

The measurement of nuclear modification
factor R_{dA} of single muons from open
heavy-flavor in d +Au collisions at
 $\sqrt{s_{NN}} = 200$ GeV

Sanghoon Lim

The Graduate School
Yonsei University
Institute of Physics and Applied Physics

The measurement of nuclear modification
factor R_{dA} of single muons from open
heavy-flavor in d +Au collisions at
 $\sqrt{s_{NN}} = 200$ GeV

A doctor's thesis

Submitted to the Institute of Physics and Applied Physics
and the Graduate School of Yonsei University
in partial fulfillment of the
requirements for the degree of
Doctor of Science

Sanghoon Lim

Feb, 2014

**This certifies that the doctors thesis
of Sanghoon Lim is approved**

Thesis Supervisor : Prof. Ju Hwan Kang

Prof. Koan Sik Joo

Prof. Su Houng Lee

Prof. Youngil Kwon

Dr. Vincent Cianciolo

**The Graduate School
Yonsei University
Feb, 2014**

항상 꿈을 가질수 있는 삶을 선물해주신
부모님께 깊은 감사를 드립니다

Be the change you want to see in the world

– Gandhi mimer in Santiago de Compostela

Contents

| | | |
|----------|--|----------|
| 1 | Introduction | 1 |
| 1.1 | Quark gluon plasma | 3 |
| 1.1.1 | Relativistic heavy-ion collisions | 6 |
| 1.1.2 | Evidences for QGP | 9 |
| 1.1.3 | Control experiment | 15 |
| 1.2 | Cold nuclear matter effects | 18 |
| 1.2.1 | Nuclear parton distribution function | 18 |
| 1.2.2 | p_T broadening | 23 |
| 1.2.3 | Nuclear breakup | 25 |
| 1.3 | Heavy quark production | 27 |
| 1.3.1 | Theoretical framework | 27 |
| 1.3.2 | Heavy quark measurements at PHENIX | 30 |
| 1.4 | Motivation for this research | 37 |

| | |
|--|-----------|
| 2 Experimental setup | 39 |
| 2.1 RHIC | 39 |
| 2.2 PHENIX experiment | 42 |
| 2.3 Muon arms | 45 |
| 2.3.1 Muon tracker | 46 |
| 2.3.2 Muon identifier | 49 |
| 2.4 Track reconstruction | 51 |
| 2.5 Event triggers | 54 |
| 2.5.1 Minimum bias trigger | 56 |
| 2.5.2 MuID local level-1 trigger | 57 |
| 2.6 Centrality determination | 58 |
| 3 Heavy-flavor muon analysis | 61 |
| 3.1 Analysis overview | 61 |
| 3.1.1 Source of tracks | 62 |
| 3.1.2 Summary of analysis procedure | 66 |
| 3.1.3 Methodology for hadronic background estimation | 69 |
| 3.2 Raw data analysis | 70 |
| 3.2.1 Data sets | 70 |
| 3.2.2 Initial quality assurance | 72 |
| 3.2.3 MB normalization | 75 |
| 3.2.4 Analysis variables | 77 |

| | | |
|-------|--|-----|
| 3.2.5 | Track quality cuts | 79 |
| 3.2.6 | Geometrical acceptance cuts | 83 |
| 3.2.7 | Magnetic field configuration | 88 |
| 3.3 | Acceptance by efficiency study | 91 |
| 3.4 | Background estimation | 96 |
| 3.4.1 | Estimation of cocktail input | 97 |
| 3.4.2 | Hadron cocktail simulation with modified nuclear cross section | 101 |
| 3.4.3 | Tuning hadron cocktail | 102 |
| 3.4.4 | Trigger efficiency consideration | 106 |
| 3.4.5 | Hadron package selection | 109 |
| 3.5 | Signal extraction | 112 |
| 3.5.1 | Signal from one hadron cocktail package | 113 |
| 3.5.2 | Combining hadron cocktail packages | 114 |
| 3.5.3 | Subtraction of muons from J/ψ decay | 117 |
| 3.5.4 | Bin shift correction | 118 |
| 3.5.5 | Combining two arms in $p+p$ collisions | 122 |
| 3.6 | Nuclear modification factor, R_{dA} | 125 |
| 3.7 | Systematic uncertainty | 126 |
| 3.7.1 | Invariant yield | 126 |
| 3.7.2 | Nuclear modification factor | 130 |

| | |
|---|------------|
| 4 Results | 131 |
| 4.1 heavy-flavor muon p_T spectra | 131 |
| 4.2 Nuclear modification function, $R_{dA}(p_T)$ | 134 |
| 4.3 Nuclear modification function, $R_{dA}(\langle N_{coll} \rangle)$ | 135 |
| 5 Discussion | 139 |
| 5.1 p_T spectra in $p+p$ collisions | 139 |
| 5.2 Comparison of R_{dA} with the results at mid-rapidity | 142 |
| 5.3 R_{dA} compared to theoretical calculations | 145 |
| 5.4 Comparison of R_{dA} between heavy-flavor muon and J/ψ | 153 |
| 6 Conclusion and outlook | 157 |
| 6.1 Conclusion | 157 |
| 6.2 Outlook | 159 |
| A Additional plots | 163 |
| A.1 R_{NS} | 163 |
| A.2 R_{CP} | 166 |
| A.3 R_{dA} of heavy-flavor lepton and J/ψ | 168 |
| B Data table | 169 |

C Good run list **181**

| | | |
|-----|--|-----|
| C.1 | Run-9 $p+p$, MuIDLL-1D and -1H triggered data | 181 |
| C.2 | Run-8 $d+Au$, MuIDLL-1D triggered data for south arm | 184 |
| C.3 | Run-8 $d+Au$, MuIDLL-1D triggered data for north arm | 187 |
| C.4 | Run-8 $d+Au$, MuIDLL-1H triggered data for south arm | 189 |
| C.5 | Run-8 $d+Au$, MuIDLL-1H triggered data for north arm | 192 |

List of Figures

| | | |
|------|--|----|
| 1.1 | History of the Universe | 2 |
| 1.2 | The strong coupling constant α_s | 4 |
| 1.3 | Energy density of QCD matter | 5 |
| 1.4 | QCD phase diagram | 7 |
| 1.5 | Time evolution of QGP | 8 |
| 1.6 | Jet production in $p+p$ and heavy-ion collisions | 9 |
| 1.7 | Invariant cross section of π^0 in central and peripheral Au+Au collisions | 10 |
| 1.8 | Nuclear modificatino factor R_{AA} of π^0 | 12 |
| 1.9 | Two particle azimuthal distributions in $p+p$, $d+Au$, and Au+Au collisions | 13 |
| 1.10 | Illustration of the initial shape of heavy-ion collisions and elliptic flow | 14 |
| 1.11 | Elliptic flow and quark number scaling | 15 |
| 1.12 | Illustration of A+A and $d(p)+A$ collisions | 16 |

| | | |
|------|--|----|
| 1.13 | Nuclear modification factor R_{dA} of charged hadron at different rapidity ranges | 17 |
| 1.14 | The parton distribution function from HERAPDF | 19 |
| 1.15 | nPDF modifications for a Pb nucleus from EPS09 | 20 |
| 1.16 | nPDF modification for a Pb nucleus from EPS09s | 21 |
| 1.17 | J_{dA} vs. $x_{\text{Au}}^{\text{frag}}$ in $d+\text{Au}$ collisions at $\sqrt{s_{NN}} = 200$ GeV | 22 |
| 1.18 | R_{dA} of light hadrons in different centrality classes | 24 |
| 1.19 | The difference between $\langle p_T^2 \rangle$ in $d+\text{Au}$ and $p+p$ collisions | 24 |
| 1.20 | R_{dA} and R_{CP} of J/ψ | 26 |
| 1.21 | Leading order production diagrams for heavy quarks | 27 |
| 1.22 | Heavy-flavor electron p_T spectrum in $p+p$ collisions at mid-rapidity | 31 |
| 1.23 | Charm cross section as a function rapidity in $p+p$ collisions | 32 |
| 1.24 | R_{AA} and v_2 of heavy-flavor electrons in $\text{Au}+\text{Au}$ collisions at mid-rapidity | 33 |
| 1.25 | R_{AA} of heavy-flavor leptons in $\text{Cu}+\text{Cu}$ collisions at mid and forward rapidity | 34 |
| 1.26 | R_{dA} of heavy-flavor electrons in $d+\text{Au}$ collisions at mid-rapidity | 35 |
| 1.27 | R_{dA} of heavy-flavor muons from Run-3 $d+\text{Au}$ data | 36 |
| 1.28 | Comparison of R_{AA} as a function of N_{part} in $\text{Au}+\text{Au}$ and $\text{Cu}+\text{Cu}$ collisions | 38 |

| | | |
|------|--|----|
| 2.1 | RHIC facility | 40 |
| 2.2 | illustratioin of the PHENIX | 42 |
| 2.3 | The kinematic acceptance of the PHENIX | 43 |
| 2.4 | illustratioin of the PHENIX | 44 |
| 2.5 | Location of absorbers in the muon arm | 45 |
| 2.6 | Drawing of the South muon tracker | 46 |
| 2.7 | Numbering scheme of the MuTr | 48 |
| 2.8 | MuID panel | 50 |
| 2.9 | Drawing of the MuID panel and plastic tubes | 51 |
| 2.10 | Event display of single J/ψ | 52 |
| 2.11 | Event display in the MuTr | 53 |
| 2.12 | Configuratton of symset for MuID level-1 trigger | 57 |
| 2.13 | MuID local level-1 trigger symset logic | 58 |
| 2.14 | The South BBC response in d +Au collisions with simulation | 60 |
| 2.15 | Distribution of $\langle N_{\text{coll}} \rangle$ for different centrality classes in d +Au collisions | 60 |
| 3.1 | Schematic view of particle flux in the muon arm | 62 |
| 3.2 | Longitudinal momentum distribution at MuID Gap-2 at north arm | 66 |
| 3.3 | Analysis flow | 67 |
| 3.4 | Average event z -vertex per run | 72 |

| | | |
|------|--|----|
| 3.5 | Production rate at the MuID Gap-4 in Run-9 $p+p$ data | 73 |
| 3.6 | Fraction of events in centrality classes of Run-8 $d+\text{Au}$ data | 74 |
| 3.7 | Run scaler of MuIDLL1D triggers during Run-8 | 75 |
| 3.8 | Run scaler of MB and MuIDLL1D triggers during Run-9 | 75 |
| 3.9 | Schematic view of DG0 and DDG0 | 77 |
| 3.10 | Schematic view of R_{ref} | 78 |
| 3.11 | Schematic view of $p\delta\theta$ | 80 |
| 3.12 | DG0 and $p\delta\theta$ distributions of the data and muon simulation at MuID Gap-4 | 81 |
| 3.13 | DDG0 and R_{ref} distributions of the data, G-FLUKA, and GHEISHA at MuID Gap-3 | 84 |
| 3.14 | MuTr 2D hit histograms | 86 |
| 3.15 | Comparison of ϕ and r distributions between the data and the hadron simulations | 87 |
| 3.16 | Raw track yield per run at MuID Gap-2, 3 and 4 of two magnetic field configurations | 89 |
| 3.17 | Raw p_T spectra at MuID Gap-2, 3 and 4 of the simulation and the data with two magnetic field configurations | 90 |
| 3.18 | Acceptance by efficiency for different centrality classes in Run-8 $d+\text{Au}$ | 94 |
| 3.19 | z -vertex dependent acceptance by efficiency for different centrality classes in Run-8 $d+\text{Au}$ | 95 |
| 3.20 | Comparison of K/π ratios for the hadron cocktail | 98 |

| | | |
|------|---|-----|
| 3.21 | Comparison of p_T spectra for the hadron cocktail | 99 |
| 3.22 | Comparison of weighting factors | 104 |
| 3.23 | Tuning matrix | 105 |
| 3.24 | MuIDLL1 trigger efficiency for Run-8 $d+\text{Au}$ | 107 |
| 3.25 | MuIDLL1 trigger efficiency for Run-9 $p+p$ | 108 |
| 3.26 | Matching stopped hadrons at MuID Gap-2 and 3 | 110 |
| 3.27 | Matching slopes of normalized z -vertex distribution at MuID Gap-4 | 111 |
| 3.28 | Comparison of different hadron packages for Run-9 $p+p$ | 116 |
| 3.29 | Examples of the parametrization of J/ψ production in $d+\text{Au}$ collisions | 119 |
| 3.30 | Comparison of inclusive heavy-flavor muons and muons from J/ψ | 120 |
| 3.31 | Fit to the invariant yield of heavy-flavor muons in $d+\text{Au}$ collisions for the bin shift correction | 121 |
| 3.32 | Yield variation of hadron packages by K/π ratio change | 129 |
| 4.1 | Invariant cross section of heavy-flavor muon in $p+p$ collisions | 132 |
| 4.2 | Invariant yield of heavy-flavor muon in $d+\text{Au}$ collisions | 133 |
| 4.3 | R_{dA} in 0-100% centrality $d+\text{Au}$ collisions | 135 |
| 4.4 | R_{dA} in 0-20% centrality $d+\text{Au}$ collisions | 136 |
| 4.5 | R_{dA} in 20-40% centrality $d+\text{Au}$ collisions | 136 |
| 4.6 | R_{dA} in 40-60% centrality $d+\text{Au}$ collisions | 137 |

| | | |
|------|--|-----|
| 4.7 | R_{dA} in 60–88% centrality d +Au collisions | 137 |
| 4.8 | p_T integrated R_{dA} for two p_T ranges | 138 |
| 5.1 | p_T spectrum in p + p collisions and comparisons | 140 |
| 5.2 | Comparison of R_{dA} as a function of p_T at different rapidity ranges | 143 |
| 5.3 | Comparison of R_{dA} as a function of $\langle N_{\text{coll}} \rangle$ at different rapidity ranges | 144 |
| 5.4 | Comparison of R_{dA} to theoretical calculations in 0–100% d +Au collisions | 146 |
| 5.5 | Comparison of R_{dA} to EPS09s calculation in 0–20% and 60–88% d +Au collisions | 148 |
| 5.6 | Comparison of R_{dA} to EPS09s calculations adding initial k_T in 0–20% | 149 |
| 5.7 | Comparison of R_{dA} as a function of $\langle N_{\text{coll}} \rangle$ to EPS09s calculation | 150 |
| 5.8 | x_2 as a function of p_T | 151 |
| 5.9 | Comparison of R_{dA} as a function of x_2 to EPS09s calculation in 0–20% and 60–88% d +Au collisions | 152 |
| 5.10 | Comparison of R_{dA} between heavy-flavor muon and J/ψ in 0–20% and 60–88% d +Au collisions | 154 |
| 5.11 | R_{dA} of J/ψ as a function of $\langle N_{\text{coll}} \rangle$ at different rapidity ranges | 155 |
| 6.1 | View of the VTX and FVTX | 160 |

| | | |
|-----|---|-----|
| A.1 | R_{NS} in 0–100% centrality $d+\text{Au}$ collisions | 163 |
| A.2 | R_{NS} in 0–20% centrality $d+\text{Au}$ collisions | 164 |
| A.3 | R_{NS} in 20–40% centrality $d+\text{Au}$ collisions | 164 |
| A.4 | R_{NS} in 40–60% centrality $d+\text{Au}$ collisions | 165 |
| A.5 | R_{NS} in 60–88% centrality $d+\text{Au}$ collisions | 165 |
| A.6 | R_{CP} in 0–20% centrality $d+\text{Au}$ collisions | 166 |
| A.7 | R_{CP} in 20–40% centrality $d+\text{Au}$ collisions | 166 |
| A.8 | R_{CP} in 40–60% centrality $d+\text{Au}$ collisions | 167 |
| A.9 | R_{dA} of heavy-flavor lepton and J/ψ | 168 |

List of Tables

| | | |
|-----|--|-----|
| 2.1 | RHIC run history | 41 |
| 2.2 | MuID gap positions | 49 |
| 2.3 | PHENIX trigger configuration | 55 |
| 2.4 | Centrality characterization in d +Au collisions | 59 |
| 3.1 | Sampled MB events for Run-8 d +Au and Run-9 $p+p$ data set | 76 |
| 3.2 | Analysis cuts for the muon candidates | 82 |
| 3.3 | Analysis cuts for the stopped hadrons | 85 |
| 3.4 | Acceptance by efficiency correction factors for Run-9 $p+p$ data | 92 |
| 3.5 | PYTHIA parameter set | 98 |
| 3.6 | good hadron cocktail packages | 110 |
| 3.7 | Bin shift correction factors | 123 |
| 3.8 | Source of systematic uncertainty | 126 |
| 3.9 | Systematic uncertainty on acceptance by efficiency calculation | 128 |

| | | |
|------|--|-----|
| B.1 | Heavy-flavor muon cross section in $p+p$ collisions | 169 |
| B.2 | Heavy-flavor muon invariant yield in 0-100% d +Au collisions | 170 |
| B.3 | Heavy-flavor muon invariant yield in 0-20% d +Au collisions | 171 |
| B.4 | Heavy-flavor muon invariant yield in 20-40% d +Au collisions | 172 |
| B.5 | Heavy-flavor muon invariant yield in 40-60% d +Au collisions | 173 |
| B.6 | Heavy-flavor muon invariant yield in 60-88% d +Au collisions | 174 |
| B.7 | Heavy-flavor muon R_{dA} in 0-100% d +Au collisions | 175 |
| B.8 | Heavy-flavor muon R_{dA} in 0-20% d +Au collisions | 176 |
| B.9 | Heavy-flavor muon R_{dA} in 20-40% d +Au collisions | 177 |
| B.10 | Heavy-flavor muon R_{dA} in 40-60% d +Au collisions | 178 |
| B.11 | Heavy-flavor muon R_{dA} in 60-88% d +Au collisions | 179 |
| B.12 | Heavy-flavor muon integrated R_{dA} for $1.0 < p_T < 3.0$ GeV/ c | 180 |
| B.13 | Heavy-flavor muon integrated R_{dA} for $3.0 < p_T < 5.0$ GeV/ c | 180 |

Abstract

The measurement of nuclear modification factor R_{dA} of single muons from open heavy-flavor in $d+\text{Au}$ collisions at $\sqrt{s_{NN}} = 200$ GeV

Sanghoon Lim

Institute of Physics and Applied Physics

The Graduate School

Yonsei University

Heavy quarks, produced in the early stage of heavy-ion collisions, are very effective probes of dense medium produced at RHIC. The measurement of heavy quarks in $p+p$ collisions provides a baseline to quantify nuclear effects in variety of beam species as well as a test of pQCD calculation. Furthermore, the same measurement in $d+\text{Au}$ collisions allows to probe initial state Cold Nuclear Matter (CNM) effects on heavy quark production.

PHENIX muon arm has an ability to measure muons at forward ($1.2 < \eta < 2.4$) and backward ($-2.2 < \eta < -1.2$) rapidity regions. A new analysis technique to estimate backgrounds effectively was developed in previous analysis of $p+p$ and Cu+Cu data taken running Run-5. This new analysis technique estimates background components by utilizing a full Monte Carlo simulation called "Hadron Cocktail". Similar analysis method was adopted to Run-8 $d+\text{Au}$ and Run-9 $p+p$ data sets. The open heavy-flavor production via muons at rapidity range of $1.4 < |y| < 2.0$ in $p+p$ and $d+\text{Au}$ collisions at $\sqrt{s_{NN}} = 200$ GeV

has been measured. Based on this measurement, nuclear modification factor R_{dA} has been calculated for different centrality classes (0–100%, 0–20%, 20–40%, 40–60%, 60–88%) to quantify CNM effects on heavy quark production.

Key Words: RHIC, PHENIX, Cold Nuclear Matter, Heavy quark, R_{dA}

Chapter 1

Introduction

About 14 billion years ago, the **Big Bang** occurred, and everything started. At the very beginning, temperature was still so high that all quarks, anti-quarks, and gluons were free. They were deconfined and formed a thermalized state known as **quark gluon plasma (QGP)** as shown in Fig. 1.1. As time went on, the Universe continuously expanded, and the temperature and energy density decreased. Quarks and gluons started to form particles, and then these hadrons were bound into small nuclei. Now we are living at the very cold Universe, relative to the beginning, and almost everything is stabilized. The curiosity about such as the origin and fundamental things of the Universe has been the driving force for the development of science. Experiments with novel accelerators have succeeded in producing very hot and dense matters, similar to what existed during the first few micro-seconds, we can trace back and explore the extremely hot and dense matters.

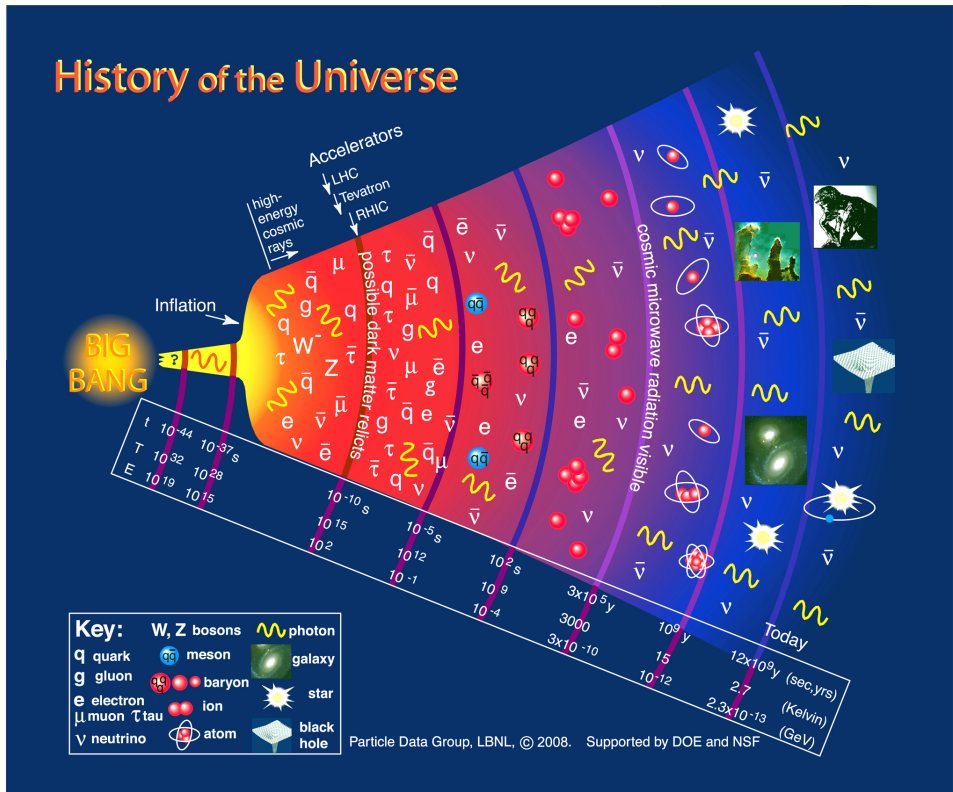


Figure 1.1: History of the Universe [1].

1.1 Quark gluon plasma

When the energy density ϵ exceeds some typical hadronic value ($\sim 1 \text{ GeV/fm}^3$), matter no longer consists of separate hadrons (protons, neutrons, etc.), but as their fundamental constituents, quarks and gluons. Because of the apparent analogy with similar phenomena in atomic physics we may call this phase of matter the QCD (or quark-gluon) plasma.

- E. V. Shuryak [2]

Quantum chromodynamics (QCD) is the modern theory of the Standard Model to describe the strong interactions between quarks and gluons. Two properties of QCD are:

- Confinement means there is no free stable free quark and quarks are always confined as color neutral states. This property is due to the fact that the strong force between quarks and gluons becomes stronger as the distance between them goes longer. Therefore, an infinite amount of energy would be needed to separate bounded quarks.
- Asymptotic freedom is that the strong interaction becomes effectively weak in very high-energy reactions. In this regime, a perturbation theory may be applied to describe the effectively weakened strong force. This property was predicted by H. D. Politzer [3, 4] and by F. Wilczek and D. Gross [5, 6], and they were awarded the Nobel Prize in 2004.

Based on the second property of QCD listed above, a general perturbative cross section in QCD could be expanded as a power series:

$$\sigma_{\text{QCD}} = A_1 \alpha_s + A_2 \alpha_s^2 + \dots \quad (1.1)$$

where A_i is coefficient of the i -th order determined by the Feynman rules, and α_s is the effective QCD coupling constant [1]. The α_s as a function of the momentum transfer, Q is,

$$\alpha_s(Q^2) = (\beta_0 \ln(Q^2/\Lambda_{\text{QCD}}))^{-1}. \quad (1.2)$$

When the energy scale is much larger than the Λ_{QCD} (~ 200 MeV) the QCD can be described by the perturbation theory. In addition, the

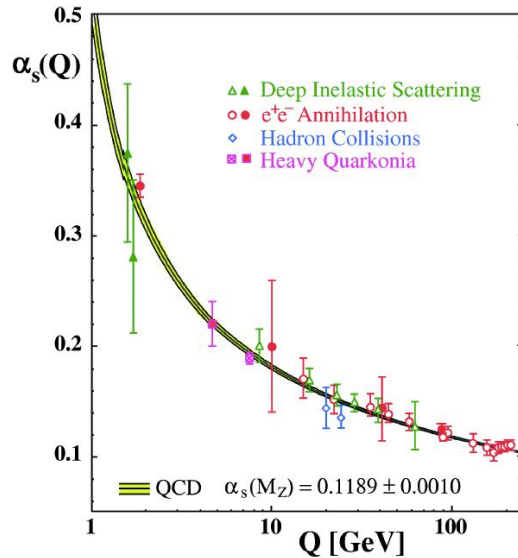


Figure 1.2: The strong coupling constant α_s as a function of energy scale Q . The lines are predictions from QCD with world average value of $\alpha_s(M_Z)$ [7].

quarks and gluons are deconfined from the strong interaction between each other in this kind of extreme energy limit. Figure 1.2 shows many experimental data for the strong coupling constant.

As the quotation at the begining of this section, there would be a phase transition of the normal nuclear matter into the new state of matter called QCD plasma or QGP. In the framework of lattice QCD, an existence of the phase transition to QGP is was shown. As shown in Fig. 1.3, the quantity of ϵ/T^4 increases drastically at a temperature T_C , called critical temperature. These results indicate a phase transition from the hadronic system to QGP with large degrees of freedom.

Assuming massless non-interacting particles, the degree of freedom for each of bosons and fermions contribute to the energy density by the amount of $\frac{\pi^2}{30}$ and $\frac{7\pi^2}{8 \cdot 30}$, respectively. In contrast to ~ 3 estimated degrees of freedom for hadron gas dominated by π^+ , π^0 , and π^- , the degrees of freedom above T_C are expected as 16 for gluons¹ plus 36

¹2(helicity) \times 8(color) = 16

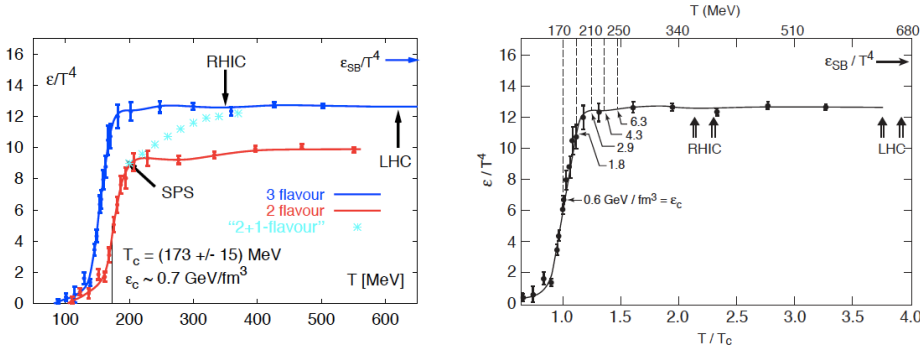


Figure 1.3: Energy density of QCD matter with two and three flavors of dynamical quark [8, 9].

for quarks² and anti-quarks. Therefore, energy density would hugely increases to $37 \cdot \frac{\pi^2}{30} T^4$ ($47.5 \cdot \frac{\pi^2}{30} T^4$) for 2 (3) active flavor QGP as follows.

$$\begin{aligned}\varepsilon_{f=2} &= \{2(\text{flavor}) \cdot 2(\text{spin}) \cdot 2(q\bar{q}) \cdot 3(\text{color}) \cdot \frac{7}{8} + 2(\text{helicity}) \cdot 8(\text{color})\} \frac{\pi^2}{30} T^4 \\ &= 37 \frac{\pi^2}{30} T^4\end{aligned}\quad (1.3)$$

$$\begin{aligned}\varepsilon_{f=3} &= \{3(\text{flavor}) \cdot 2(\text{spin}) \cdot 2(q\bar{q}) \cdot 3(\text{color}) \cdot \frac{7}{8} + 2(\text{helicity}) \cdot 8(\text{color})\} \frac{\pi^2}{30} T^4 \\ &= 47.5 \frac{\pi^2}{30} T^4\end{aligned}\quad (1.4)$$

The right plot in the Fig. 1.3 shows the case of 3 light flavors, and absolute values of ϵ for several temperatures are also written. In order to reach the fully transited point (upper edge of the transition slope), almost five time larger energy density than the energy density at $T = T_C$ is needed. Relativistic Heavy Ion Collider (RHIC) was expected make this kind of extremely dense nuclear matter, and the maximum temperature achieved in Au+Au collisions is expected to be almost $T = 2T_C$.

1.1.1 Relativistic heavy-ion collisions

The hot and dense QCD medium discussed in the previous section is believed to be produced by collisions of heavy nuclei of very high energies. Several accelerators have been built and operated; Bevalac at LBNL, AGS at BNL, SPS at CERN, RHIC at BNL, and LHC at

² $2(\text{spin}) \times 3(\text{flavor}) \times 3(\text{color}) \times 2(q, \bar{q}) = 36$

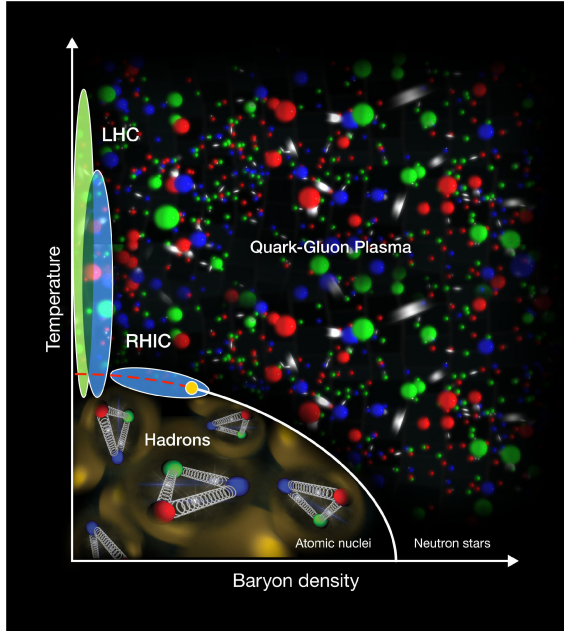


Figure 1.4: QCD phase diagram.

CERN. For the first time, a new state of matter, QGP, was produced in Au+Au collisions of $\sqrt{s_{NN}} = 200$ GeV at RHIC. After the discovery of QGP, the LHC started to operate from 20094 and made the hottest and densest QGP in the world from Pb+Pb collisions up to $\sqrt{s_{NN}} = 2.76$ TeV

Figure 1.4 shows a schematic phase diagram of nuclear matter over a range of temperature and baryon chemical potential, μ_B [11, 12]. In the figure, blue area is the region reached at RHIC and a green area is that at the LHC. The net baryon density is expected to be low in relativistic heavy-ion collisions at these colliders [13], so regions for both facilities are located left side of the diagram. The exact order of the phase transition is unknown, but second order transition is expected

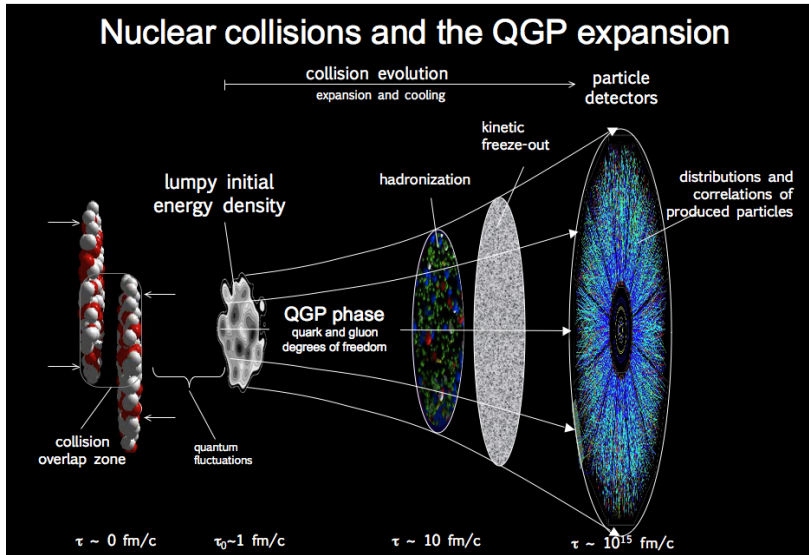


Figure 1.5: Time evolution of QGP [10].

in the case of zero net baryon density [13]. When the baryon chemical potential is sufficiently high, the phase transition from hadronic matter to QGP is first order transition as shown with the white line in Fig. 1.4. After the critical point (yellow point), the transition changes to the second order. RHIC also has a program to search the critical point by varying the collision energies, 4 called energy scan (area along the red dashed line).

Figure 1.5 shows sequential pictures of a heavy-ion collision from the collision to the measurement of particles at detectors. Since the speed of nucleus is almost the speed of light, a nucleus before collision looks like a pancake due to the Lorentz contraction. Right after the collision, quarks and gluons are produced during the formation time. At $\tau \sim 1 \text{ fm}/c$, produced partons strongly interact each other, then a thermalized medium is formed. As the system evolves and expands,

the temperature and energy density decrease. When the temperature drops below the critical temperature, hadrons are started to be formed. After the chemical freeze-out, particle composition at that time is longer changed, but momentum transfer still occurs. If the temperature cools down below the kinematic freeze-out temperature, hadrons move out freely toward detectors.

1.1.2 Evidences for QGP

During the first three years of RHIC operation, many interesting results were obtained from $p+p$, Au+Au, and d +Au collisions from all experiments, BRAHMS [14], PHOBOS [15], PHENIX [13], and STAR [16]. Among plenty of interesting results, two most interesting and critical results, supporting for the existence of QGP, will be introduced.

Jet quenching

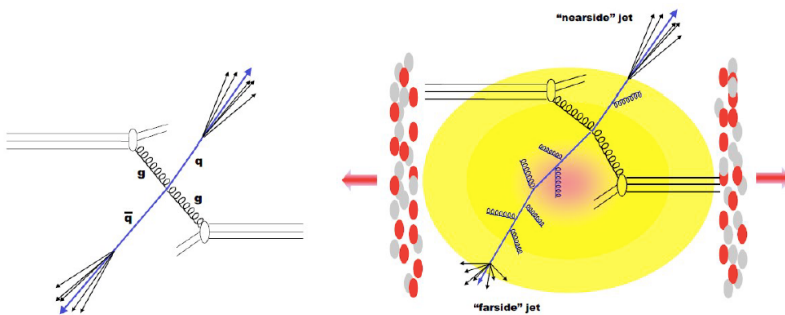


Figure 1.6: Jet production in $p+p$ (left) and heavy-ion (right) collisions.

In order to study of properties of QGP expected to be formed in heavy-ion collisions, observables, containing the information at earliest time and being sensitive to the properties of QGP, should be measured. Jet, which is produced by the hard scattering between partons, is considered one of the clean signals. Two back-to-back jets are usually produced, and both energetic partons fragment into a number of hadrons inside cone shapes in case of $p+p$ collisions. This is illustrated on the left in Fig 1.6.

When energetic partons traverse through the hot and dense medium, a suppression of high p_T hadrons is predicted due to energy loss of partons [17, 18]. In case of heavy-ion collisions, high p_T partons penetrating the medium lose their energy due to medium-induced gluon

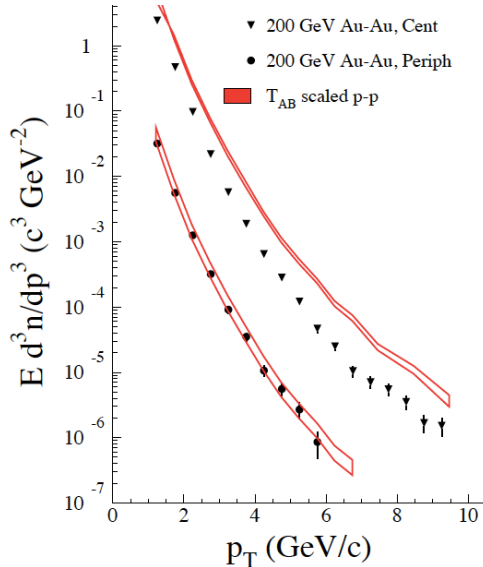


Figure 1.7: Invariant cross section of π^0 in central and peripheral Au+Au collisions at $\sqrt{s_{NN}} = 200$ GeV [13].

bremstrahlung and many soft collisions with partons in the medium. As shown in the right plot of Fig. 1.6, lots of gluons are emitted from the energetic parton of farside jet. Therefore, this parton fragments into large number of low momentum hadrons at wider area than that of the nearside jet.

Figure 1.7 shows p_T spectra of π^0 in central and peripheral Au+Au collisions at $\sqrt{s_{NN}} = 200$ GeV in PHENIX [13]. Two red lines are scaled p_T spectra in $p+p$ collisions scaled by the nuclear overlap function corresponding to each centrality class. In case of peripheral collisions, the scaled $p+p$ data is consistent, whereas a huge suppression of high p_T π^0 production is observed in central Au+Au collisions.

The medium effects on the jet production and the suppression of high p_T particles could be directly quantified with the nuclear modification factor,

$$R_{AA} = \frac{dN_{A+A}}{\langle N_{\text{coll}} \rangle dN_{p+p}} \quad (1.5)$$

where dN_{A+A} and dN_{p+p} are the invariant yield in A+A and $p+p$ collisions, and $\langle N_{\text{coll}} \rangle$ is the average number of binary collisions for a certain centrality class. If this quantity is over the unity ($R_{AA} > 1$), the measured particle production in heavy-ion collisions is enhanced relative to the results in $p+p$ collisions. On the contrary, a suppression is happened in heavy-ion collisions, when R_{AA} is less than one ($R_{AA} < 1$). Figure 1.8 shows R_{AA} of π^0 in Au+Au collisions at $\sqrt{s_{NN}} = 200$ GeV for different centrality classes from the PHENIX experiment [19]. A factor of 4 – 5 suppression is observed in the most central (0–10%) Au+Au collisions compared to the $p+p$ results.

The angular correlation between a trigger particle and associated par-

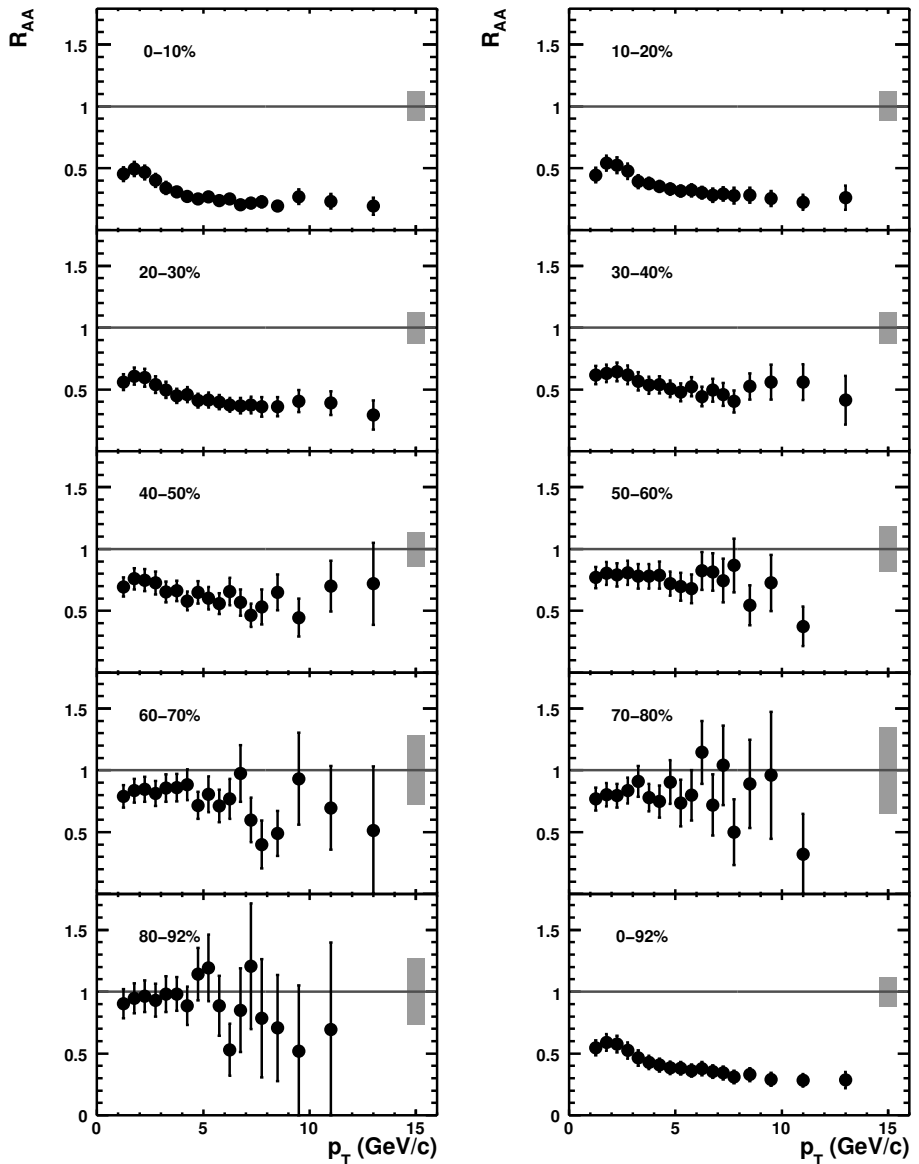


Figure 1.8: Nuclear modification factor R_{AA} of π^0 in Au+Au collisions at $\sqrt{s_{NN}} = 200$ GeV for different centrality classes at $\sqrt{s_{NN}} = 200$ GeV [19].

ticles is another clear view to probe the jet modification. Figure 1.9 shows the angular correlations in $p+p$ (line), $d+\text{Au}$, and central $\text{Au}+\text{Au}$ (blue stars) collisions measured by the STAR collaboration [20]. In the bottom panel, a cone structure at away-side ($\Delta\phi \approx \pi$), seen in $p+p$ and $d+\text{Au}$ collisions, is completely suppressed in central $\text{Au}+\text{Au}$ collisions. The results from $d+\text{Au}$ collisions, which is consistent with the results in $p+p$ collisions, also strongly supports the exsistence of QGP in heavy-ion collisions.

Elliptic flow

Another interesting property of QGP is elliptic flow. In non-central $\text{Au}+\text{Au}$ collisions at RHIC, the distribution of produced particles shows a large anisotropy relative to a reaction plane. This observed anisotropy is intimately related to the geometry of nucleus collision and the property of created medium. If the medium is like a weakly

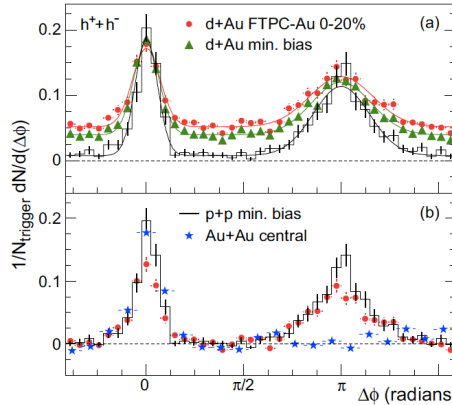


Figure 1.9: Correlated two particle azimuthal distributions in $p+p$, $d+\text{Au}$, and $\text{Au}+\text{Au}$ collisions measured by the STAR experiment [20].

interacting gas state, the initial geometry information of asymmetric collision would disappear during the rapid expansion. However, if partons inside the medium interact strongly with each other, a larger pressure gradient would be developed along the short axis of the initial almond shape. Figure 1.10 shows how the initial spatial anisotropy converts into the momentum anisotropy.

This property can be quantified by a Fourier expansion of an angular distribution of produced particles relative to the reaction plane as,

$$E \frac{d^3N}{dp^3} = \frac{1}{2\pi p_T} \frac{d^2N}{dp_T dy} \left(1 + \sum_n 2v_n(p_T) \cos [n(\phi - \Psi_R)] \right) \quad (1.6)$$

where Ψ_R is the azimuthal angle of the reaction plane, and v_n is the Fourier coefficient of n -th order. The elliptic flow is the coefficient of second order.

Figure 1.11 shows v_2 of identified hadrons in Au+Au collisions as a function of (a) p_T and (b) transverse kinetic energy (KE_T) measured by the PHENIX [21] and STAR [22, 23]. The v_2 as a function of KE_T , considering relativistic effects, shows alignments of mesons and baryons respectively. When scaling of the v_2 with the n_q (2 for mesons and 3 for

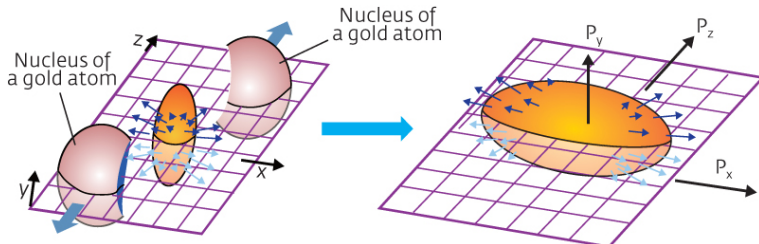


Figure 1.10: An initial almond shape after a non-central nucleus collision (left) and flow development along the reaction plane (right).

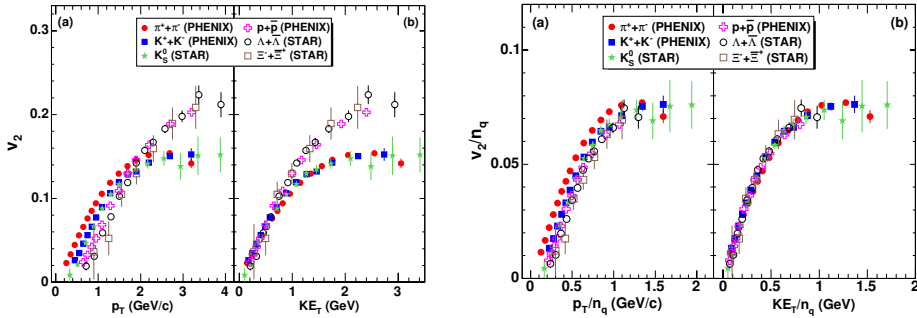


Figure 1.11: Elliptic flow v_2 (left panel) and scaled v_2 (right panel) by quark numbers (n_q) as a function of p_T and KE_T in Au+Au collisions at $\sqrt{s_{NN}} = 200$ GeV measured by the PHENIX [21] and the STAR [22, 23].

baryons), v_2/n_q of all hadrons amazingly follows an universal scaling. This universal scaling supports that the collective motion is developed in the partonic state rather than the hadronic state. Therefore, these results suggest that the QGP formed in heavy-ion collisions would be a strongly interacting medium.

1.1.3 Control experiment

Just after the first run of Au+Au collisions at RHIC, many striking results supporting the formation of QGP came out. During the third year of the RHIC operation, the experiment of d +Au collisions was performed as a control experiment. In d +Au collisions, it is believed that the hot and dense medium is not formed, but there still exist intrinsic matter effects, called cold nuclear matter effects, of the Au nucleus. In order to better understand of the results from Au+Au collisions, which both cold and hot nuclear matter effects exist, the

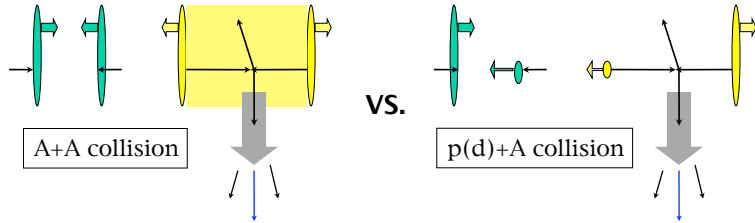


Figure 1.12: Illustration of $A+A$ (left) and $d(p)+A$ (right) collisions.

$d+A$ collisions can be used as a different kind of baseline.

Figure 1.12 is illustrations of $A+A$ (left) and $d(p)+A$ (right) collisions. In contrast to the jet quenching in QGP from $A+A$ collision, no modification of a back-to-back jet is expected in $d(p)+A$ collisions. As shown in Fig. 1.9, the jet angular correlation in $d+A$ collisions is similar with the $p+p$ results. In addition, no high p_T suppression is observed in the inclusive charged hadron production in $d+A$ collisions as shown in Fig. 1.13. From these comparisons, it can be concluded that the jet quenching is a clear evidence of QGP expected to be formed in $Au+Au$ collisions. However, a small suppression is observed at forward rapidity ($\eta = 3.2$), which is expected to be due to the cold nuclear matter effects which will be discussed in the next section. In order to clearly distinguish between the hot and cold nuclear matter effects, very precise measurements in both $d(p)+A$ and $A+A$ collision are essential.

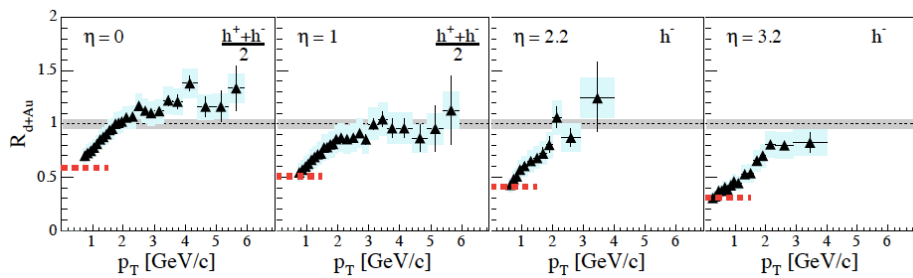


Figure 1.13: Nuclear modification factor R_{dA} of charged hadron at different rapidity ranges, $\eta = 0, 1, 2.2, 3.2$, measured by the BRAHMS [24].

1.2 Cold nuclear matter effects

In heavy-ion collisions, both effects due to hot nuclear matter (HNM) and cold nuclear matter (CNM) are excited together, so it is hard to conclude that a certain phenomena observed in heavy-ion collisions is attributed solely to the HNM effects. In order to fully understand the results in heavy-ion collisions and distinguish effects from the HNM and CNM, a control experiment of $d(p)+A$ collisions, which is thought to have minimal effects from the HNM, is needed. Even though the HNM (similar with the QGP formed in heavy-ion collisions) is hardly formed in $d(p)+A$ collisions, this collision system is surely different from the $p+p$ collisions because of the modifications inside the nucleus.

1.2.1 Nuclear parton distribution function

Parton distribution functions (PDF) describe the density of partons (valence and sea quarks, and gluons) in side a free proton as a function of magnitude of momentum transfer (Q^2) and longitudinal momentum fraction (x). Figure 1.14 shows an example of PDF distributions at $Q^2 = 10$ GeV 2 from HERAPDF 1.7 [25]. The PDFs inside a proton are determined by parametrizations of the data from deep inelastic scattering (DIS) experiments and Drell-Yan (DY) process. Since the DIS and DY are mostly related to the distributions of quarks and anti-quarks, uncertainty of the gluon distribution is relatively larger than those of quarks and anti-quarks. As hard scattering processes at RHIC energy are dominated by gluon interactions, the larger uncertainty can be narrowed down based on the results from RHIC. The modification of PDF inside a nucleus was found from nuclear DIS experiments [27].

This modification of nuclear PDF (nPDF) can be quantified by the ratio of form factors between the nucleus and proton:

$$R_i^A(x, Q^2) = \frac{f_i^A(x, Q^2)}{f_i(x, Q^2)} \quad (1.7)$$

where $f_i(x, Q^2)$ is the PDF of parton flavor i inside a free proton, $f_i^A(x, Q^2)$ is the PDF of parton flavor i inside a nucleus A . The measurements from $l+A$ DIS and DY via di-leptons in $p+A$ are used to parameterize the nPDF. There are various parameterizations, nDSg [28], EKS98 [29], and EPS09 [26], and the most commonly used nPDF is the EPS09. The nPDF modifications of a Pb nucleus from the iEPS09 [26] are shown in Fig. 1.15. Plots are on the top (at the bottom) are NLO (LO) calculations at $Q^2 = 1.69 \text{ GeV}^2$ (2.25 GeV^2). Figure 1.16 shows

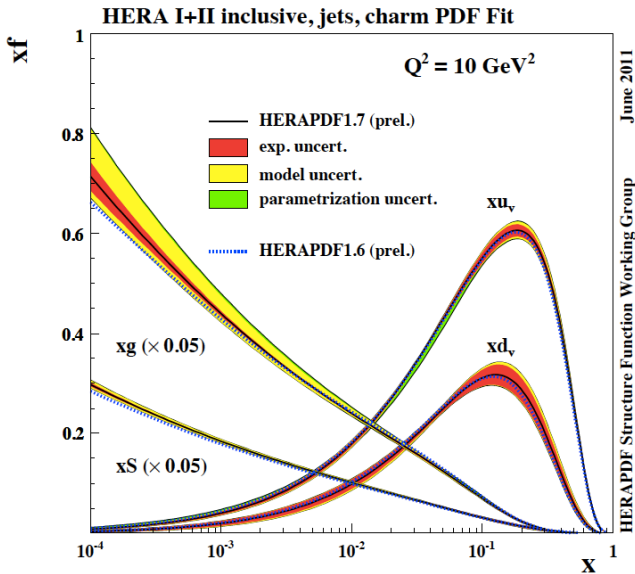


Figure 1.14: The PDF from HERAPDF 1.7 [25] at $Q^2 = 10 \text{ GeV}^2$.

a new version of the nPDF, called EPS09s, including a spatial dependence inside the nucleus [30]. The modifications of nPDF are classified into four categories depending on the value of R_i^A and x region such as shadowing, anti-shadowing, EMC region, and Fermi-motion.

- **Shadowing** refers to a suppression of parton densities relative to the free proton ($R_i^A(x, Q^2) < 1$) at low- x region, $x \lesssim 10^{-2}$. As shown in Fig. 1.15, the shadowing effect is largest on the gluon distribution, and this is probably attributed to self-interaction of high-density gluons known as a gluon saturation.

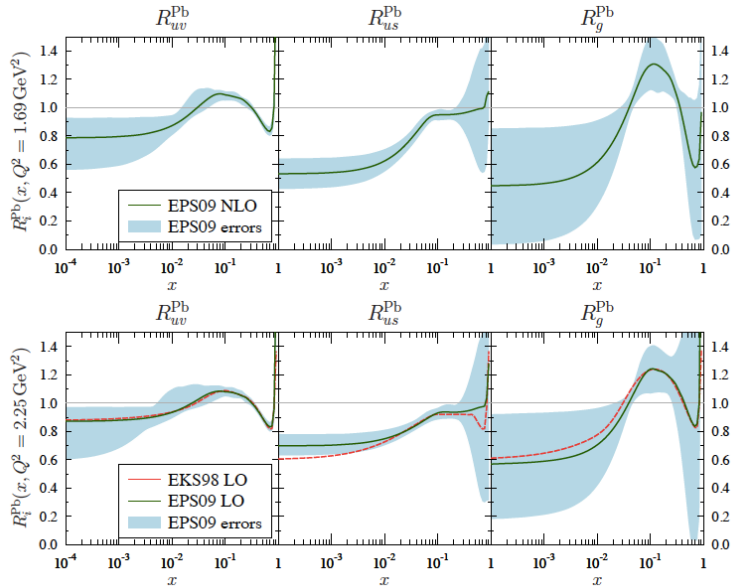


Figure 1.15: nPDF modifications for a Pb nucleus from EPS09 [26] in case of two Q^2 . Solid lines are for the valence quarks (R_V^Pb , left), sea quark (R_S^Pb , middle), and gluon (R_G^Pb , right) distributions.

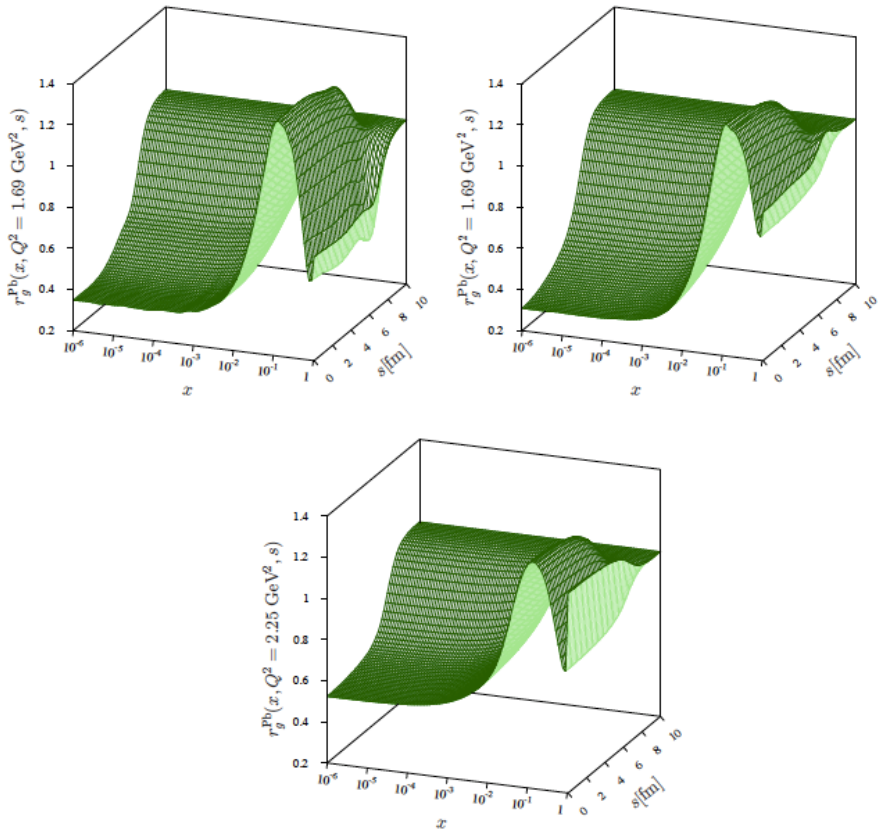


Figure 1.16: Spatial dependent nPDF modifications for a Pb nucleus, $R_g^{\text{Pb}}(x, Q^2, s)$, from EPS09sNLO1 (upper left), EPS09sLO1 (upper right), and EKS98s (lower).

- **Anti-shadowing** refers to an enhancement of parton densities relative to the free proton ($R_i^A(x, Q^2) > 1$) at intermediate- x region, $2 \times 10^{-2} \lesssim x \lesssim 2 \times 10^{-1}$. The anti-shadowing effect is clearly seen at the gluon distribution and barely seen at the sea quark (R_{uv}^{Pb}) in Fig. 1.15. In case of the gluon anti-shadowing, this is believed a counter effect of the gluon shadowing; two low- x

gluons fuse and make a high-x gluon.

- **EMC region** refers to a decrease of $R_i^A(x, Q^2)$ at $2 \times 10^{-1} \lesssim x \lesssim 7 \times 10^{-1}$ region. This phenomenon was discovered by the European Muon Collaboration (EMC) from scattering muons on deuteron and iron [27, 31]. These experimental results disagree with the theoretical calculations, and the physical interpretation for this EMC effect is still ambiguous.
- **Fermi motion** refers to a large increase of $R_i^A(x, Q^2)$ at highest- x region due to the Fermi (quantum) motion of nucleons inside a nucleus [32, 33].

Figure 1.17 shows the PHENIX results of J_{dA} depending on $x_{\text{Au}}^{\text{frag}}$ in $d+\text{Au}$ collisions at $\sqrt{s_{NN}} = 200$ GeV; where J_{dA} is the ratio of pair

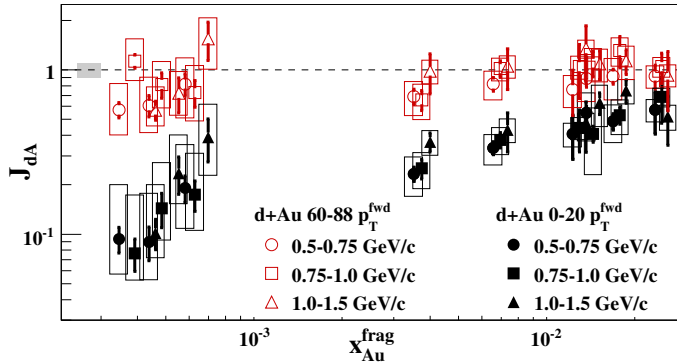


Figure 1.17: PHENIX results of J_{dA} vs. $x_{\text{Au}}^{\text{frag}}$ in $d+\text{Au}$ collisions at $\sqrt{s_{NN}} = 200$ GeV by measuring π^0 at forward rapidity region, $3.0 < \eta < 3.8$ [34].

production between $d+\text{Au}$ and $p+p$ collisions,

$$J_{d\text{A}} = \frac{1}{\langle N_{\text{coll}} \rangle} \frac{\sigma_{d\text{A}}^{\text{pair}} / \sigma_{d\text{A}}}{\sigma_{pp}^{\text{pair}} / \sigma_{pp}}, \quad (1.8)$$

and $x_{\text{Au}}^{\text{frag}}$ is momentum fraction of partons in the Au nucleus, $x_{\text{Au}}^{\text{frag}} = (\langle p_{T1} \rangle e^{-\langle \eta_1 \rangle} + \langle p_{T2} \rangle e^{-\langle \eta_2 \rangle}) / \sqrt{s_{NN}}$, measured in $2 \rightarrow 2$ scatterings. This plot is made from π^0 pair measurements, mid-forward and forward-forward correlations, by the PHENIX central arm and MPC detectors. In Fig. 1.17 filled black points are in the most central (0–20%) $d+\text{Au}$ collisions, and open red points are from the most peripheral (60–88%) collisions. As shown in Fig. 1.17, a clear suppression of back-to-back pair production relative to the $p+p$ collisions is shown at low- x region in central $d+\text{Au}$ collisions, and the results indicate a strong shadowing effect.

1.2.2 p_T broadening

Historically in the 1970's, an enhanced particle production at moderate p_T region in $p+\text{A}$ collisions compared to $p+p$ collisions [35], which is called Cronin effect, was observed. This enhancement of particle production at intermediate p_T region, which results in a deficit of low p_T particles, is thought to be attributed to multiple scattering of partons inside a nucleus before the hard scattering. During the elastic multiple scatterings, partons gain transverse momentum, and this leads to the enhancement of final state particles at moderate p_T region.

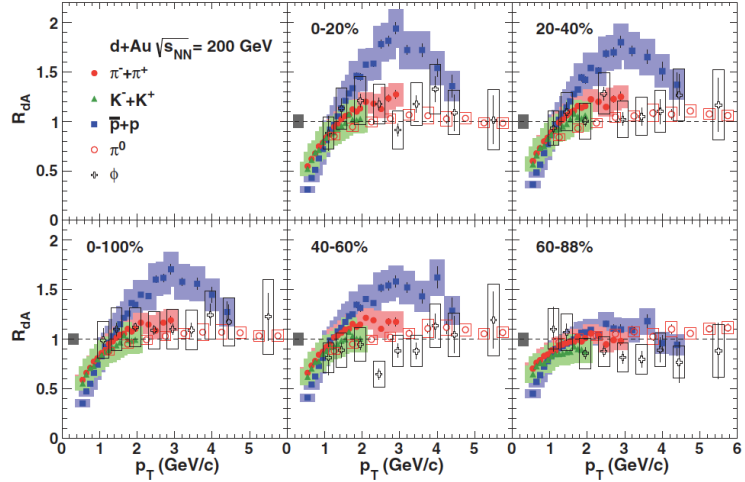


Figure 1.18: R_{dA} of light hadrons in different centrality classes [36].

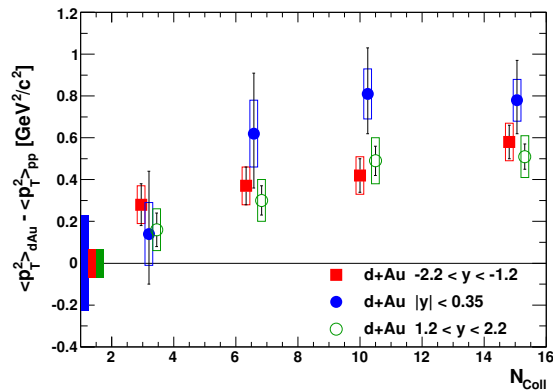


Figure 1.19: The difference between $\langle p_T^2 \rangle$ in $d+Au$ and $p+p$ collisions as function of a $\langle N_{\text{coll}} \rangle$ in $d+Au$ collisions [37].

Figure 1.18 shows R_{dA} of various hadrons (π , K , p , and ϕ) at mid-rapidity for different centrality classes [36]. In the most central (0–20%) d +Au collision, enhancements of hadron productions at moderate p_T range are observed. One interesting feature is that a clear baryon enhancement is observed which is similarly seen in Au+Au collisions. One hypothesis to explain this behavior is mass-ordering Cronin effect, but it is hard to explain the different R_{dA} between hadrons of similar masses, p (~ 938 MeV) and ϕ (~ 1019 MeV), shown in Fig. 1.18. Recombination model, which explain the baryon enhancement at intermediate p_T region by the recombination of low p_T partons, reproduces this data as well as the data from Au+Au collisions [38].

In addition to the result of light hadrons, the p_T broadening is also observed in J/ψ production from d +Au collisions. As shown in Fig. 1.19, there is a clear difference of $\langle p_T^2 \rangle$ between the data d +Au and p + p collisions at all rapidity ranges. The difference becomes larger as the average number of binary collisions increases.

1.2.3 Nuclear breakup

Quarkonia states are affected by another CNM effect, nuclear breakup. After production of quarkonia states, they interact with the intrinsic nuclear matter on the way out. A large suppression of J/ψ production at mid-rapidity was observed in the low energy fixed target experiments [40]. Since the crossing time through the nuclei is as long as the J/ψ formation time at lower energies, the possibility to breakup by the interaction with some nucleons increases [41]. Survival probability from the nuclear absorption can be formulated, by assuming that the

production and absorption of quarkonia states can be factorized and there is no A dependence,

$$S^{abs}(b, z) = e^{- \int_z^\infty dz' \rho_A(b, z) \sigma_{abs}(z-z')}, \quad (1.9)$$

where b is the impact parameter, z is the longitudinal position of the quarkonia production, ρ_A is the density of nucleus A , and σ_{abs} is the absorption cross section of quarkonia states. The suppression of J/ψ production is observed in all rapidity ranges and collision systems

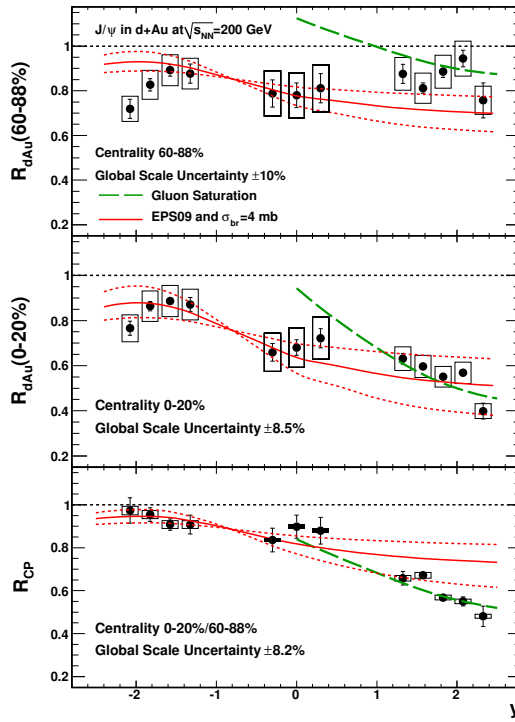


Figure 1.20: R_{dA} and R_{CP} of J/ψ as a function of rapidity and compared to theoretical calculations [39].

(d +Au, Cu+Cu, and Au+Au) from the PHENIX experiment [42]. These results indicate that there are additional factors causing the J/ψ suppression besides the HNM effects.

Figure 1.20 shows the R_{dA} and R_{CP} of J/ψ production at various rapidity ranges. Small suppression is observed in the most peripheral collisions (top panel) over the entire rapidity range, and the suppression at forward rapidity becomes larger in the most central collisions. Two different models, the gluon saturation and the EPS09 nPDF with a breakup cross section of 4 mb, fail to describe the R_{dA} and R_{CP} simultaneously. With these data, it is hard to conclude that how two factors, the suppression of charm production and the nuclear breakup, contribute to the J/ψ suppression seen in the data.

1.3 Heavy quark production

1.3.1 Theoretical framework

A leading order (LO) process for heavy quark production at RHIC energies is the gluon fusion, $g + g \rightarrow Q + \bar{Q}$, and Figure 1.21 shows detailed diagrams for the LO process [43]. Quark and anti-quark an-

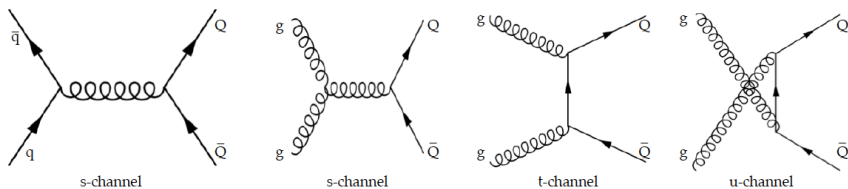


Figure 1.21: Leading order diagrams for heavy quark pairs production.

nihilation process, $q + \bar{q} \rightarrow Q + \bar{Q}$, is suppressed and treated as a next leading order (NLO), because the population of anti-quarks in proton is low [44]. Other NLO processes are $g + q \rightarrow Q\bar{Q}$, $g + \bar{q} \rightarrow Q + \bar{Q} + g$, $g + \bar{q} \rightarrow Q + \bar{Q} + \bar{q}$, and $g + g \rightarrow Q + \bar{Q} + g$. The cross section of LO processes shown in Fig. 1.21 are proportional to α_s^2 , and the NLO processes are order of α_s^3 .

Due to large mass of heavy quarks, the perturbative QCD (pQCD) can calculate the heavy quark production over the entire p_T range. Therefore, experimental measurements will provide an excellent test of this theoretical approach. By the assumption of factorization [45], the calculation of $Q\bar{Q}$ production from $p+p$ collisions can be separated into two independent parts of hard collisions between partons and non-perturbative parton densities. For the direct comparison with experimental measurements (e^\pm , $\mu^- \leftarrow D$, B), additional processes of fragmentation and decay are also considered in this calculation. The overall process can be shown as,

$$pp \xrightarrow{pQCD} Q\bar{Q} \xrightarrow{\text{fragmentation}} H_Q \xrightarrow{\text{decay}} l_{HF} \quad (1.10)$$

where $Q\bar{Q}$ is the heavy quark pair, H_Q is the hadron containing heavy quark, and l_{HF} is the lepton from decay of H_Q which can be measured experimentally.

The most common formula for the cross section of heavy quark production is,

$$\sigma Q\bar{Q} = \int dx_1 dx_2 f_i^{H_1}(x_2, \mu_F) f_j^{H_2}(x_1, \mu_F) \hat{\sigma}_{ij}(x_1 p_1, x_2 p_2, m_Q, \mu_F, \alpha_s) \quad (1.11)$$

where x is the Bjorken x of parton, f is the parton distribution function, $\hat{\sigma}$ is the partonic cross section, and μ_F is the factorization scale. Detailed description and proof of this factorization theorem for the heavy quark production from the deep inelastic scattering can be found in [46]. There are two important characteristics in this calculation as follows.

- The heavy quark masses are not negligible, if they are comparable with respect to the scale of hard scattering.
- The number of active light quark flavors (n_{lf}) in the strong coupling (α_s) is determined according to the physical scale.

The active light quarks are considered as partons of zero mass, and other quarks are treated to be massive. According to the magnitude of physical scale, e.g. Q^2 or p_T , the n_{lf} is determined. In case of charm, the n_{lf} is 3 for $p_T < m_{charm}$, and if $p_T > m_{charm}$, charm is included the active parton flavors ($n_{lf} = 4$). Two theoretical calculations for heavy quark production are approached. The first is a total cross section from the NLO calculation with $n_{lf} = 3$ [47]. Another approach is an integration of p_T and rapidity distributions from the Fixed-Order-Next-to-Leading-Log (FONLL) calculation with varying $n_{lf} = 3$ or 4 depending on p_T [48]. Detailed discussion of these two theoretical frameworks can be found in [49].

1.3.2 Heavy quark measurements at PHENIX

The PHENIX experiment has very good capabilities to study heavy quark production by measuring leptons from D and B mesons.³ Electrons from heavy-flavor decay are analyzed in the PHENIX central arms at mid-rapidity, and muons can be measured in the PHENIX muon arms at forward rapidity region. PHENIX has measured heavy quark production in various collision systems, and many interesting studies are still on going. In this section, the measurements of heavy quark production so far will be introduced.

In $p+p$ collisions

The measurement of heavy quark production in $p+p$ collisions is important for these reasons.

- Test of pQCD by comparing with theoretical calculations.
- Baseline measurement to the results in A+A or $d(p)+A$ collisions in order to study medium effects in such collision systems.

Figure 1.22 shows a p_T spectrum of heavy-flavor electrons at mid-rapidity measured in the PHENIX central arms [50]. The lines are from FONLL calculations [51, 52], and the lower panel shows the ratio of data to FONLL central curve. Upper and lower lines in the lower panel represent uncertainties of the FONLL calculation. The results show a good agreement with the FONLL curve over the entire measured p_T range.

³Due to limited acceptance for particle identification, there is no measurement from direct reconstruction with invariant mass technique.

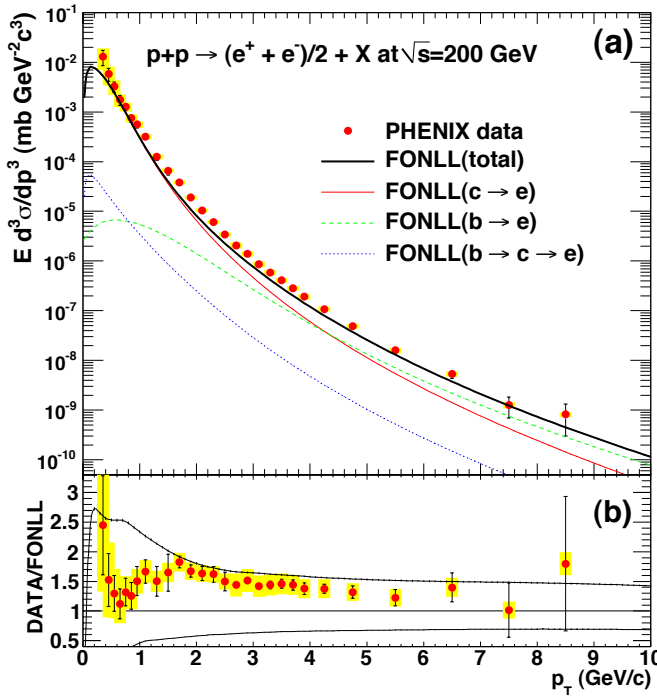


Figure 1.22: Heavy-flavor electron p_T spectrum in $p+p$ collisions at mid-rapidity and comparison with FONLL calculation [50].

Figure 1.23 shows charm ($c\bar{c}$) cross section as a function of rapidity in $p+p$ collisions. The total charm cross section at a certain rapidity is obtained from extrapolation down to $p_T = 0$ GeV/c of a normalized FONLL p_T curve to the measured data. As shown in the figure, the measured charm cross section is consistent with the FONLL estimation both at forward and mid-rapidity regions.

In heavy-ion collisions

In heavy-ion collision, heavy quarks are expected to lose less energy

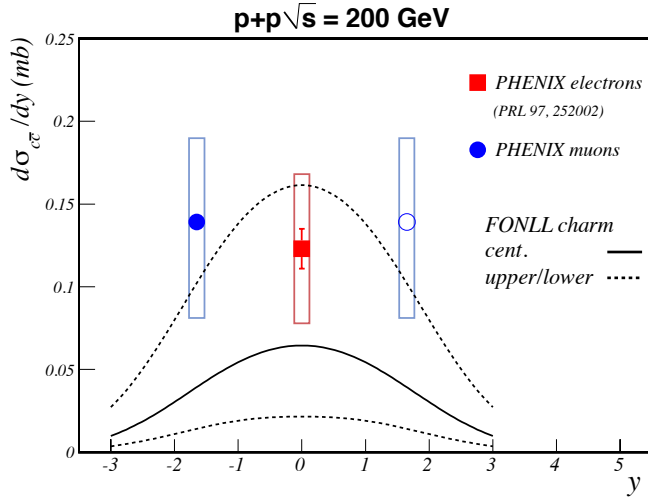


Figure 1.23: Charm cross section as a function of rapidity in $p+p$ collisions [53].

than light quarks when traversing the hot and dense medium. This is because the angle of gluon radiation decreases as increasing mass of the parton like $\theta < M_Q/E_Q$, known as the “dead cone effect” [54]. Therefore, this effect estimates the mass dependent energy loss, $R_{AA}^{u,d} < R_{AA}^c < R_{AA}^b$.

Figure 1.24 shows R_{AA} (upper) and v_2 (lower) of heavy-flavor electron and π^0 at mid-rapidity. On the contrary to the estimation of dead cone effect, a similar level of suppression is observed in R_{AA} of heavy-flavor electron and π^0 at $p_T > 5 \text{ GeV}/c$. At the time these results were obtained, electrons from charm and bottom can not be separated, so it is hard to verify the dead cone effect with the current data. At the lower panel in Fig. 1.24, significant v_2 is observed in heavy-flavor electrons. Especially at $p_T < 2 \text{ GeV}/c$, the v_2 of heavy-flavor electron is consistent with that of π^0 .

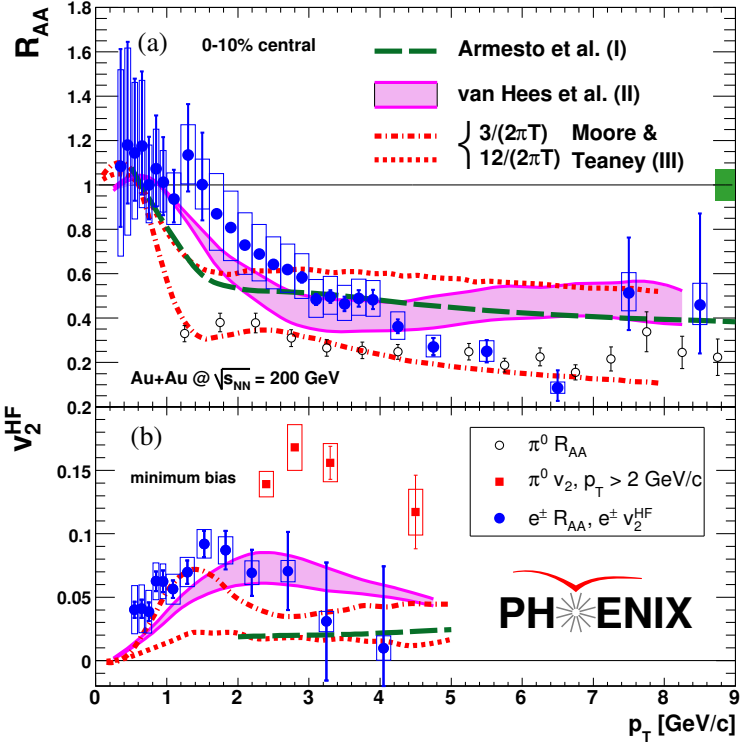


Figure 1.24: Nuclear modification factor R_{AA} (upper) and elliptic flow v_2 (lower) of heavy-flavor electrons in Au+Au collisions at mid-rapidity [55].

PHENIX also measured heavy-flavor lepton production in Cu+Cu collisions which is relatively smaller system than Au+Au collisions. Figure 1.25 shows R_{dA} of heavy-flavor electrons (mid-rapidity) and muons (forward rapidity) in central Cu+Cu collisions. Unlike the results in Au+Au collisions shown in Fig. 1.24, only mild suppression is observed at $p_T > 3$ GeV/c. Whereas, the heavy-flavor muon production at forward rapidity shows a larger suppression than the mid-rapidity results. This is interesting because the energy density (\propto multiplicity)

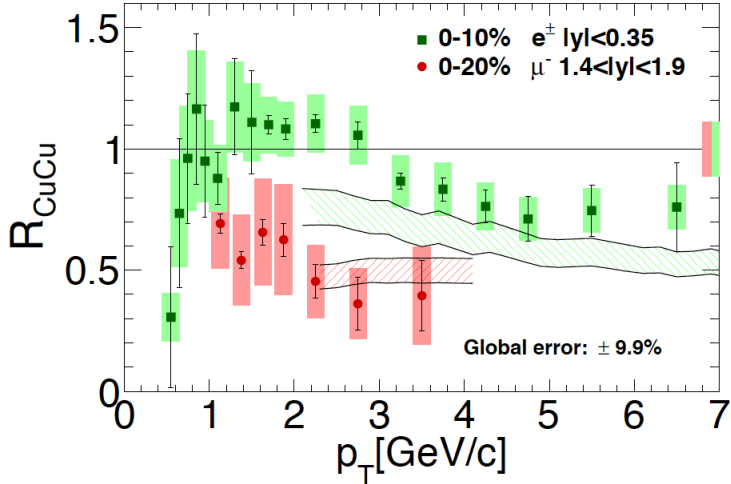


Figure 1.25: Nuclear modification factor R_{AA} of heavy-flavor leptons in central Cu+Cu collisions at mid (green squares) [56] and forward rapidity (red circles) [53].

is, on the contrary, larger at mid-rapidity. This large suppression at forward rapidity may suggest additional CNM effects, because pQCD calculations [57, 58] including the CNM effects reproduce the data at both rapidity reasonably well.

In d +Au collisions

The study of heavy quark production in d +Au collisions is important to understand and interpret the results from heavy-ion collisions. In heavy-ion collisions, both hot and cold nuclear matter effects exist, d +Au collisions with minimal effects of the QGP is needed as a control experiment. In addition, d +Au experiment itself is an excellent probe to study cold nuclear matter (CNM) effects as discussed in Sec. 1.2. In case of the measurement of heavy quark production whose leading-order process is gluon fusion, we can directly access to the information

of the gluon distribution in nucleus.

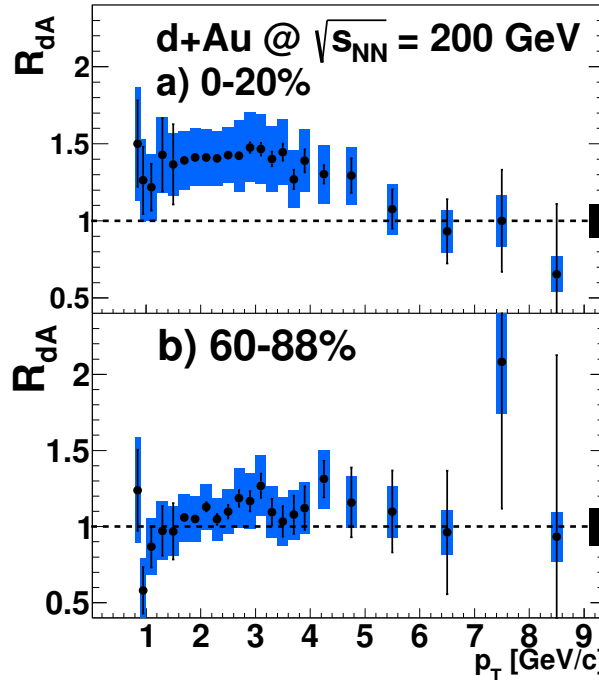


Figure 1.26: Nuclear modification factor R_{dA} of heavy-flavor electrons in central (upper) and peripheral $d+Au$ collisions at mid-rapidity [59].

Figure 1.26 shows the nuclear modification factor R_{dA} of heavy-flavor electrons measured at mid-rapidity [59]. In the most central (0–20%) $d+Au$ collisions, a clear enhancement is observed as shown in the upper panel, whereas R_{dA} is consistent with the unity in the most peripheral collisions. This enhancement at moderate p_T region in central $d+Au$ collision is probably related to the p_T broadening due to multiple scattering of partons. By comparing this $d+Au$ results with the heavy-ion results shown in Fig. 1.24, we can conclude that the suppression of

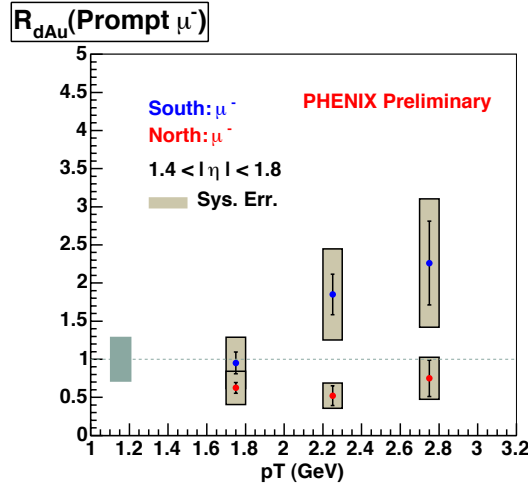


Figure 1.27: R_{dA} of heavy-flavor muons in MB d +Au collisions, which data was taken during the first d +Au run in 2003.

heavy quark production seen in Au+Au collision is due to the HNM effects.

At forward and backward rapidity range, the measurement of heavy quark production is more interesting, because the gluon distribution functions corresponding x ranges at forward and backward rapidity are strongly modified as described in Sec. 1.2.1. Figure 1.27 is the R_{dA} of heavy-flavor muons measured at the PHENIX muon arms. As shown in the figure, a suppression (enhancement) is observed at forward (backward) rapidity region which can be attributed to the gluon shadowing (anti-shadowing). However, the measurement is obtained in limited kinematic ranges and the systematic uncertainty is large due to the lack of statistics.

1.4 Motivation for this research

The primary purpose of this research is to measure muons from open heavy-flavor decay at forward and backward rapidity ranges in d +Au collisions. As discussed in the previous section, heavy quark production has been measured in various collision systems so far. However, there are some missing blocks to complete the whole picture of heavy quark measurement in PHENIX. One is in d +Au collisions at forward rapidity, and another is in Au+Au collisions at forward region too.

Unfortunately in current experimental setup, the heavy-flavor muon analysis with the PHENIX muon arms has lots of difficulties like large combinatorial background tracks. In case of the analysis with d +Au data, it suffers less from the combinatorial backgrounds because of much smaller multiplicity than that in heavy-ion collisions. Moreover, the results in d +Au collision will be more interesting due to following reasons.

- At mid-rapidity, a clear enhancement of heavy quark production is observed in central d +Au collisions [59] as shown in Fig. 1.26. The results at forward and backward rapidity will provide the essential information of how the CNM affects heavy quark production depending on rapidity.
- In Cu+Cu collisions, the larger suppression is observed at forward rapidity than mid-rapidity region as shown in 1.25 [53, 56]. In addition, the level of suppression seen at forward rapidity is comparable with the suppression in central Au+Au collisions

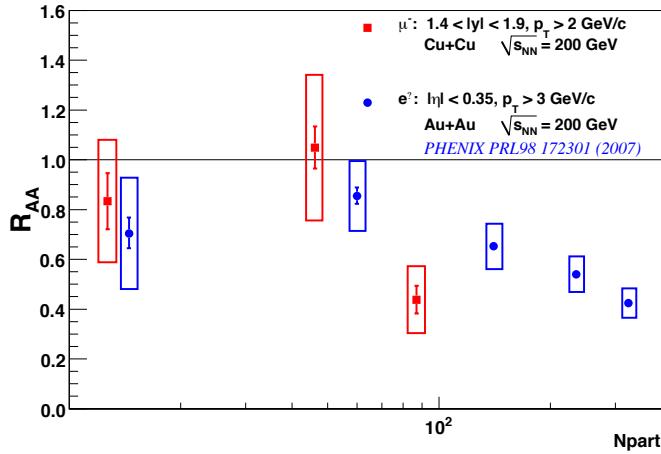


Figure 1.28: Comparison of R_{AA} as a function of N_{part} in Au+Au (mid-rapidity) and Cu+Cu (forward rapidity) collisions at $\sqrt{s_{NN}} = 200$ GeV [53].

which means,

$$R_{\text{AuAu}, \langle N_{\text{coll}} \rangle \approx 955}^{\text{mid}} \sim R_{\text{CuCu}, \langle N_{\text{coll}} \rangle \approx 152}^{\text{forward}}.$$

The CNM effects may contribute to the large suppression at forward region.

- The measurement of heavy quark production will help to understand the quarkonia production, especially about the nuclear breakup discussed in Sec. 1.2.3.

Chapter 2

Experimental setup

2.1 RHIC

The relativistic heavy ion collider (RHIC), which is dedicated to ultra-relativistic heavy ion collisions, is located at Bookhaven National Laboratory (BNL) in New York. As shown in the whole view Fig. 2.1, RHIC consists of two super-conducting rings (yellow and blue) of 3.8 km in circumference. Heavy ions start from Van de Graaff, and protons are generated at the proton linear accelerator, referred to as proton linac. These generated heavy-ions and protons are injected to the Alternating Gradient Synchrotron (AGS), which is a historic experimental site to observe J/ψ , and accelerated up to ~ 10 GeV/c per nucleon. Then these beams traverse to the RHIC finally, and they are maximumly accelerated up to 100 GeV/c (255 GeV/c) for heavy ions (protons). Table 2.1 shows the history of RHIC runs from 2000 including beam species, collision energies, and the integrated luminosities

which PHENIX collected.

At the starting point of RHIC, 2000, four experiments were in operation: BRAHMS, PHENIX, PHOBOS, and STAR. Two small experiments, BRAHMS and PHOBOS, were stopped taking data after publishing lots of global measurements. Now, only two large experiments, PHENIX and STAR, are actively working on taking data and further upgrades for enhanced performances.

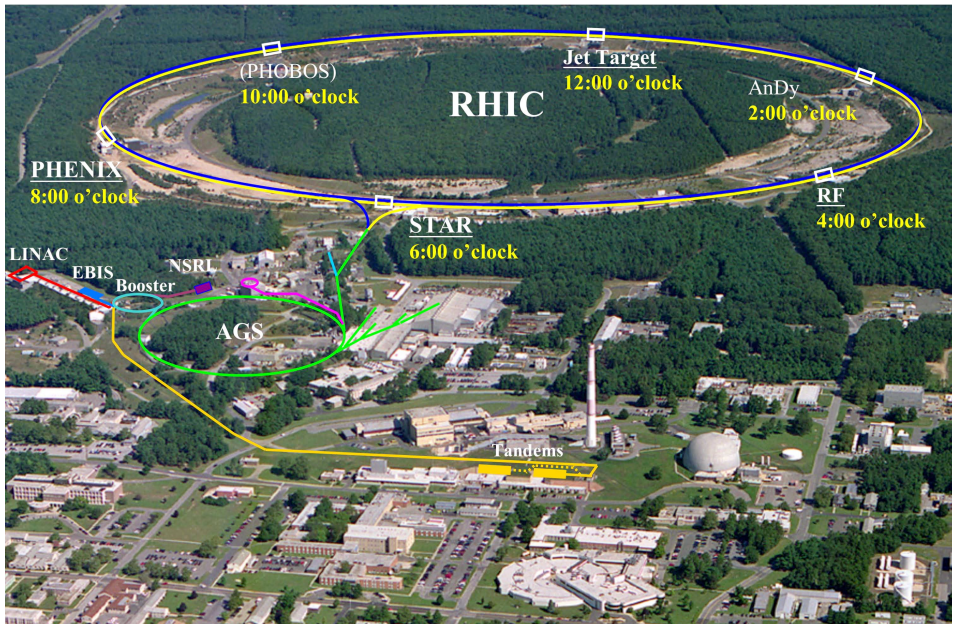


Figure 2.1: View of the RHIC facility

Table 2.1: History of RHIC runs from 2000 to now showing beam species, CM energy and sampled luminosity by PHENIX.

| RHIC Run | Year | Beam Species | Energy | $\int L dt$ |
|----------|--------|--------------|----------|-------------------|
| Run-1 | 2000 | Au+Au | 130 GeV | $1 \mu b^{-1}$ |
| Run-2 | 2001-2 | Au+Au | 200 GeV | $24 \mu b^{-1}$ |
| | | $p+p$ | 200 GeV | $150 nb^{-1}$ |
| Run-3 | 2002-3 | $d+Au$ | 200 GeV | $2.74 nb^{-1}$ |
| | | $p+p$ | 200 GeV | $0.35 nb^{-1}$ |
| Run-4 | 2003-4 | Au+Au | 200 GeV | $241 \mu b^{-1}$ |
| | | Au+Au | 62.4 GeV | $9 \mu b^{-1}$ |
| Run-5 | 2005 | Cu+Cu | 200 GeV | $3 nb^{-1}$ |
| | | Cu+Cu | 62.4 GeV | $0.19 nb^{-1}$ |
| | | Cu+Cu | 22.4 GeV | $2.7 \mu b^{-1}$ |
| Run-6 | 2006 | $p+p$ | 200 GeV | $10.7 pb^{-1}$ |
| | | $p+p$ | 62.4 GeV | $100 nb^{-1}$ |
| Run-7 | 2007 | Au+Au | 200 GeV | $813 \mu b^{-1}$ |
| Run-8 | 2007-8 | $d+Au$ | 200 GeV | $80 nb^{-1}$ |
| | | $p+p$ | 200 GeV | $5.2 pb^{-1}$ |
| Run-9 | 2009 | $p+p$ | 200 GeV | $16 pb^{-1}$ |
| | | $p+p$ | 500 GeV | $14 pb^{-1}$ |
| Run-10 | 2010 | Au+Au | 200 GeV | $1.3 \mu nb^{-1}$ |
| | | Au+Au | 62.4 GeV | $100 \mu b^{-1}$ |
| | | Au+Au | 39 GeV | $40 \mu b^{-1}$ |
| | | Au+Au | 7.7 GeV | $260 mb^{-1}$ |
| Run-11 | 2011 | $p+p$ | 500 GeV | $27 pb^{-1}$ |
| | | Au+Au | 200 GeV | $915 \mu b^{-1}$ |
| | | Au+Au | 27 GeV | $5.2 \mu b^{-1}$ |
| | | Au+Au | 19.6 GeV | $13.7 M evts$ |
| Run-12 | 2012 | $p+p$ | 200 GeV | $9.2 pb^{-1}$ |
| | | $p+p$ | 510 GeV | $30 pb^{-1}$ |
| | | U+U | 193 GeV | $171 \mu b^{-1}$ |
| | | Cu+Au | 200 GeV | $4.96 nb^{-1}$ |
| Run-13 | 2013 | $p+p$ | 510 GeV | $240 pb^{-1}$ |

2.2 PHENIX experiment

Pioneering High Energy Nuclear Interaction eXperiment (PHENIX) is one of the largest heavy-ion physics experiments. Figure 2.2 is an illustration of the PHENIX detector. Two beams inside the beam pipe collide at the interaction point (IP) where the center of the PHENIX detector. The z -axis of the global PHENIX coordinate is along the beam pipe, and North side (right in the Fig. 2.2) corresponds to the positive z direction. The IP is the center, $(0,0,0)$ of the PHENIX coordinate system.

The PHENIX detector is composed of two main parts and other global detectors. First main part shown in the top panel in Fig. 2.4, called “central arms” [60, 61], consisting of two sets of detectors: Drift Chambers (DC), Pad Chambers (PC), Ring-Imaging Cherenkov detectors,

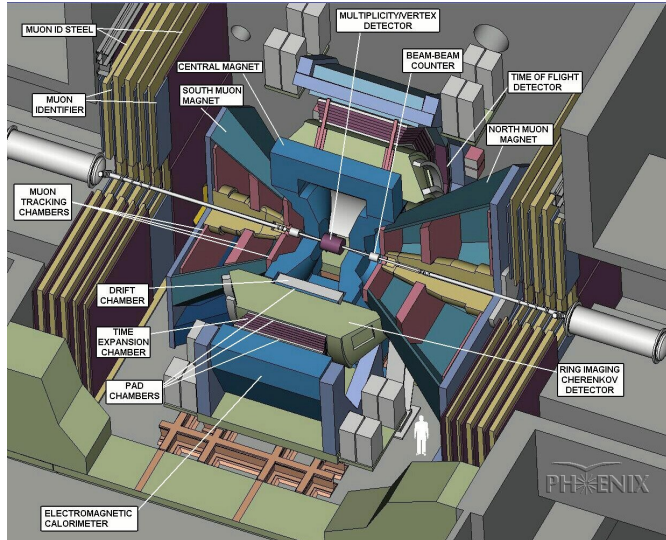


Figure 2.2: illustration of the entire PHENIX detector.

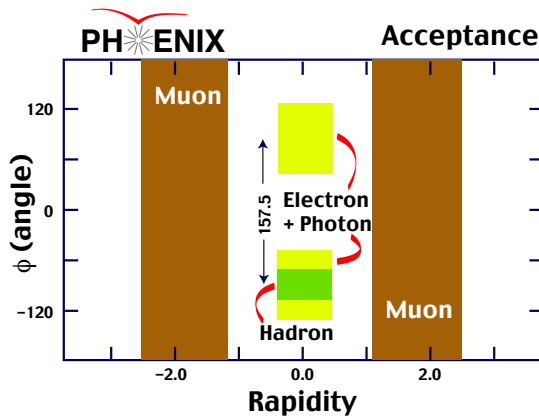


Figure 2.3: The kinematic acceptance of the PHENIX detector.

Electromagnetic Calorimeter (EMCal), Time Expansion Chamber (TEC) and, Time-of-Flight (TOF) detector. Each arm, West or East arm, is located symmetrically, and its kinematic coverage is $|\eta| < 0.35$ in pseudo-rapidity and π angle in azimuth shown in Fig. 2.3. The central arms have capabilities of measuring electrons, photons, and identified charged hadrons.

Another main part is a pair of muon spectroscopy [62], referred to as the North and South muon arm shown in the bottom panel of Fig. 2.4. Each muon arm consists of a muon tracker (MuTr) and a muon identifier (MuID) for momentum measurement and hadron/muon separation. Both muon arms cover full azimuthal angle, and η coverage for the North (South) arm is $1.2 < \eta < 2.4$ ($-2.2 < \eta < -1.2$). The muon spectroscopy is the mainly used subsystem in this analysis, so the details are described in the section 2.3.

There are also global detectors for event characterization, e.g. event collision vertex, collision centrality, and reaction plane. Two Beam

Beam Counter (BBC) detectors [63], composed of 64 quartz Cherenkov radiators with a photomultiplier tube, are located at far forward region ($3.0 < |\eta| < 3.9$). From the time difference between two BBC detectors of arriving charged particles from the collision point, the event start time and the collision (event) vertex are determined. Depending on how many charged particles are detected in the BBC, resolution of the event vertex varies between 0.5 cm for heavy-ion collisions and 2.0 cm for $p+p$ collisions.

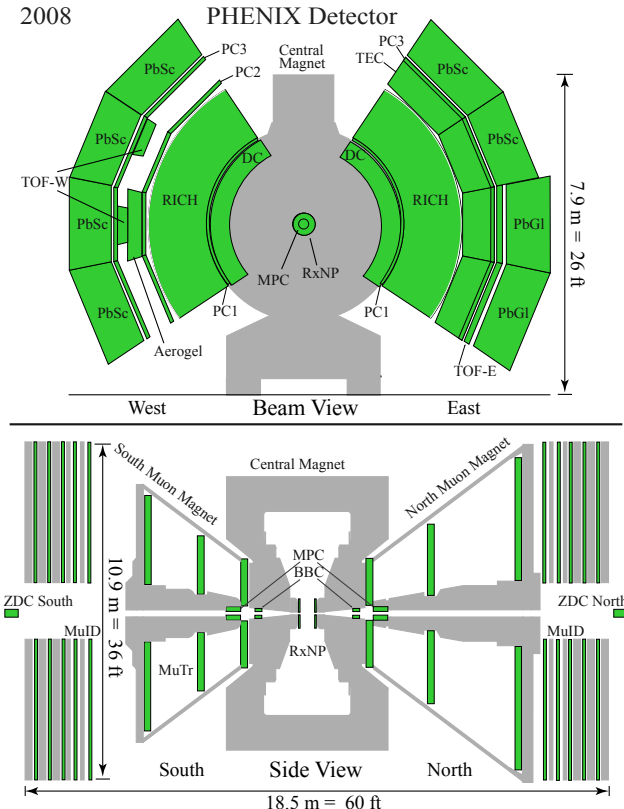


Figure 2.4: illustration of the entire PHENIX detector.

2.3 Muon arms

As briefly described in the former section, the PHENIX muon arms consist of two spectrometer at forward (North arm, $1.2 < \eta < 2.4$) and backward (South arm, $-1.2 < \eta < -2.2$) rapidity regions. Each muon arm is comprised of a muon tracker (MuTr) inside magnetic field followed by a muon identifier (MuID). The combination of these subsystems provides capabilities of the precise measurements of momentum and the separation of hadron/muon.

In front of each muon arm, ~ 80 cm of a nosecone absorber is located to reject hadrons suffering from the nuclear interaction with the absorber materials. Figure 2.5 is a map of the absorber materials in the muon arm. The nosecone absorber ($\sim 5\lambda_I$) and additional 5 layers of absorber between MuID gaps ($\sim 5\lambda_I$) significantly suppress hadron tracks. After traversing all these absorbers, pion contamination in the identified muons at the last MuID gap is typically $\sim 3 \times 10^3$.

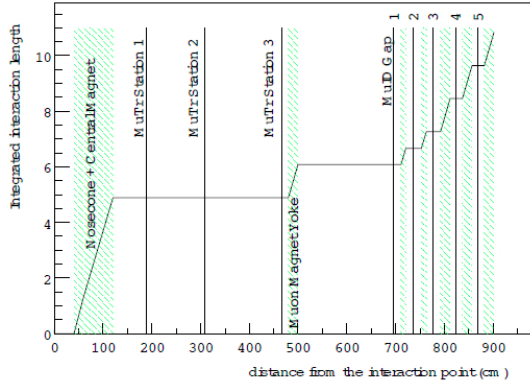


Figure 2.5: Location of absorbers in the muon arm along the z -direction from the interaction point.

2.3.1 Muon tracker

The muon tracker (MuTr) is designed, with its spatial resolution of $\sim 100 \mu\text{m}$ corresponding to the relative mass resolution of $\sigma(M)/M = 6\%/\sqrt{M}$, to provide the capability for separation of ρ/ω from $\phi, J/\psi$ from ψ' as well as Υ from Υ' . The MuTr, placed inside the muon magnet as shown in 2.4, consists of three stations of cathode strip read-out chambers as shown in 2.6.

First two stations (Station 1 and 2) are comprised of three layers, and the last station (Station 3) is composed of 2 layers. The Station 2 and 3 are divided into 8 segments (called octants), and the Station 1 contains 4 segments (called quadrants)¹. Figure 2.7 shows the details

¹station 1 is divided into 4 segments electrically to match next two stations

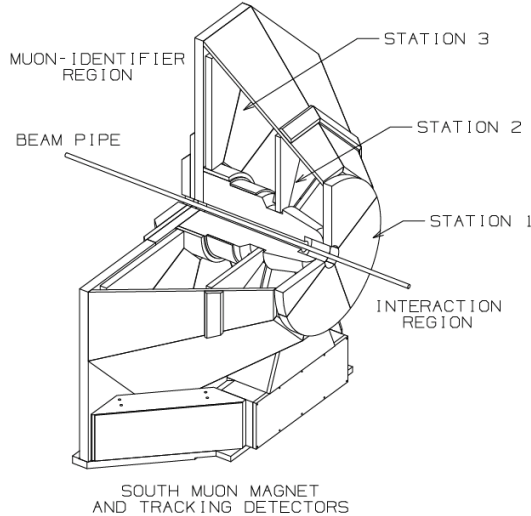


Figure 2.6: Drawing of the South muon tracker. Muons from the interaction point (right side) proceed toward the muon identifier located on the left (not shown).

numbering scheme of the MuTr stations.

Each of three MuTr stations was produced by a specific technology to achieve the accurate cathod patterns better than $25 \mu\text{m}$. For mechanical construction of the MuTr Station 1, 2, and 3, photolithograph, electro-mechanical etching, and mechanical routing are used, respectively. The Station 1 is placed at the closest position from the interaction point, so it is expected to have the highest occupancy per strip and the most stringent requirement ($> 95\%$) on dead area in the detector acceptance. The quadrants consist of three chamber gaps, and each gap includes a pair of cathode strip layers on either side of an anode wire layer.

The layers of Station 2 were made of etched $25 \mu\text{m}$ copper coated, which thickness is 600 \AA , mylar foils in order to avoid degradation of the momentum resolution. All cathode and anode planes are attached to the laminated frames, which thickness is 3.175 mm , to restrict radiation length (X_0) of the materials under 0.1% . The Station 3 consists of two gaps containing one anode wire plane in between two cathode read-out planes. The cathode strips are made by mechanically routing shallow lines in the copper skin.

The MuTr measures the momentum of charged particles by the simple Lorentz force law using the trajectory of a charged track (sagitta) in a magnetic field. When a charged particle enters inside the MuTr, only the component of its velocity perpendicular to the direction of magnetic field is affected by the Lorentz force. Then, the momentum of this charged particle is obtained as:

$$p = q \cdot B \cdot R \quad (2.1)$$

where q is the charge number, B is the magnitude of magnetic field, and R is the radius of the induced circular trajectory.

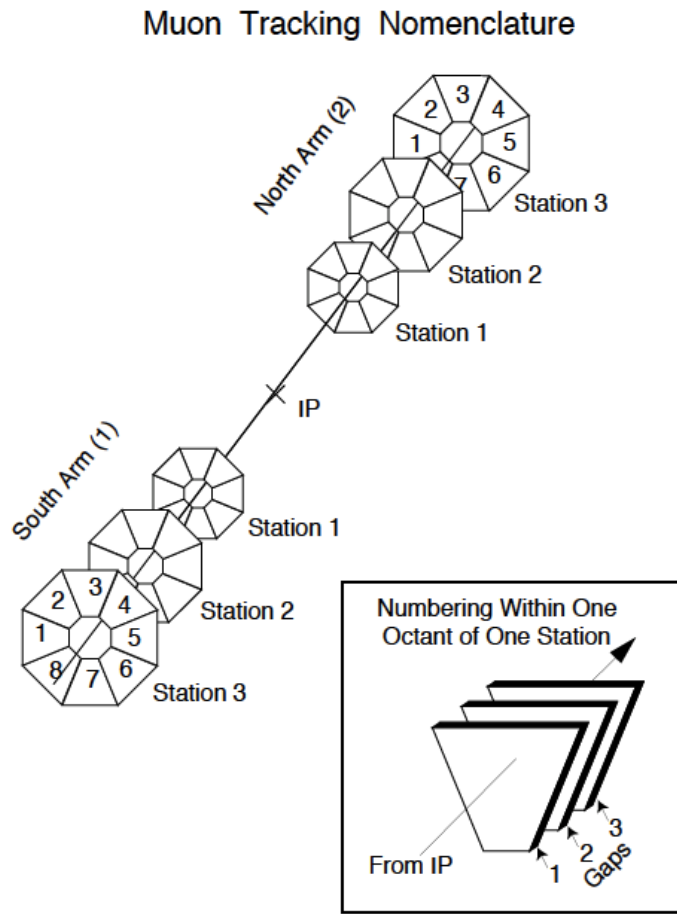


Figure 2.7: Illustration of the numbering scheme of the MuTr statios and octants.

2.3.2 Muon identifier

The primary purpose of the MuID is to enhance muon/hadron separation from the irreducible μ/π ratio, 1×10^{-3} , due to weak decay of pions before reaching the nosecone absorber. The thickness of absorber materials in the MuID is decided to decrease the punch-through hadrons to 1/4 of the irreducible μ/π ratio, that is 2.5×10^{-4} . As the nosecone absorber provides the rejection of pion about $\sim 10^{-2}$, another 90 cm ($\sim 5\lambda_I$) of absorber materials are needed in the MuID to achieve the factor of 1/4, which provides significant suppression in the muon pair background for J/ψ measurement.

Each MuID consists of five alternating steel absorber and multi-wire chamber as shown in Fig. 2.4. The position on the z -axis of all MuID gaps and the width of installed absorbers as shown in Fig. 2.5 are listed in Table 2.2. Since the total amount of absorber in the South

Table 2.2: The coordinate of all MuID gaps from the interaction point, $(0,0,0)$, and widths of an absorber in front of each gap.

| Arm | Gap | Front z (cm) | Back z (cm) | Absorber width (cm) |
|-------|-----|----------------|---------------|---------------------|
| North | 0 | 686.96 | 704.24 | 30 |
| North | 1 | 728.46 | 745.74 | 10 |
| North | 2 | 768.76 | 786.04 | 10 |
| North | 3 | 815.86 | 833.14 | 20 |
| North | 4 | 861.36 | 878.64 | 20 |
| South | 0 | -686.96 | -704.24 | 20 |
| South | 2 | -768.76 | -786.04 | 10 |
| South | 3 | -815.86 | -833.14 | 20 |
| South | 4 | -861.36 | -878.64 | 20 |

arm is 10 cm less than that in the North arm, the contamination of punch-through hadrons probably larger in the South arm.

As shown in Fig. 2.8, each MuID gap is comprised of six overlapping panels labeled A through F. Each MuID gap is filled with Iarocci tubes which are planar drift tubes, operated in proportional mode, consisting of gold-coated CuBe anode wires at the center of a graphitecoated plastic cathode. Figure 2.9 shows a cross section of the MuID panel and the plastic tubes (two-pack). A two-pack is a pair of tubes attached together and staggered by the half of one channel in order to increase

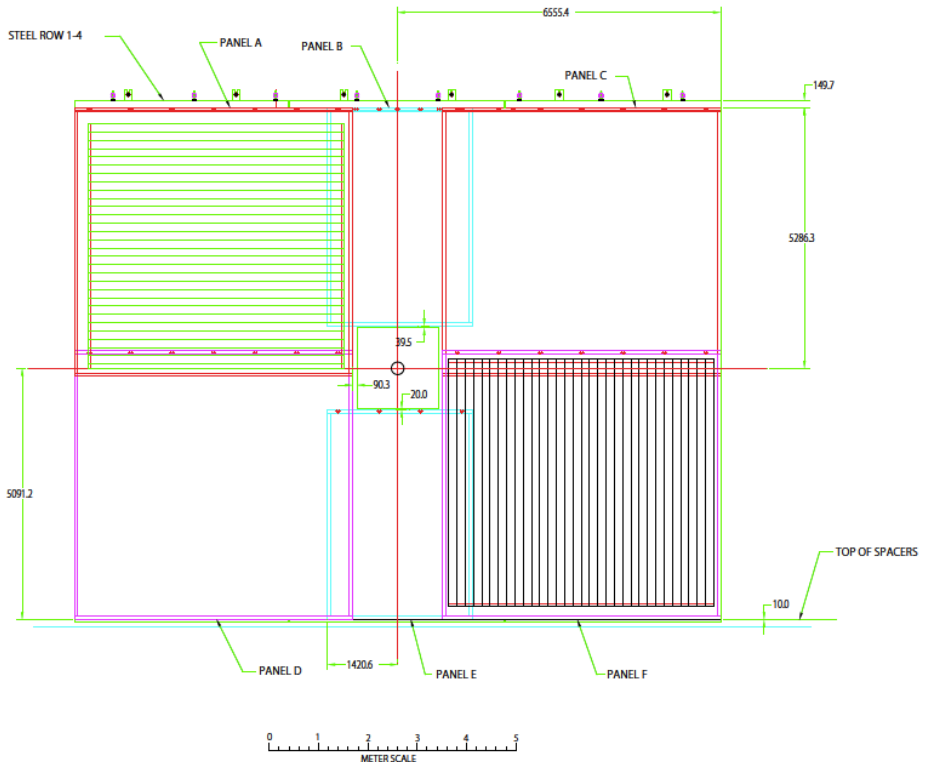
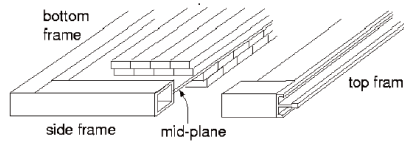
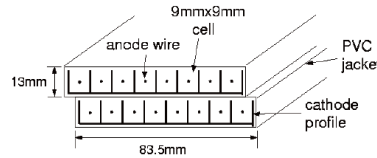


Figure 2.8: Drawing of one MuID gap which consist of six panels.



Cross section of the MuID panel



Cross section of the plastic tube(2-pack)

Figure 2.9: Cross section of the MuID panel (top) and the plastic tubes called a two-pack (bottom).

the efficiency. This two-pack is the most fundamental element of the MuID. As shown in the top panel of Fig. 2.9, groups of horizontally or vertically oriented two-packs form a MuID panel, and the total number of two-packs in MuID gaps at one arm is 3170. The large panels (A, C, D, and F) at 4 corners of the gap contain 118 horizontal and 128 vertical tubes, respectively. Two small panels (B and E), placed above and below the square hole, include 90 horizontal and 52 vertical tubes, respectively.

2.4 Track reconstruction

Information of tracks collected by the MuTr and the MuID detectors are combined together, and track reconstruction is performed offline. The track reconstruction starts from finding *roads* in the MuID. At first, one-dimensional roads are built from the clusters along the MuID

gaps oriented in horizontal or vertical direction. The road finding algorithm is recursive, it starts from pairs (one of each orientation) of clusters in the MuID Gap-1 and 2 (numbering from 0) and searches another pairs at both sides in the MuID Gap-0 and 3. Each one-dimensional MuID road is extended to the MuID Gap-4, fitted with a straight line. Finally, two-dimensional roads, contains information of position and direction, are formed with pairs of one-dimensional roads. These combined two-dimensional MuID roads are filtered with a few of criteria:

- difference of depth bewteen the horizontal and vertical one-dimensional roads should be zero or one.
- each one-dimensional road should have hits at least in two gaps.
- difference of number of hits between horizontal and vertical one-dimensional roads less than three.

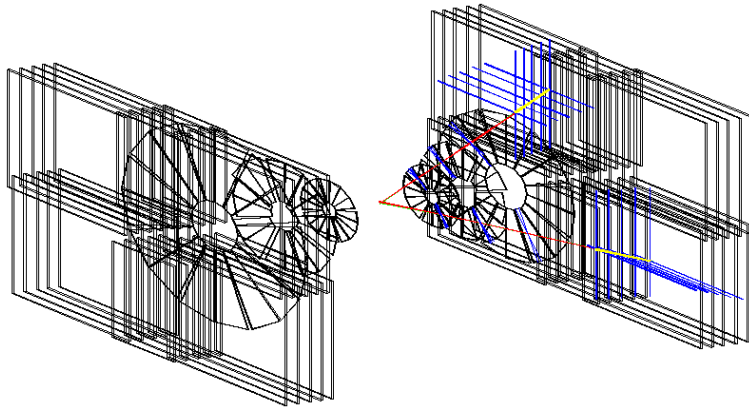


Figure 2.10: Event display of single J/ψ showing the full muon arm reconstruction.

- the minimum depth of a MuID road is Gap-2.

In order to minimize combinatorial background tracks in the muon reconstruction, the MuID roads are used as seeds and trace back to the MuTr. The details about MuID road finding are described in [64].

After calibration of all raw data from the MuTr, adjacent hits in the MuTr are grouped into *clusters*. Because one to three adjacent cathode strips normally fired, when a single track pass through the MuTr. The cluster finding is performed by scanning all over hits on a certain octant of a MuTr cathode. When a new hit is scanned, the position of previous cluster is checked whether a new hit is adjacent or not. If it is, a new hit is added to the previous cluster, otherwise a new cluster is registered.

The loop is started from the MuTr Station 3 and moves to Station 2 and 1. The position of clusters can be derived with sets of fired cathode strips, because two cathode strips within a gap, oriented at stereo angles to another, can provide a two-dimensional coordinate shown in Fig. 2.11. Clusters in two or three gaps, located together

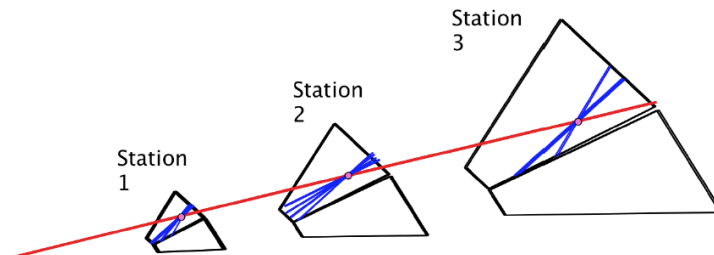


Figure 2.11: Event display of a single track in the MuTr. Blue lines in the MuTr gaps are fired cathode strips, and pink points are MuTr stubs.

within a few cm, in each MuTr station are combined to form MuTr *stubs* by fitting with a simple linear function.

The track finding algorithm in the MuTr starts from trying to find all MuID roads at Gap-0 which match a stub in the MuTr Station 3. When there is a match of a MuID road and a stub in the MuTr station 3, further attempts start to find stubs in Station 2 and 1. Reconstructed tracks are projected back to the interaction point through the nosecone absorber to determine the vertex positions and the momentum at collision points of tracks. Figure 2.11 shows a reconstructed MuTr track (red line), MuTr stubes (pink points) corresponding to fired cathode strips (blue lines).

2.5 Event triggers

In order to have efficient data taking of meaningful events, PHENIX uses various level-1 triggers. There are 32 slots for the level-1 triggers, and each trigger operate separately to take events of interest. The PHENIX level-1 trigger system [65] operates every beam crossing and generates a trigger bit to accept or reject a event within ~ 40 beam crossing. The local level-1 (LL1) triggers communicate with the associated subsystems and follow different trigger algorithms for own subsystems. The global level-1 (GL1) collects information from the LL1 and generates the decision of *accept/reject* based on combination of the LL1 information. When the level-1 trigger decides to take a event, a signal of “dead for X beam crossing” is also issued. In order to allow tracking chambers to collect signals with enough time and avoid taking fake events due to noise after taking a real event, the

Table 2.3: A short list of triggers applied during the Run-9 data taking of $p+p$ collisions at $\sqrt{s} = 200$ GeV. The scale down factors are set depending on trigger and beam luminosity.

| Name | Scale down | Scaled count |
|----------------------------------|------------|--------------|
| BBCLL1(>0 tubes) | 589 | 1192547 |
| BBCLL1(noVertexCut) | 1001 | 1360582 |
| (MUIDLL1_S1H)&BBCLL1(noVtx) | 18 | 226225 |
| (MUIDLL1_N1H)&BBCLL1(noVtx) | 18 | 276991 |
| (MUIDLL1_N1D S1D)&BBCLL1(noVtx) | 14 | 479256 |

next *accept* trigger will not be generated during the “dead for X beam crossing”.

Table 2.3 shows a list of triggers which are used to take events analyzed in this research. The scale down factor means the number of skipped events after taking one event. For example, if a scale down factor is N , only one event are recorded from $N + 1$ triggered events. This is due to the limited rejection power of a certain trigger and the data acquisition bandwidth. There are three categorizations for each trigger: raw, live, and scaled. The raw triggered events are the events satisfied the condition of a certain trigger. If the raw trigger is not generated during the “dead for X beam crossing”, which means this event can be recorded, it is also the live trigger. Among the events flagged the live trigger, one of $N + 1$ events is actually recorded according to the pre-selected scale down factor, N .

2.5.1 Minimum bias trigger

The minimum bias (MB) trigger uses the BBC. The standard condition is that both the South and North BBC modules have more than one hit. The MB trigger also has a requirement of the collision vertex. Depending on the vertex range, BBCLL1(>0 tubes) (± 30 cm), BBC(noVertexCut) (no vertex position requirement), and BBCLL1(narrowVtx) ($\pm 10 \sim 15$ cm) are used.

The MB trigger efficiency (ϵ_{BBC}^{MB}) in the PHENIX for $p+p$ collisions at $\sqrt{s} = 200$ GeV is $55 \pm 5\%$ [66]. That is, the MB events sampled 23.0 ± 2.2 mb of the total $p+p$ inelastic cross section. In case of $d+Au$ collisions, the ϵ_{BBC}^{MB} is $88 \pm 4\%$ [67]. In order to calculate correct invariant yield, the efficiency of BBC trigger for events containing specific tracks, which are heavy-flavor muons in this research, should be also determined. This efficiency was determined by using π^0 measurement at mid-rapidity, and the values are 79% and 99% for $p+p$ and $d+Au$ collisions, respectively. This bias factor is applied to the measured invariant yield as:

$$Y^{true} = Y^{measured} \cdot \frac{\epsilon_{BBC}^{MB}}{\epsilon_{BBC}^{HF \rightarrow \mu}} \quad (2.2)$$

where $\epsilon_{BBC}^{HF \rightarrow \mu}$ is the BBC efficiency for events containing a heavy-flavor muon.

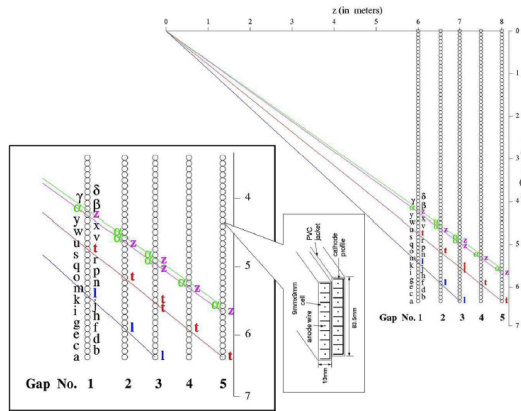


Figure 2.12: Symsets configuration for the MuID local level-1 trigger.

2.5.2 MuID local level-1 trigger

The data sets used in this research are taken with combinations of the MB trigger and two MuID local level-1 (MuIDLL1) triggers: MuID 1-Deep and MuID 1-Hadron. The MuIDLL1 uses hit patterns of each horizontal and vertical MuID gaps. For each set of oriented gaps, two packs in the MuID Gap-0 are virtually grouped, and lines are projected from the interaction point, $(0,0,0)$, to the Gap-4 through the grouped two packs in the Gap-0 as shown in Fig. 2.12. The logical tubes, within a certain range from the intersected tube on the projected line, are formed in each gap, and this set of logical tubes is called *symset*.

For every event, MuIDLL1 algorithm checks all symsets formed in the entire MuID. Figure 2.13 shows symset logics for the two MuIDLL1 triggers. If any of two symset logics is satisfied, the MuIDLL1 generates an *accept* trigger bit. The MuIDLL1-1D (deep) trigger, shown in the left panel in Fig. 2.13, is for tagging events containing muon candidates. The MuIDLL1-1H (hadron) trigger is a newly adopted trigger

instead of MuIDLL1-1S (shallow) trigger from the Run-8 for tagging stopped hadron candidates. As shown in the right panel in Fig. 2.13, the symset logic generate a *reject* decision, if there are any hits in the MuID Gap-4.

2.6 Centrality determination

Collision geometry in single d +Au collision is quantified by using *centrality* from 0 (most central, d collides the center of Au nucleus) to 100% (most peripheral, d collides the very edge of Au nucleus). The value of centrality is defined as a percentage of the total charges deposited in the South BBC, which is Au-going side, shown in Fig. 2.14. Based on this distribution, 0–20% central events mean the 20% events which deposit largest charges in the South BBC (red area in Fig. 2.14.).

For each centrality class, the average number of binary collisions ($\langle N_{\text{coll}} \rangle$) is determined by using a Glauber model calculation [68] and simulation with the BBC. The BBC response for each binary collision is described reasonably well by a negative binomial distribution (NBD). By fitting

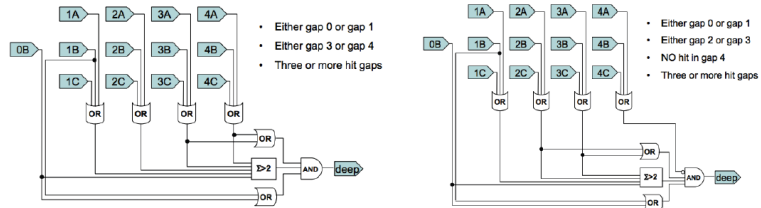


Figure 2.13: Symset logic for MuID local level-1 triggers. The left symset logic is for MuID-1D (deep) trigger, and the right symset logic is for MuID-1H (hadron) trigger.

the BBC response in the real data with the NBD distribution at a region of $\sim 100\%$ MB trigger efficiency, the BBC trigger efficiency can be obtained. The bias factor (ϵ_{BBC}) already described in Section 2.5.1 as well as the $\langle N_{\text{coll}} \rangle$ for each centrality class are listed in Table 2.4. As shown in Fig. 2.15, the distributions of N_{coll} for different centrality classes are largely overlapped each other.

The bias factor corrects both the MB trigger efficiency and bias in the centrality determination of a $d+\text{Au}$ collision. The Galuber model is also used for determination of the bias factors. For this calculation, it is assumed that only one of N binary collisions produces charges (characteristic of a hard process) in the BBC, and rest $N-1$ binary collisions are soft processes. The actual increase of charges in the BBC is tuned by using the real data. By applying the simple value of bias factor for a corresponding centrality class, both BBC efficiency of triggering the MB events and the events containing a heavy-flavor muon, and the centrality determination are corrected.

Table 2.4: Characterization of the collision centrality in $d+\text{Au}$ collisions and corresponding bias correction factor ϵ_{BBC} .

| Centrality bin | $\langle N_{\text{coll}} \rangle$ | ϵ_{BBC} | $\epsilon_{BBC}/\langle N_{\text{coll}} \rangle$ |
|----------------|-----------------------------------|-------------------|--|
| 0–20% | 15.1 ± 1.0 | 0.94 ± 0.01 | 0.062 ± 0.003 |
| 20–40% | 10.2 ± 0.7 | 1.000 ± 0.006 | 0.098 ± 0.004 |
| 40–60% | 6.6 ± 0.4 | 1.03 ± 0.02 | 0.157 ± 0.008 |
| 60–88% | 3.2 ± 0.2 | 1.03 ± 0.06 | 0.33 ± 0.02 |
| 0–100% | 7.6 ± 0.4 | 0.889 ± 0.001 | 0.117 ± 0.004 |

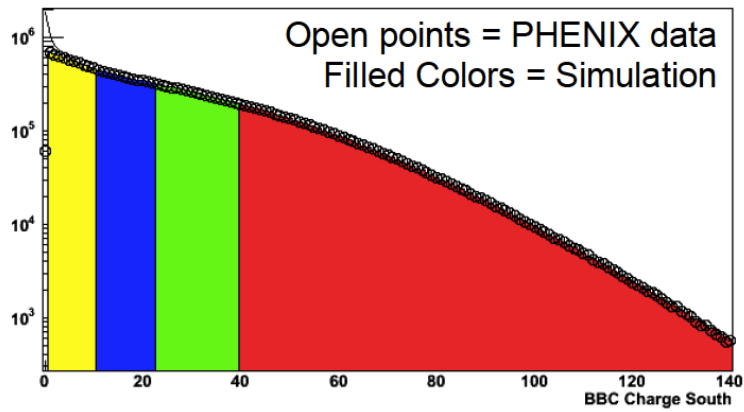


Figure 2.14: The deposited charge distribution at the South BBC (open circle) in d +Au collisions with comparison to simulation (filled color). Each color mean a different centrality class.

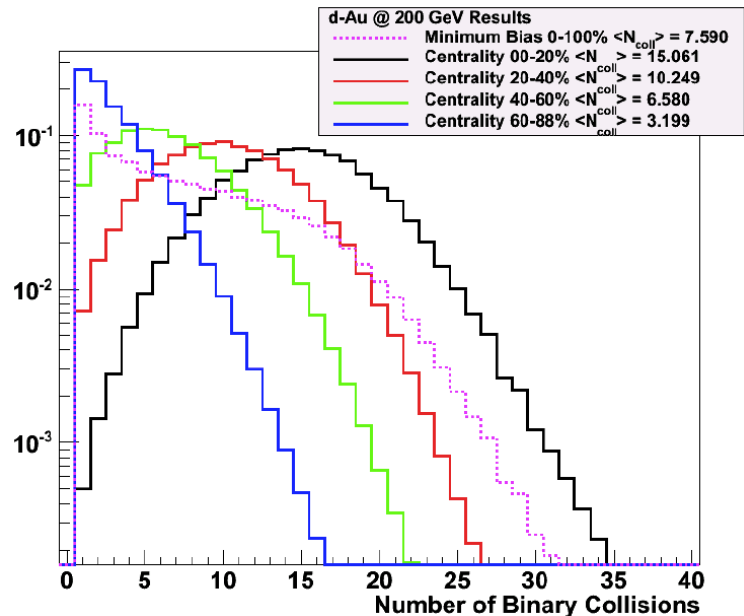


Figure 2.15: Distribution of $\langle N_{coll} \rangle$ for 5 different centrality classes in d +Au collisions.

Chapter 3

Heavy-flavor muon analysis

3.1 Analysis overview

The main purpose of this analysis is to measure single muons from heavy-flavor mesons with the muon spectroscopy in PHENIX. The first heavy-flavor muon analysis had been approached with data from $p+p$ collisions collected during the RHIC Run-2, and this analysis was developed by second analysis with data from $p+p$ and Cu+Cu collisions collected during the Run-5. This dissertation presents another measurement of heavy-flavor muons in $p+p$ (Run-9) and $d+\text{Au}$ (Run-8) collisions at $\sqrt{s_{NN}} = 200$ GeV. Based on the measurements of heavy-flavor muons, the nuclear modification factor (R_{dA}) has been determined to quantify nuclear matter effects of the heavy-flavor muon production in $d+\text{Au}$ collisions.

In this research, a basic analysis methodology has been followed the recent method, using “*hadron cocktail*”, developed during the Run-5 data

analysis. Some of the detailed techniques have been improved during this research. In this section, brief introduction to overall analysis is described.

3.1.1 Source of tracks

The heavy-flavor muon, treated as “signal”, is extracted by eliminating background components from inclusive muon candidates. Inclusive muon candidates are reconstructed tracks reaching at the MuID Gap-4, which is the last plane in the MuID, and passing all track quality cuts. There are two main background sources in inclusive muons candidates. The first component is the muon from light hadron decay called “decay muon” which is dominant at $p_T < 3.0$ GeV/ c , and another component is “punch-through hadron” which is the hadron passing through all absorber in front of the MuID Gap-4. There are also other background sources like muons from quarkonia or low vector mesons as well

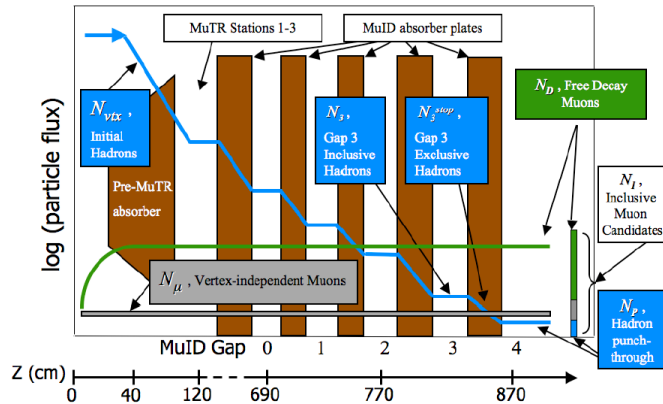


Figure 3.1: Schematic view of relative flux of tracks through the muon arm relative to the distance from the collision point.

as combinatorial backgrounds, but the fraction of these backgrounds to the signal is less than 5% after all background subtractions are proceeded. In this analysis, stopped hadron tracks reconstructed at MuID Gap-2 and Gap-3, which are not real background tracks of heavy-flavor muons at MuID Gap-4, are also considered to accurately estimate the hadron background using the hadron cocktail method. The detailed description about these track sources is following.

Prompt muon - muons from heavy-flavor decay

The prompt muon, which is treated as the signal in this analysis, refers to muons decaying from hadrons including heavy quarks (mostly c and b) produced *promptly* by hard scatterings in the hadron collisions. Due to very short decay lengths of the heavy-flavor hadrons (e.g. $c\tau(D) \sim 300\mu\text{m}$ and $c\tau(B) \sim 500\mu\text{m}$ [1]), these muons are produced very close to the collision vertex and mostly pass through the all MuID gaps. With the detector configuration during the data taking period for the data sets used in the research, muons from D and B mesons can not be separated.

Decay muon - muons from light hadron decay

Majority of produced particles from the hadron-hadron collisions are light hadrons (π , K , and p), and almost all of these hadrons are absorbed in the absorber in front of the Muon Tracker (MuTR) before decaying to muons. However, due to their huge initial production and the large branching ratios to muons ($\text{BR}(\pi^\pm \rightarrow \mu^\pm \nu_\mu) = 99.98\%$, $\text{BR}(K^\pm \rightarrow \mu^\pm \nu_\mu) = 66\%$ [1]), only tiny fraction of decaying hadrons before the absorber results in the important background source. These muons from the light hadron decay are dominant background tracks at low p_T region ($p_T < 3 \text{ GeV}/c$ for the data taken during Run-8 and

Run-9¹).

The probability of particle decay as a function of path length can be expressed as:

$$P(L) = 1 - e^{-\frac{L}{\gamma c \tau}}. \quad (3.1)$$

Since typical relativistic decay lengths of $\pi(\gamma c \tau(\pi_{p=2 \text{ GeV}/c}) \approx 100 \text{ m})$ and $K(\gamma c \tau(K_{p=2 \text{ GeV}/c}) \approx 50 \text{ m})$ are much longer than the distance from the collision point to the absorber ($\approx 40 \text{ cm}$), the equation (3.1) can be approximated by using the Taylor expansion like this:

$$P(L) \approx \frac{L}{\gamma c \tau}. \quad (3.2)$$

From this fact, the track z -vertex distribution normalized by the event z -vertex distribution shows a linear dependence on the z -vertex position.

Punch-through hadron

As described above, most of initially produced hadrons reach the absorber without decay. However, these hadrons suffer from the nuclear interaction with the $\sim 10\lambda$ of absorber and can not penetrate into the MuTr. Even though only a small fraction of hadrons survive from the interaction with the absorber, not a small number of hadrons pass through all MuID gaps, due to their huge initial flux, and are reconstructed as muon candidates called *punch-through hadrons*. This punch-through hadron is a dominant background source at high p_T ($p_T > 3 \text{ GeV}/c$ in the Run-8 and Run-9 data sets). Due to similar trajectory with prompt muon, punch-through hadron can be estimated

¹After installing additional absorber after Run-10, the p_T range where the decay muon is dominant up to higher p_T .

only by hadron simulation.

Stopped hadron

Tracks (hadrons and muons) passing through the MuID also suffer from interactions with absorber materials between the MuID gaps. As shown in 3.1, the flux of hadrons keeps decreasing as going into the deeper MuID gap. Although these stopped tracks before the last MuID gap (Gap-4) are not considered as the muon candidate, the stopped hadrons are used in this analysis to determine hadron background precisely by the hadron cocktail method. Figure 3.2 shows longitudinal momentum (p_z) distribution of stopped tracks at the MuID Gap-2 from the hadron cocktail simulation. Muons (red), stopped due to ionization energy loss, are located inside the peak near $p_z \approx 2 \text{ GeV}/c$, and hadrons (blue), stopped by the strong interaction with the absorber materials, are in the tail. Based on this figure, pure stopped hadrons can be selected with proper p_z cuts ($\sim 2.5 \text{ GeV}/c$) for the MuID Gap-2 and Gap-3 at both arms.

Other background sources

Besides the hadronic background (decay muon and punch-through hadron), there are other background sources in the muon candidates. These are muons from light vector mesons (ρ , ω , and ϕ) decay, muons from quarkonia (e.g. χ_c , J/ψ , ψ' , and Υ family) decay, and muons from Drell-Yan process. The muons from J/ψ are subtracted based on the previous PHENIX J/ψ measurement [37], and the contribution to the signal from the rest is less than 5% [53].

In addition, there are mis-reconstructed tracks which are accidentally reconstructed by taking random hits (so-called *combinatorial background*). Tracks decaying in the MuTR volume are also mis-reconstructed back-

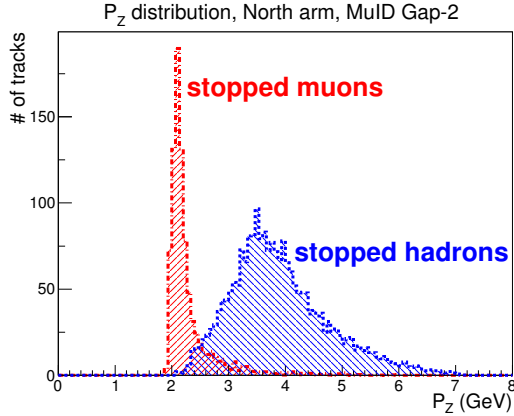


Figure 3.2: Longitudinal momentum distributions of the stopped tracks at MuID Gap-2 at north arm from hadron simulation.

ground and their contributions are large especially in high p_T region. Because the path of a track kinks inside the MuTR, its momentum can be mis-reconstructed as higher p_T than real p_T of the track.

3.1.2 Summary of analysis procedure

The main purpose of this analysis is to measure the invariant yield of heavy-flavor muons. This physical quantity can be obtained with the following formula:

$$\frac{d^2N^\mu}{2\pi p_T dp_T dy} = \frac{1}{2\pi p_T \Delta p_T \Delta y} \frac{N_I - N_C - N_F - N_{J/\psi}}{(N_{\text{evt}}/\epsilon_{BBC}) A \epsilon} \quad (3.3)$$

where Δp_T and Δy are the bin widths in p_T and y ; N_I is the number of inclusive muon candidates after filtering with the analysis cut; N_C is the number of decay and punch-through hadron background tracks determined using the hadron cocktail method; N_F is the estimated

number of fake tracks that pass the selection criteria; $N_{J/\psi}$ is the number of muons from J/ψ decay; N_{evt} is the number of sampled events; $A\epsilon$ is the detector acceptance and efficiency correction factor; and ϵ_{BBC} is the BBC bias correction factor for the trigger efficiency for MB events and events containing a heavy-flavor muon as well as the centrality determination. In order to determine the invariant yield of heavy-flavor muons, values of all symbols are calculated as following analysis procedure.

1. First of all, picoDSTs of the data sets ($d+\text{Au}$ in Run-8, $p+p$ in Run-9) are produced. Initial quality assurance (QA) is performed

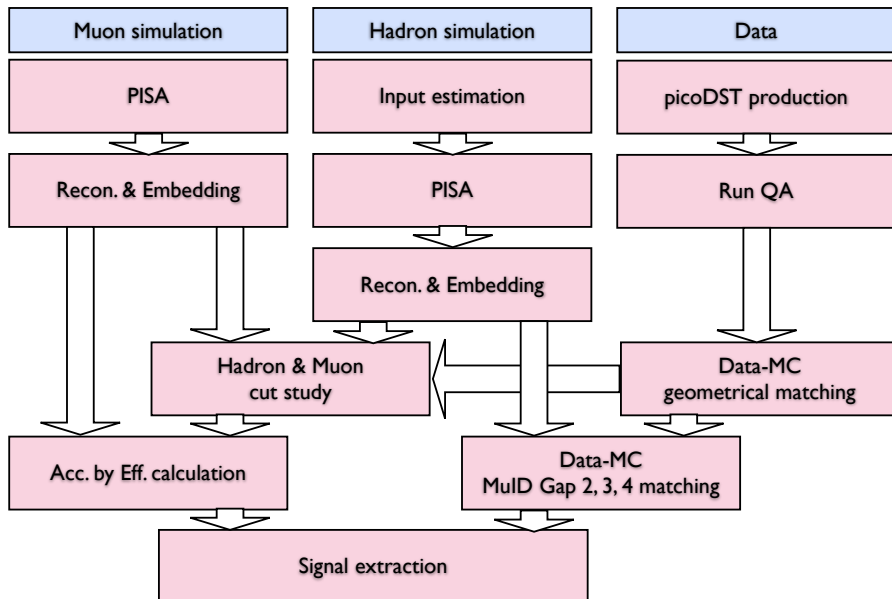


Figure 3.3: Analysis flow.

based on detector performance, mean event vertex position, and raw yield of muon candidates over the data taking period. After the QA, a list of good runs (i.e. number of analyzed events, N_{evt}) for a certain arm and a trigger is obtained.

2. Several versions (different modified nuclear cross section) of the hadron cocktail simulation, called *cocktail packages*, are performed. Based on these simulation using G-FLUKA or GHEISHA shower packages, track quality cuts for stopped hadron at the MuID Gap-2 and 3 are set. Additionally, geometrical cuts are also determined by comparing r and ϕ distributions at the MuTr between the data and the hadron cocktail simulation.
3. Pure single muons are simulated to determine track quality cuts for muon candidates (at the MuID Gap-4). Based on the track quality and geometrical cuts, the acceptance by efficiency ($A\epsilon$) can be calculated.
4. After filtering the data with the analysis cuts, good muon candidates (N_I) as well as stopped hadrons are obtained.
5. Input hadron spectra for hadron cocktail simulation are tuned by matching the hadron cocktail package to the data at the MuID Gap-2, 3, and 4. Then, hadronic background for a certain hadron cocktail package is determined.
6. In order to calculate the final hadronic background (N_C), several hadron cocktail packages are combined.
7. By subtracting the combined hadronic background from the muon candidate and applying the acceptance by efficiency correction,

invariant yield of heavy-flavor muons is obtained. However, this yield still includes muons from light vector meson, quarkonia, and Drell-Yan process.

8. At the moment of performing this analysis, only p_T spectra of J/ψ have been measured [37]. Muons from J/ψ ($N_{J/\psi}$) are estimated by decay simulation from fully corrected J/ψ p_T spectra. The contribution of the rest sources is negligible compared to the signal (< 5%).

3.1.3 Methodology for hadronic background estimation

As two main background sources, decay muon and punch-through hadron, are originated from light hadrons, these hadronic backgrounds can be predicted by simulation of mixture of hadrons called hadron cocktails. As shown in Fig. 3.3, the overall steps for the hadronic background estimation are summarized in the middle column. This hadron cocktail method had been well-developed during the preceding heavy-flavor muon research in PHENIX [69, 53], so basic methodology in this research have followed the previous method. Description about each step for the hadronic background estimation is following.

1. Initial hadron p_T spectra at forward and backward rapidity ($1.2 < |\eta| < 2.4$) in $p+p$ and $d+Au$ collisions are estimated based on fine-tuned event generators, PYTHIA and HIJING and measured p_T spectra at other rapidity ranges.

2. The full PHENIX detector simulation using GEANT [70] (PISA) is performed with estimated initial hadron p_T spectra. One of hadron shower codes (G-FLUKA and GHEISHA) with a modified nuclear interaction cross section is used for a certain set of simulation.
3. Simulated hadrons are reconstructed and embedded into the $p+p$ or $d+\text{Au}$ data to reproduce the detector inefficiency and track loss due to the multiplicity effect. On this stage, database files for MuTR configuration and MuID tube efficiency files are also implemented in order to reflect the realistic detector performance during the data taking period.
4. Then, the input p_T spectra of the hadron cocktail are tuned by matching the hadron cocktail simulation to the data at the MuID Gap-2, 3 and 4 separately. Stopped hadron yields are used for the matching at MuID Gap-2 and 3, and slopes of normalized z -vertex distribution are used for the matching at MuID Gap-4. These three tunes of the hadron cocktail and one optimal tune, matching at all MuID gaps simultaneously, are combined to determine the final hadronic background with the hadron cocktail.

3.2 Raw data analysis

3.2.1 Data sets

The data sets analyzed in this research are data from $p+p$ (RHIC Run-9) and $d+\text{Au}$ (RHIC Run-8) collisions at $\sqrt{s_{NN}} = 200$ GeV. Both

data sets were selected by level-1 muon triggers in coincidence with the minimum-bias (MB) trigger. As listed in Table 2.1, $\sim 80^{-1}\text{nb}^{-1}$ $d+\text{Au}$ and $\sim 16\text{ pb}^{-1}$ $p+p$ data are collected during the Run-8 and Run-9, respectively. The integrated luminosity of the second $d+\text{Au}$ run is almost 40 times larger than the first $d+\text{Au}$ run (RHIC Run-3).

Data files are basically stored in HPSS file storage as nanoDST format. This nanoDST files are produced by reconstruction of the raw data written as PHENIX Raw Data File Format (PRDFF). nanoDST files in HPSS storage can be accessed via the PHENIX official file access manager named *Analysis Train*. In order to reduce the size of data files and extract physics quantities of reconstructed tracks, picoDST are produced via the analysis train. The official module to make picoDST is located at the PHENIX code versioning system:

offline/package/MWGpico.

Based on this official module, slightly modified version of module is used to produce picoDST. For this version, some of useless variables are dropped and trigger variables are modified corresponding to the trigger setting during a certain run. The modified module is also located in the PHENIX CVS at:

offline/AnalysisTrain/Run_MWGpico_sngmuon.

Both data sets collected by using the MB and MuIDLL1 triggers are refined to picoDSTs. In order to reduce file size again for better accessibility to the data, a femtoDST set is produced by just filtering track information in the picoDST. The femtoDST is a non-official format,

and final size of data files for each $p+p$ and $d+\text{Au}$ collisions is around a few GB.

3.2.2 Initial quality assurance

Initial good runs are referred to good run lists used in dimuon analysis [71, 72]. The criteria of this good run selection is following.

- BBC status
- MuTr and MuID HV status
- MuTr and MuID LV status
- Zero field runs
- Runs containing no dimuon candidate

Additional QA are performed for the heavy-flavor muon analysis. At first, average event z -vertex per run is checked as shown in Fig. 3.4.

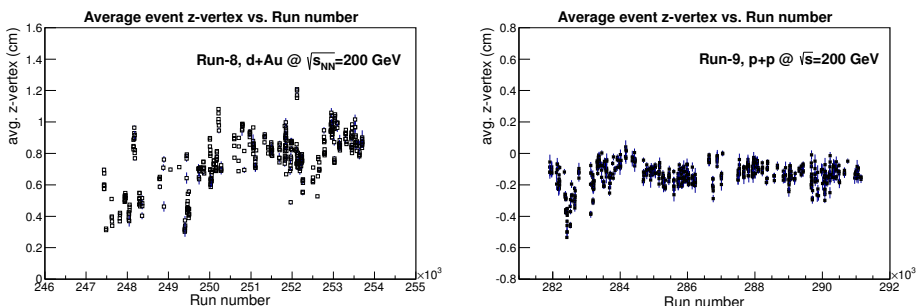


Figure 3.4: Average event z -vertex per run for Run-8 $d+\text{Au}$ (left) and Run-9 $p+p$ data.

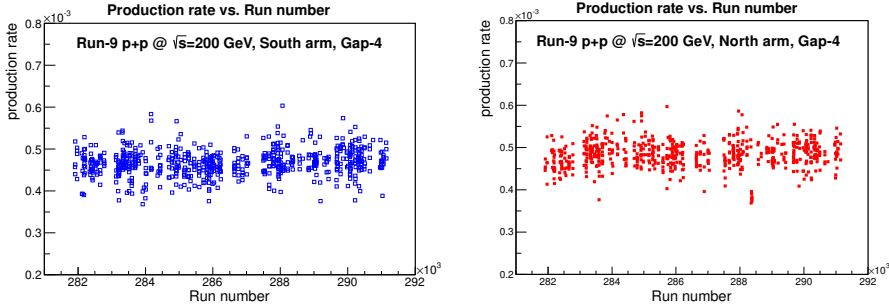


Figure 3.5: Production rate of the muon candidates at MuID Gap-4 for South (left) and North (right) muon arms in Run-9 $p+p$ data.

The run having average event z -vertex out of 3σ from the mean of the entire run is removed from the analyzed run list.

Secondly, raw track production yield at each MuID gap for each muon arm is checked. Figure 3.5 shows production rate of the muon candidates at the MuID Gap-4 for the both muon arms in the Run-9 $p+p$ data. Production rates at the MuID Gap-2 and Gap-3 are also checked, because the stopped hadron is also important component in this analysis. Based on the production rate per run, the run having production rate out of 3σ from the mean of the total runs is rejected. The raw production rate of dropped runs are possibly due to the bad detector HV problem as well as the DAQ status during these runs.

Finally, a QA for centrality is performed, and this is only for the $d+Au$ data set. This centrality QA is already done [73], and the status of QA for each run can be checked in the PHENIX database. As shown in Fig 3.6, the distribution of event fraction for each centrality class should be flat. Some runs out of the mean fractions are rejected.

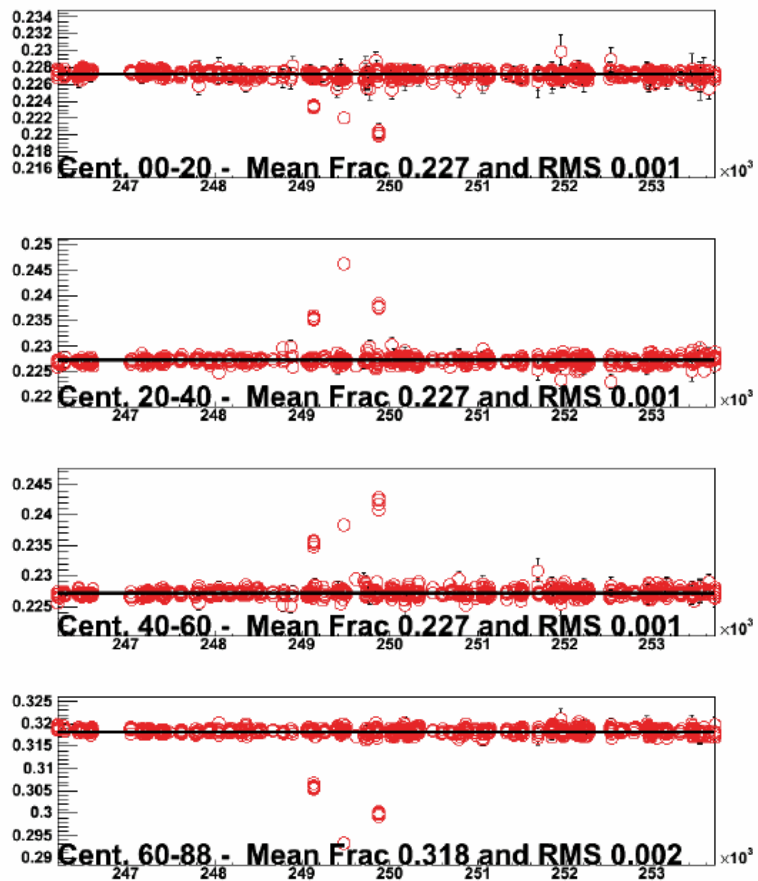


Figure 3.6: Fraction of events in four centrality classes of Run-8 $d+Au$ data set [73].

3.2.3 MB normalization

In order to normalize by the proper number of MB events, scale down factors of the MB and MuIDLL1 triggers are obtained from the PHENIX DAQ database. Figure 3.7 shows scale down factors for MuIDLL1D triggers at the South (left) and the North (right) muon arms during the Run-8 period. The scale down factors for the South arm are larger than those for the North arm, because the track multiplicity is larger at the South muon arm where the Au nucleus going direction. Fig-

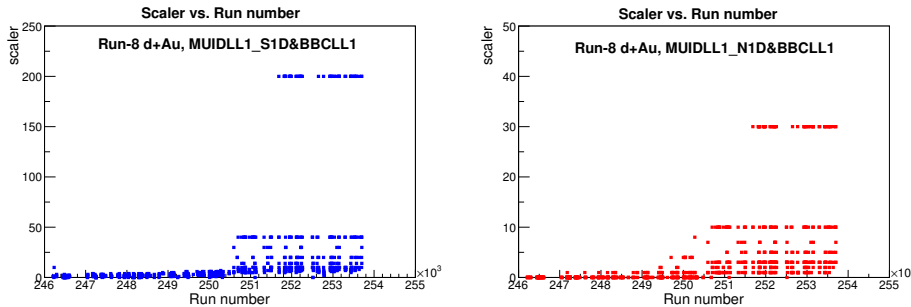


Figure 3.7: Run scaler for MuIDLL1D trigger for South (left) and North (right) arm during the period of Run-8.

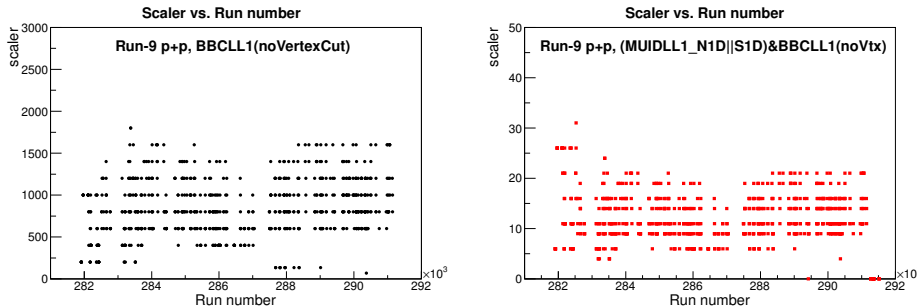


Figure 3.8: Run scaler for MB (left) and MuIDLL1D (right) triggers during the period of Run-9.

ure 3.8 shows scalers for the MB and MuIDLL1D triggers during the Run-9 period, and scale down factors for the MB trigger is a lot bigger than those of MuIDLL1D trigger.

Based on the scalers for the MB and a certain LL1 trigger, the correct number of the MB events for track samples in events collected by a certain LL1 trigger can be calculated as,

$$N^{sampled\ MB} = \sum_{run} \sum_{event} \frac{(S_{run}^{MB} + 1)}{(S_{run}^{LL1} + 1)} = \sum_{run} \left[N_{run}^{recorded\ MB} \frac{(S_{run}^{MB} + 1)}{(S_{run}^{LL1} + 1)} \right] \quad (3.4)$$

where $N_{run}^{recordedMB}$ is the number of analyzed MB events for a certain run, S_{run}^{MB} and S_{run}^{LL1} are scale down factor for the MB and LL1 triggers for a certain run, repectively. Table 3.1 shows sampled MB events and corresponding luminosity within ± 25 cm z -vertex window for each

Table 3.1: Sampled MB events for Run-8 d +Au and Run-9 $p+p$ data set.

| Run-8 d +Au | | |
|---------------|-----------------------|---------------------------------|
| Arm | Sampled MB events | Luminosity (nb^{-1}) |
| South (D) | 9.27×10^{10} | 46.8 nb^{-1} |
| North (D) | 9.75×10^{10} | 49.3 nb^{-1} |
| South (H) | 8.43×10^{10} | 42.6 nb^{-1} |
| North (H) | 9.22×10^{10} | 46.6 nb^{-1} |
| Run-9 $p+p$ | | |
| Arm | Sampled MB events | Luminosity (nb^{-1}) |
| South (D) | 2.28×10^{11} | 9.9 pb^{-1} |
| North (D) | 2.28×10^{11} | 9.9 pb^{-1} |
| South (H) | 2.28×10^{11} | 9.9 pb^{-1} |
| North (H) | 2.28×10^{11} | 9.9 pb^{-1} |

muon arms and each MuIDLL1 trigger (1D and 1H) of the Run-8 $d+Au$ and the Run-9 $p+p$ data sets.

3.2.4 Analysis variables

Each reconstructed track from data and simulation in the picoDST has the same set of analysis variables. These analysis variables contain information of tracks such as kinematics and detector responses. With these variables, initial track selection is performed in order to reject background tracks. The following list introduces mainly used analysis variables for the heavy-flavor muon analysis.

1. **z_{BBC}** - vertex position of the collision event along the beam direction measured by the BBC detector.
2. **DDG0** - The angle between the projected track of MuTr and the road of MuID at the MuID Gap-0 as illustrated in Fig. 3.9.

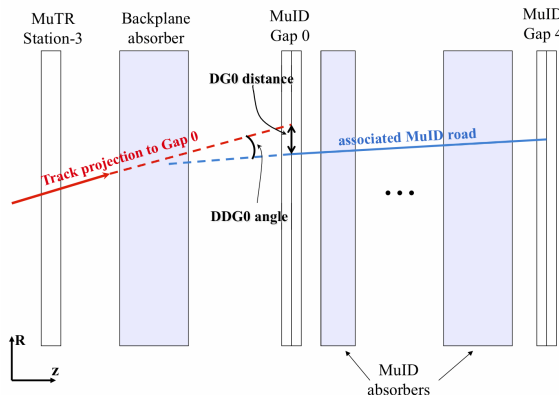


Figure 3.9: Schematic view of analysis variables, DG0 and DDG0.

3. **DG0** - The distance between the projected track of MuTr and the road of MuID at the MuID Gap-0 as illustrated in Fig. 3.9.
4. **R_{ref}** - The radial offset at $z = 0$ of the projected track from MuID road. Based on offsets at $z = 0$ (Δx and Δy), obtained by linear extrapolating with the slope of MuID road and the hit at MuID Gap-0, R_{ref} is determined as $\sqrt{(\Delta x)^2 + (\Delta y)^2}$ as illustrated in Fig. 3.10.
5. **Road slope** - The slope of the MuID road. This variable is effective for removing tracks into the square hole in the absorber and MuID planes. The slope is calculated as $\sqrt{(\frac{dx}{dz})^2 + (\frac{dy}{dz})^2}$.
6. **δz** - The difference between the event vertex provided by the BBC (z_{BBC}) and the estimated vertex determined by the muon reconstruction code (z_{refit}).

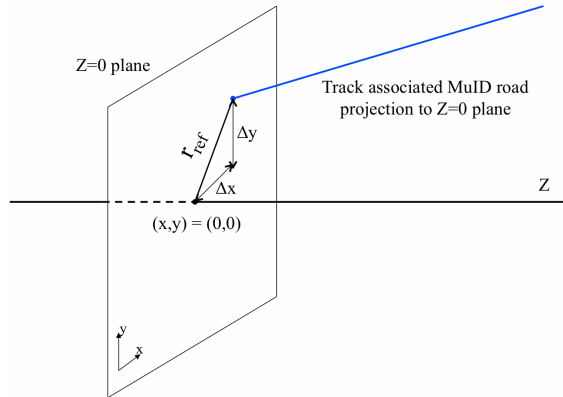


Figure 3.10: Schematic view of analysis variable, R_{ref} .

7. $p\delta\theta$ - This variable is determined as,

$$p\delta\theta = \frac{p_{vtx} + p_{sta1}}{2} \cdot \cos^{-1} \left(\frac{\vec{p}_{vtx} \cdot \vec{p}_{sta1}}{|\vec{p}_{vtx}| \cdot |\vec{p}_{sta1}|} \right)$$

where \vec{p}_{vtx} is the momentum vector at the event vertex, and \vec{p}_{sta1} is the momentum vector at the MuTr station 1. This variable means the amount of deflection of the track due to multiple scattering in the absorber in front of the MuTr. This variable is very effective to discriminate mis-reconstructed tracks decaying inside the MuTr volume, because these tracks are mostly reconstructed with higher p_T and larger angle bent.

8. χ^2_{vtx}/ndf - χ^2/ndf calculated between the vertex position from linear fitting of associated track and the real event vertex. This cut was used only in the dimuon analysis before this research. In the heavy-flavor muon analysis, this cut is really effective to reject combinatoric background. The details is described in [74].

3.2.5 Track quality cuts

Basic track selection criteria is following.

1. $1.4 < |\eta| < 2.0$

2. $-25 \text{ cm} < z_{BBC} < 25 \text{ cm}$

3. $1.0 < p_T < 7.0$

4. $N_{MuTR \text{ hits}} > 12$

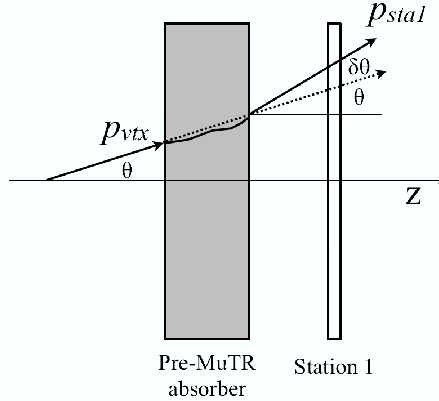


Figure 3.11: Schematic view of analysis variable, $p\delta\theta$.

5. $p_z > 2.8$ for the stopped hadrons at the MuID Gap-2 and 3 (arm and gap dependent)
6. centrality classes for the d +Au data (MB, 0–20%, 20–40%, 40–60%, 60–88%)

For the muon candidate tracks

The inclusive tracks at the MuID Gap-4 filtered with the basic track selection criteria are refined again to eliminate unphysical tracks coming from poor reconstruction or strong interaction with material. Applying well defined analysis cuts contributes to increase the signal-to-background ratio. Analysis cuts for the muon candidate tracks are determined based on the simulation with pure muons. Simulated muons are embedded into the real p + p and d +Au data to reproduce the detector occupancy effect due to the track multiplicity.

Figure 3.12 is example distributions of two cut variables, DG0 (top) and $p\delta\theta$ (bottom), at the MuID Gap-4 for the data and the simulated

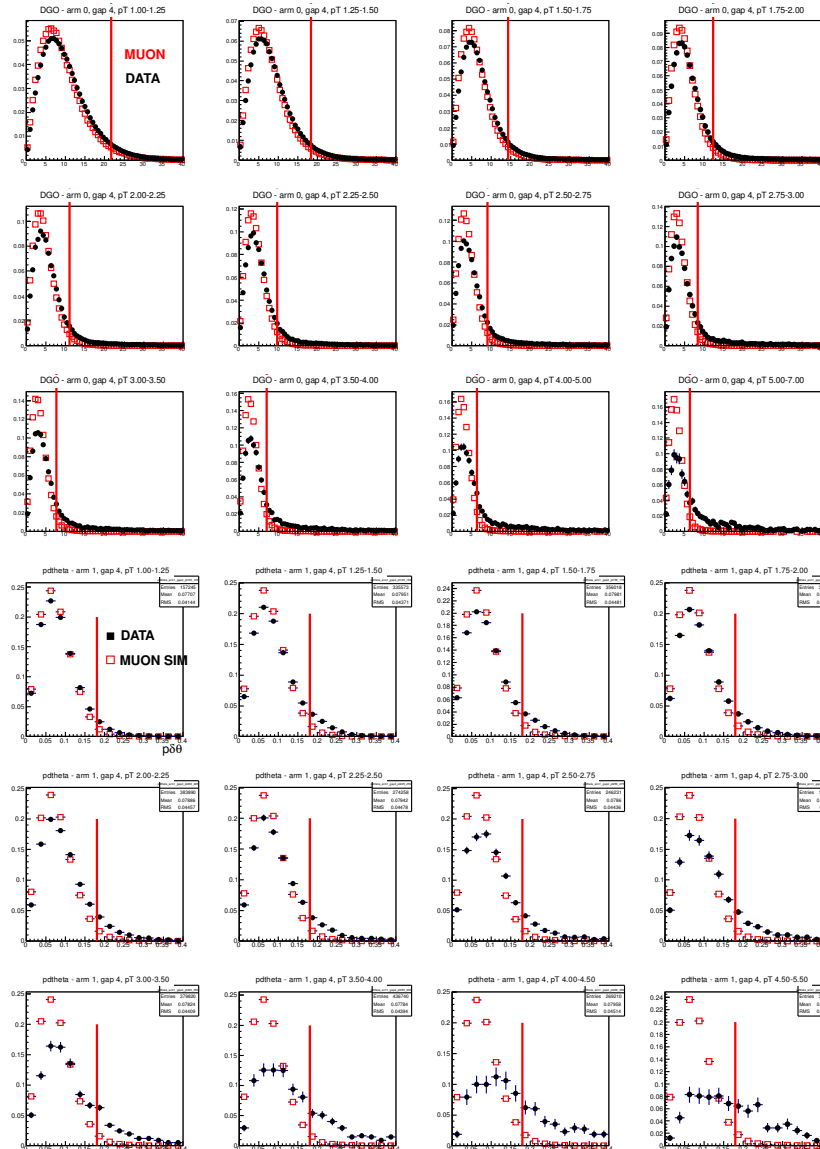


Figure 3.12: DG0 (top) and $p\delta\theta$ (bottom) distributions at MuID Gap 4 of the data (filled black) and muons simulation (open circle). Each small panel for a variable corresponds to a certain p_T bin, and the red lines refer to the value containing 96% of simulated muons.

Table 3.2: The track selection criteria for the inclusive muon candidates. Values in brackets are cut values for South muon arm.

| Cut variable | Description |
|-----------------------|--|
| $\text{MuTr } \chi^2$ | $\chi^2_{\text{MuTr}} < 10(8)$ |
| Road slope | Road slope > 0.21 |
| $p\delta\theta$ | $p\delta\theta < 0.18 \text{ GeV} \cdot \text{rad}/c$ |
| δz | $\delta z < 2 \text{ cm}$ |
| R_{ref} | $R_{ref} < 77(77) \text{ cm}$, p_T & centrality dependent |
| DG0 | $\text{DG0} < 8.3(21.6) \text{ cm}$, p_T & centrality dependent |
| DDG0 | $\text{DDG0} < 5.6(6.2) \text{ degree}$, p_T & centrality dependent |
| χ^2_{vtx}/ndf | $\chi^2_{vtx}/ndf < 4.0(4.1)$, p_T & centrality dependent |

muons. Each small panel indicates each p_T bin, and the red lines in small panels are the determined cut values containing 96% of simulated muons. As shown in the figure, the muon simulation well reproduces the distribution of cut variables in low p_T . However, some discrepancies, depending on cut variables and p_T bins, are seen in high p_T . These differences between the simulation and the data are probably due to the combinatorial background as well as non-muon tracks (e.g. punch-through hadrons) for which relative fraction to muons becomes larger as p_T increases. The previous study showed that the distributions from muon simulation and muons from J/ψ in the data are in a good agreement [49]. The values of analysis cuts for the muon candidate tracks are listed in Table 3.2, and some cuts depend on the p_T and centrality.

In addition, a near-side z cut is applied for the three lowest p_T bins in order to improve the signal-to-background ratio. In case of the first three low p_T bins, almost 90% of background tracks are decay muons.

The number of decay muons increases as the flight length becomes longer. Therefore, this near-side z cut, rejecting the far-side of z -vertex, can contribute extensively to enhance the signal-to-background ratio. Furthermore, there are enough statistics in the low p_T region and accepting only half length of z -vertex ($0 \text{ cm} < z < 25 \text{ cm}$ for the North arm) does not cause lack of statistics.

For the stopped hadron tracks

Contrary to the analysis cuts for the muon candidates, analysis cuts for the stopped hadrons are determined separately for the data and two hadron shower packages in GEANT, G-FLUKA, and GHEISHA. Figure 3.13 shows DDG0 and R_{ref} distributions of the data, G-FLUKA and GHEISHA in each p_T bin. Even though two hadron shower codes seems to qualitatively reproduce the distributions of data, the values of a certain cut variable containing 96% of hadrons are slightly different. In order to avoid a bias from applying same values of cuts, analysis cuts are determined separately for the data and the simulation with G-FLUKA and GHEISHA to accept 96% of hadrons correspondingly. In Table 3.3, analysis cuts for the stopped hadrons at the MuID Gap-3 in the data are listed.

3.2.6 Geometrical acceptance cuts

One of known issues on acceptance by efficiency correction is run-to-run variation due to selecting only one reference run. During the data taking period, the condition of detectors is not uniform. For example, some HV problems on the MuTr or the MuID causes inefficient re-

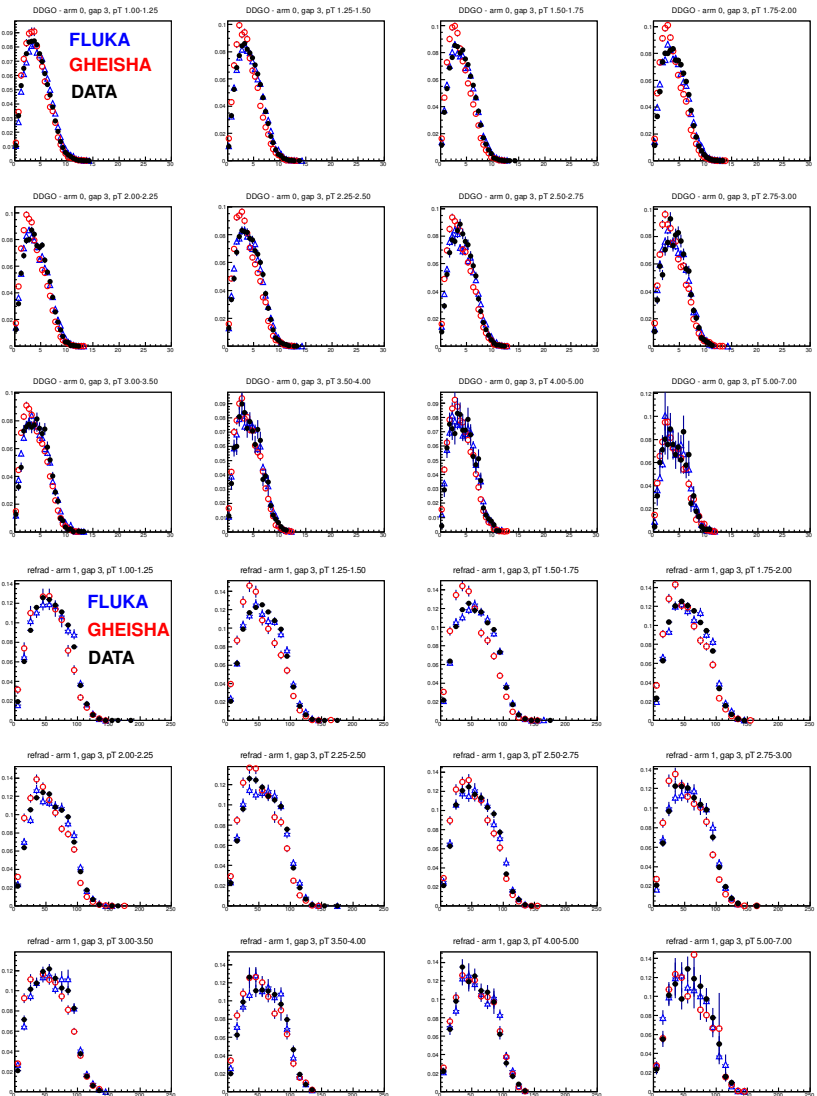


Figure 3.13: DDG0 (top) and R_{ref} (bottom) distributions at MuID Gap-3 of the data (black filled circle), G-FLUKA (blue open triangle), and GHEISHA (red open circle) simulation. Each small panel for a variable corresponds to a certain p_T bin.

gions during some part of runs. Therefore, there are mismatched areas between the hadron simulation and the data. Since exact matching between the simulation and the data is a critical point in this analysis, proper geometrical cuts are needed to improve the matching.

During the Run-8 d +Au collisions, polarity of the magnetic field was changed. As charged particles move reversely at two magnetic field configurations, the same inefficient detector area may affect differently in the opposite magnetic field. In order to combine the data of two magnetic field configurations and use full statistics, this geometrical restriction should remove the disagreement in the data and the simulation between the two magnetic field polarity. More details would be discussed in the following section.

Another issue during the Run-9 is the installation of a prototype absorber at the South muon arm. This additional absorber was installed

Table 3.3: The track selection criteria for the stopped hadrons at MuID Gap-3, respectively. Values in brackets are cut values for South muon arm. Analysis cuts for G-FLUKA and GHEISHA simulation and for the stopped hadrons at MuID Gap-2 are slight different from the values here.

| Cut variable | Description |
|--------------------|---|
| MuTr χ^2 | $\chi^2_{MuTr} < 10(8)$ |
| Road slope | Road slope > 0.21 |
| $p\delta\theta$ | $p\delta\theta < 0.21 \text{ GeV} \cdot \text{rad}/c$ |
| δz | $\delta z < 2 \text{ cm}$ |
| R_{ref} | $R_{ref} < 105(103) \text{ cm}$, p_T & centrality dependent |
| DG0 | $DG0 < 14.6(32.6) \text{ cm}$, p_T & centrality dependent |
| DDG0 | $DDG0 < 8.2(8.2) \text{ degree}$, p_T & centrality dependent |
| χ^2_{vtx}/ndf | $\chi^2_{vtx}/ndf < 8.2(8.2)$, p_T & centrality dependent |

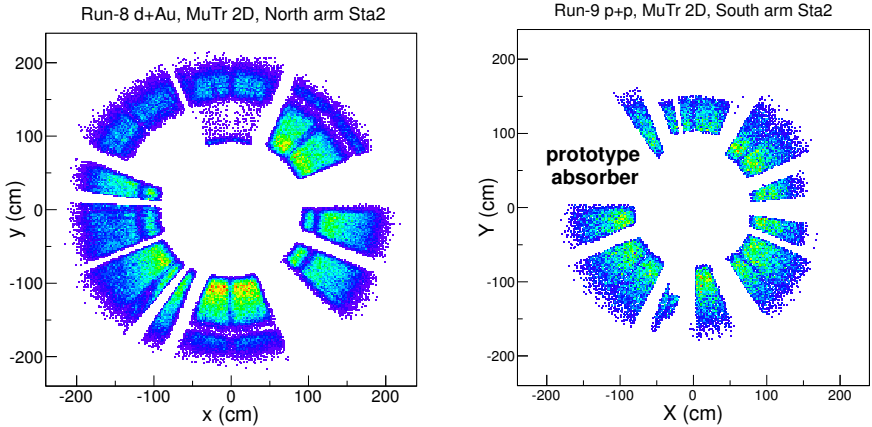


Figure 3.14: MuTr 2D hit histograms at MuTr Station 2 in North arm of Run-8 $d+Au$ (left) and in South arm of Run-9 $p+p$ (right).

to test the effect on background rejection for W analysis. Since the nuclear cross section of the absorber material is modified for the simulation, the acceptance corresponding to the additional absorber should be cut out to avoid over- or under-correct hadron interactions with the additional absorber.

The geometrical cuts are determined based on ϕ and r distributions at the MuTr stations. Figure 3.14 shows $x - y$ hit distributions at the MuTr Station-2 after applying geometrical cuts. As shown in the right panel in Fig. 3.14, the region of the additional absorber during the Run-9 is removed. Figure 3.15 shows ϕ (top) and r (bottom) distributions of the data, G-FLUKA, and GHEISHA simulations in the North muon arm, and each small panel is for one octant. Both ϕ and r distributions show good agreements between the data and the simulations.

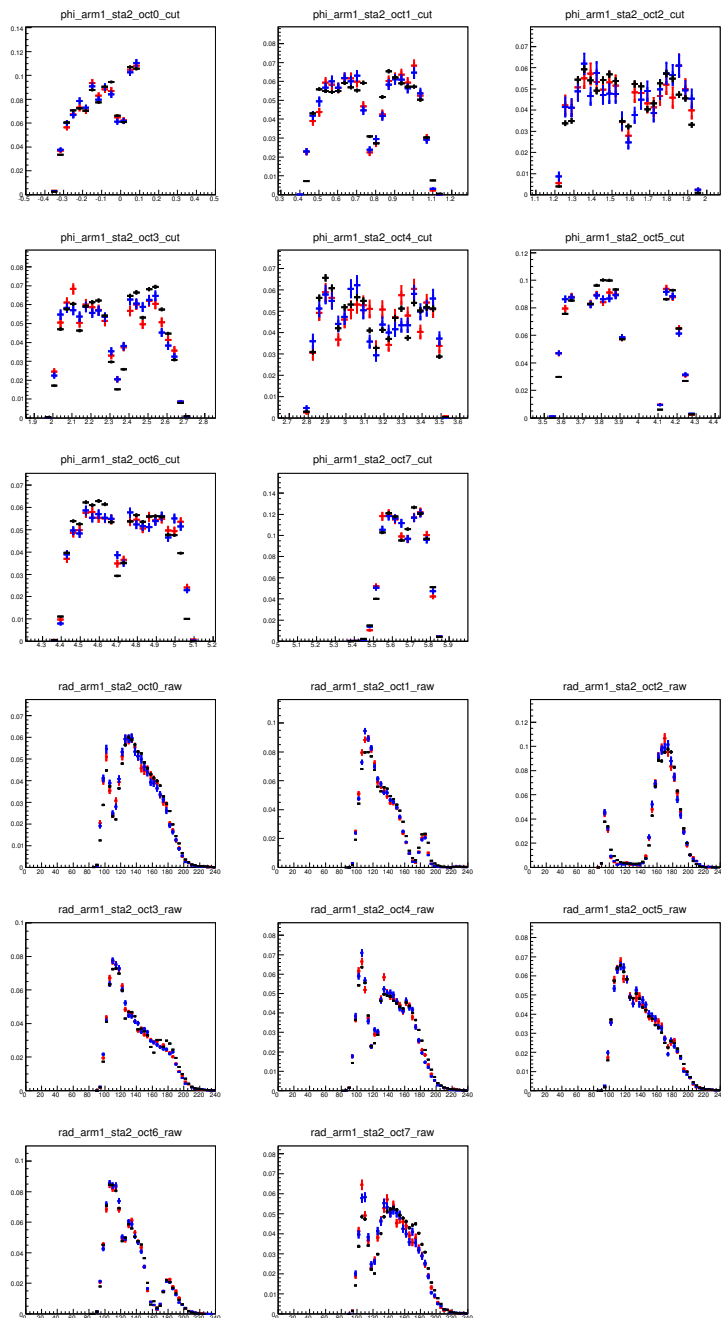


Figure 3.15: Comparison of ϕ and r distributions between the data (black) and the hadron simulations, G-FLUKA (blue) and GHEISHA (red).

3.2.7 Magnetic field configuration

As mentioned briefly in the previous section, the magnetic field configuration was changed from normal field to reverse field in the middle of the data taking period of Run-8 d+Au collisions. Negatively charged tracks, which are analyzed in this research, move oppositely in the two different magnetic field configuration. Furthermore, geometric cuts determined based on a single magnetic field configuration may cause additional track loss or disagreement of acceptance between the two magnetic fields. Geometrical distributions of the data and the combined simulation (half of the normal field and half of the reversed field) and raw yield at each MuID gap are compared after applying proper geometrical cuts. In order to perform stable background estimation over the entire analyzed p_T range, the combined data set should be used instead of using the data in normal and reversed field separately. This is the reason for confirming the agreement of raw yield in the two magnetic field configurations.

Figure 3.16 shows raw track yield per run after applying the geometrical cuts, top (bottom) panel is for the South (North) muon arm. The run number 250593 on the vertical line is the first reversed field run. The left (right) part of the vertical line is the normal (reversed) field runs. Raw track yield between two mangetic configurations show good agreements both muon arms. Figure 3.17 shows raw p_T spectra at the MuID Gap-2, 3, and 4 between the two field configurations. Top panel is for the hadron simulation and bottom panel is for the data. In case of both the data and simulation, p_T sepctra of the two field configurations are consistent at the all MuID gaps.

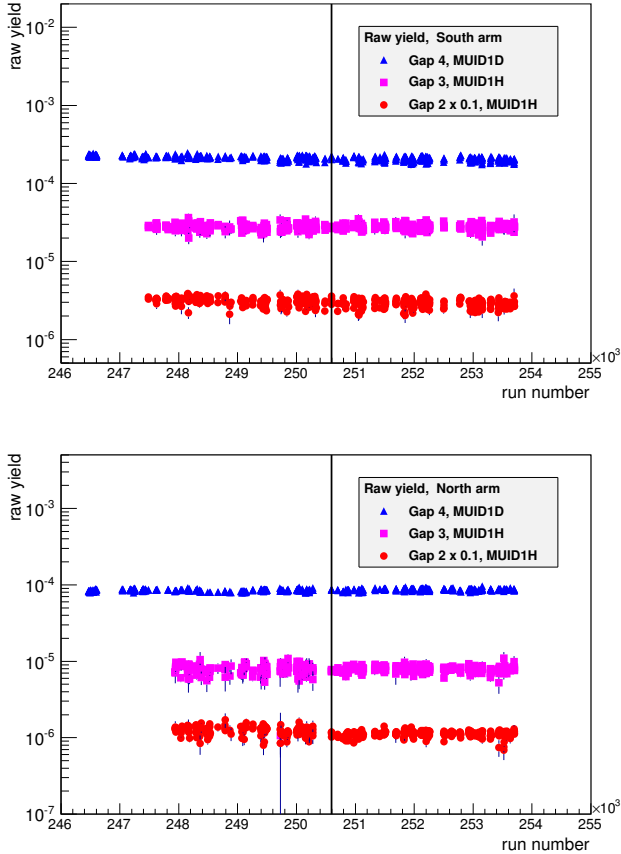


Figure 3.16: Comparison of raw track yield per run comparision at MuID Gap-2, 3 and 4 after applying proper geometrical cuts at both South (top) and North (bottom) muon arms. The left (right) part of the vertical line is the normal (reversed) field run.

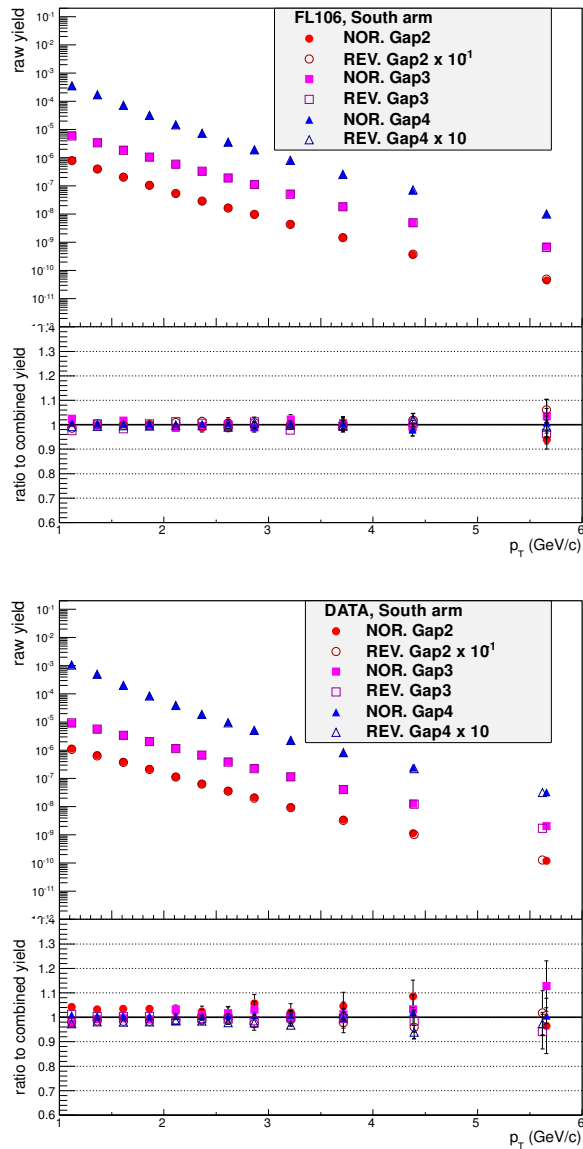


Figure 3.17: Raw p_T spectra comparisions of the simulation (top) and the data (bottom) at all MuID gaps after applying geometrical cuts. Filled points refer to the normal field, and open points refer to the reversed field.

3.3 Acceptance by efficiency study

The acceptance by efficiency correction considers following things:

- restricted acceptance
- analysis cut efficiency
- track reconstruction efficiency
- trigger efficiency

In this correction, only correction factors for single muons (heavy-flavor muons) are needed. This is because background estimation and subtraction are performed with uncorrected simulation and data. Otherwise, correction factor for decay muons, punch-through hadrons, and stopped hadrons should be considered. The precise acceptance by efficiency calculations for these tracks is more complicated than the case of pure single muons.

Calculation of the acceptance by efficiency is performed based on the full PHENIX detector simulation, reconstruction, and embedding to real data. Pure single muons are generated based on realistic p_T and η distributions for a given p_T bin and thrown to the muon arm acceptance. In order to consider bleeding over contributions of target p_T and η bins, the generated p_T range is wider than the target p_T bin range. This bleeding over effect is due to the momentum resolution of MuTr ($\sigma_p/p \approx 5\%$), so that some muons which generated p_T are lower or higher than the range of interest are possibly reconstructed within the target p_T range. The overall steps for the acceptance by efficiency calculation are following.

1. generating pure single muons based on the realistic p_T , η distributions, and z -vertex positions extracted from the real data used for embedding to match z -vertex positions between the simulated muon and the embedded event.
2. full PHENIX detector simulation and reconstruction to DST
3. embedding to the real $p+p$ and $d+\text{Au}$ data and producing pi-coDST
4. applying the offline trigger emulator used for the data
5. filtering reconstructed tracks with the exactly same analysis cuts applied for the data
6. calculating acceptance by efficiency by making a ratio between

Table 3.4: Acctepance by efficiency correction factors for Run-9 $p+p$ data depending on p_T range.

| p_T bin | Acc. \times Eff. South | Acc. \times Eff. North | Generated p_T range |
|-------------|--------------------------|--------------------------|-----------------------|
| 1.00 - 1.25 | 0.201 | 0.179 | 0.8 - 9.0 |
| 1.25 - 1.50 | 0.293 | 0.310 | 1.1 - 9.0 |
| 1.50 - 1.75 | 0.334 | 0.364 | 1.2 - 9.0 |
| 1.75 - 2.00 | 0.355 | 0.394 | 1.2 - 9.0 |
| 2.00 - 2.25 | 0.359 | 0.407 | 1.6 - 9.0 |
| 2.25 - 2.50 | 0.370 | 0.429 | 1.6 - 9.0 |
| 2.50 - 2.75 | 0.361 | 0.411 | 2.0 - 9.0 |
| 2.75 - 3.00 | 0.365 | 0.420 | 2.0 - 9.0 |
| 3.00 - 3.50 | 0.365 | 0.424 | 2.5 - 9.0 |
| 3.50 - 4.00 | 0.352 | 0.418 | 3.0 - 9.0 |
| 4.00 - 5.00 | 0.367 | 0.426 | 3.5 - 9.0 |
| 5.00 - 7.00 | 0.386 | 0.439 | 4.5 - 9.0 |

numbers of generated muons and reconstructed muons for a given p_T bin

The calculated acceptance by efficiency values for the Run-9 $p+p$ are listed in Table 3.4. Generated p_T range for each p_T bin is also contained in the table. The correction numbers for the South and North arms are slightly different, and this is mostly due to the different geometrical cuts between the two muon arms. Figure 3.18 shows the acceptance by efficiency correction factors as a function p_T for the different $d+\text{Au}$ centrality classes. The left plot is for the South arm, and the right plot is for the North arm. Only small track multiplicity (detector occupancy) effect is seen at the South arm (Au-direction) where relatively more particles are produced than the North side (d -direction). Figure 3.19 shows z -vertex dependence for each p_T bin. In the entire p_T bins at both South (top) and North (bottom) arm, the acceptance by efficiency are almost independent on the z -vertex position.

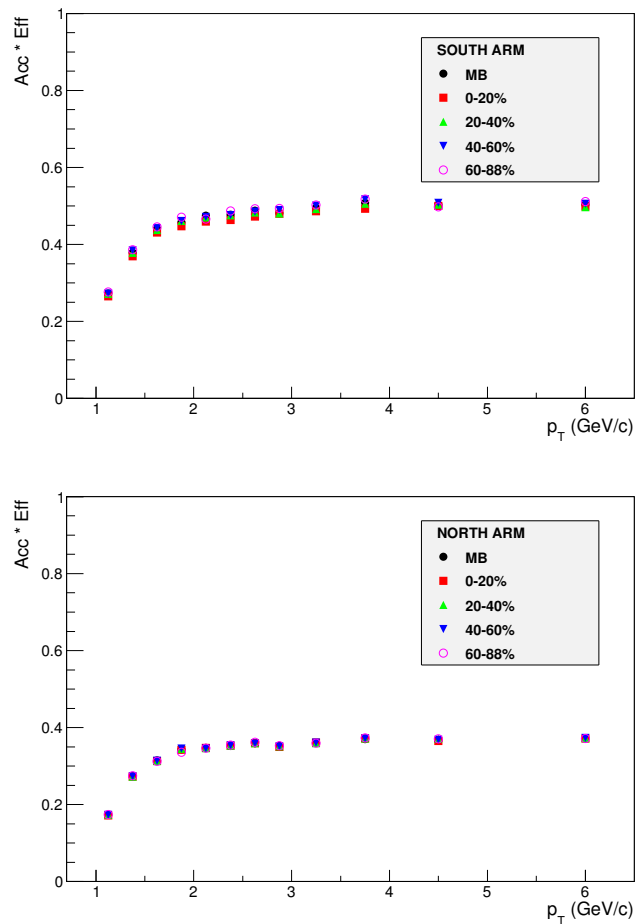


Figure 3.18: Acceptance by efficiency for different centrality classes in Run-8 $d+Au$ at South (left) and North (right) arm.

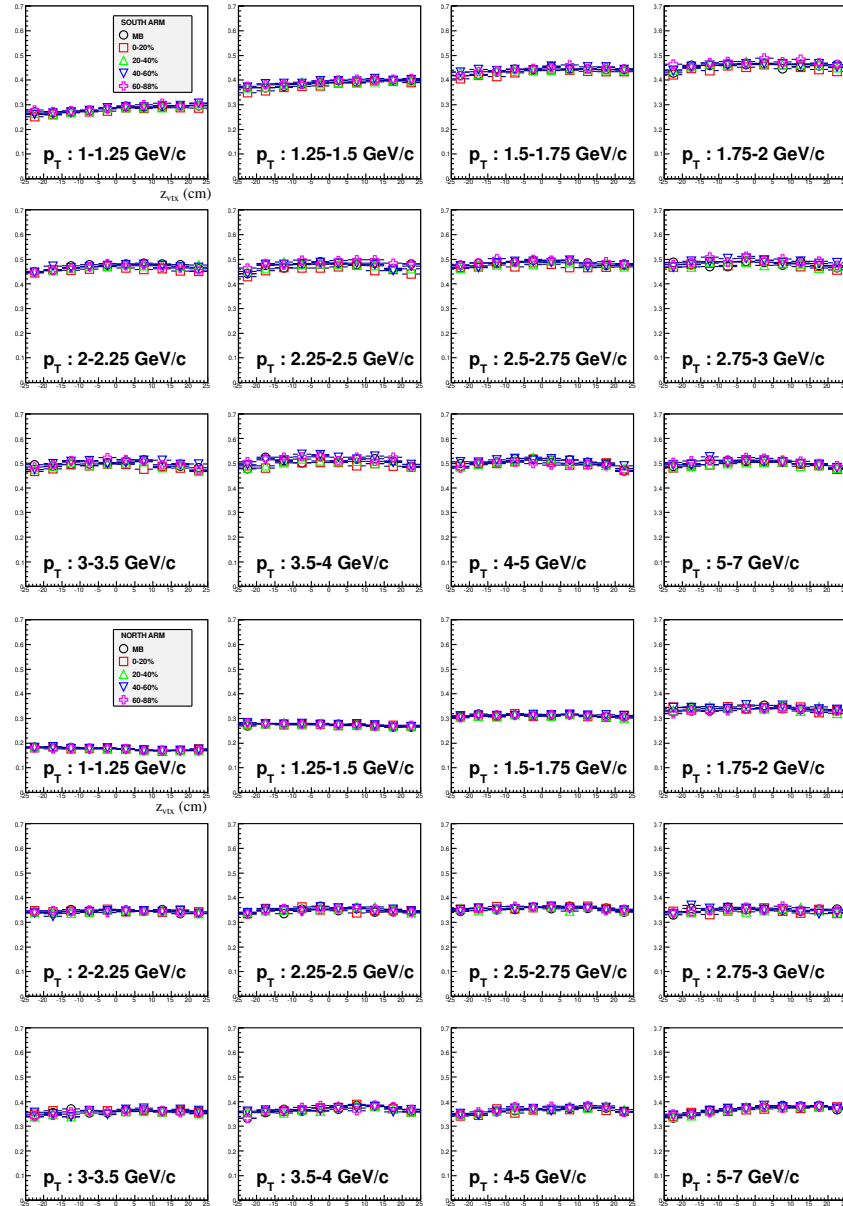


Figure 3.19: z -vertex dependent acceptance by efficiency for different centrality classes in Run-8 $d+Au$ at South (top) and North (bottom) arm. Each small panel refers to a certain p_T bin.

3.4 Background estimation

The basic background estimation method used in this analysis have been established by the previous heavy-flavor muon analysis [69, 53]. The hadron cocktail method, which is the most important part of the background estimation, estimates hadronic backgrounds (decay muons and punch-through hadrons) by simulating admixture of light hadrons (π , K , and p). Since dominant background sources are the decay muon and the punch-through hadron as discussed in Sec. 3.1.2, the simulation with the reasonable composition of light hadrons can reproduce the track flux at the all MuID gaps.

Unfortunately, there are two known issues in the heavy-flavor muon analysis at forward rapidity.

- Lack of identified hadron measurement at the PHENIX muon arm rapidity window
- Incongruity of both available hadron shower codes in the PHENIX simulation framework, G-FLUKA and GHEISHA

In order to overcome these issues, following techniques have been approached.

- Tuning input hadron p_T spectra by matching the hadron cocktail simulation to the data at the MuID Gap-2, 3 and 4
- Modifying the nuclear interaction cross section in two hadron shower codes in order to reproduce the particle flux in the data.

Details on the hadron cocktail method and the development in this research are dicussed in the following sections.

3.4.1 Estimation of cocktail input

In the previous heavy-flavor muon analysis for the Run-5 $p+p$ and Cu+Cu data sets [53], NLO pQCD calculation of π and measured K/π ratio at mid-rapidity were used. However, not only there are more limited hadron measurements, but also no theoretical prediction exists for $d+\text{Au}$ collisions. Therefore, a different method using event generators was approached in this research. At first, analysis of the Run-9 $p+p$ data set, using PYTHIA [75] for the initial hadron estimation, was performed in order to confirm the estimation method. Then, this estimation method extended to the analysis of the $d+\text{Au}$ data set by using HIJING [76]. Detailed steps for the input hadron estimation with event generators are described below.

1. Searching for the best parameter sets of PYTHIA(HIJING) event generator which could reasonably reproduce the measured data (light hadrons) at mid- (PHENIX, STAR) and forward- (BRHAMS) rapidity ranges
2. Simulating enough number of MB events to extract smooth curves for all light hadrons in pseudo-rapidity slices ($\Delta\eta = 0.2$)
3. Making p_T spectra of light hadrons in η slices
4. Calculating a correction function at $< y > = 0$ as ratios between the measured data and the PYTHIA(HIJING) simulation for each hadron
5. Adjusting p_T spectra in all η slices from PYTHIA(HIJING) with the correction function

6. Applying a p_T^3 weight to each p_T spectra to simulate enough amount of high p_T hadrons (simulated hadrons are re-weighted with a $p_T^{1/3}$ before matching to the data)

Table 3.5: PYTHIA v6.424 parameter set for the input hadron spectra estimation

| Parameter | Value | Description |
|-----------|-------|---|
| MSEL | 2 | turn on all QCD process for MB events |
| MSTP(5) | 100 | TuneA parameter set |
| MSTP(33) | 1 | Use K-factor |
| MSTP(52) | 2 | Use external PDF library |
| PARP(31) | 2.5 | K-factor for hard parton-parton process |
| MSTP(51) | 10042 | Use CTEQ6L PDF library |

The parameter set used for PYTHIA is listed in Table 3.5, and default parameter set was used for HIJING. The original p_T spectra of hadrons directly from PYTHIA(HIJING) are not perfectly matched to the measured data at mid-rapidity, especially at low p_T . In order to improve p_T curves and K/π ratios, p_T spectra from the event generators are ad-

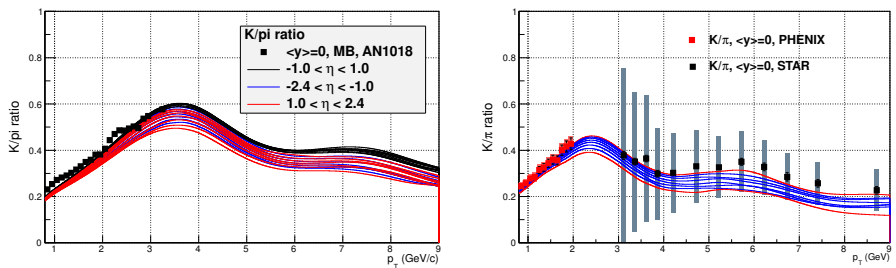


Figure 3.20: Comparison of K/π ratios between the hadron cocktail and the data in $d+Au$ (left) and $p+p$ (right) collisions.

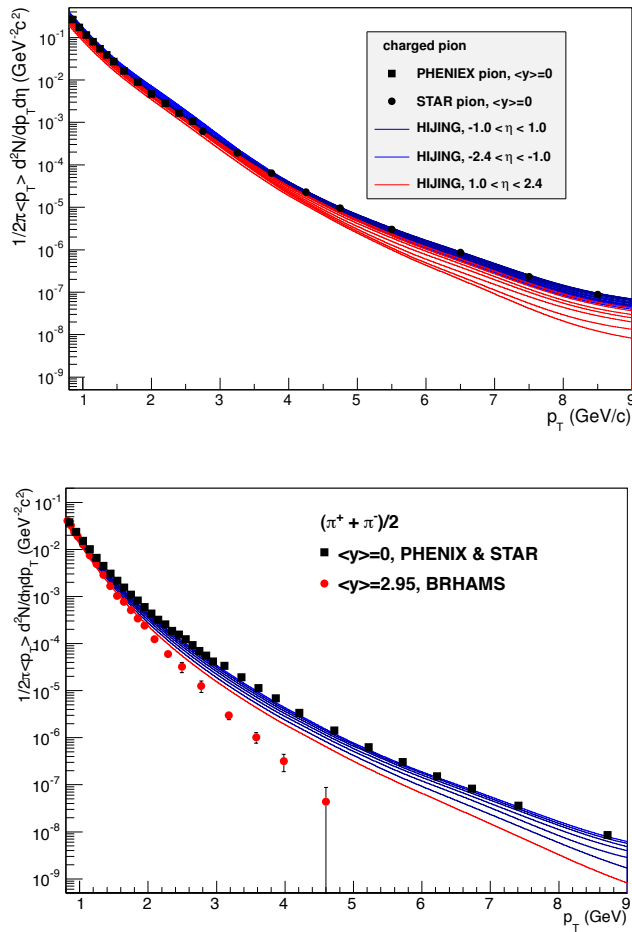


Figure 3.21: Comparison of p_T spectra for π between the hadron cocktail and the data in $d+Au$ (top) and $p+p$ (bottom) collisions.

justed by ratios of the data to PYTHIA(HIJING). After this adjustment, matching of p_T spectra between the data and the event generators is improved as shown in Fig. 3.20 and 3.21.

It is very hard to simulate enough number of hadrons up to high p_T with normal exponential p_T spectra, so final input p_T spectra for the hadron cocktail simulation are slightly modified from the initially estimated p_T spectra. Because enough high p_T hadrons can not be generated just with the normal p_T spectra. The p_T spectra obtained from the steps above are weighted by p_T^3 as,

$$\frac{\Delta N_{input}}{\Delta p_T \Delta \eta} \approx A_{norm} \frac{d^2 N}{dp_T d\eta} \cdot \langle p_T \rangle \cdot p_T^3. \quad (3.5)$$

These weighted input spectra help to reduce simulation time for the enough statistics upto high p_T . The hadron simulation with the p_T^3 weighted spectra are re-weighted correctly before matching to the data. There is a reason to use the p_T^3 weighted p_T spectra instead of using flat p_T distribution to generate enough number of high p_T hadrons. Previous muon analysis has suffered from particular background tracks which are hadrons decaying in the MuTr volume. As previously mention in the introduction to $p\delta\theta$ cut variable, these muons decayed inside the MuTr are generally from low p_T and reconstructed in higher p_T . In order to simulate enough number of these background tracks, the original exponential shape of p_T spectra is not significantly modified.

3.4.2 Hadron cocktail simulation with modified nuclear cross section

Hadron generation

Single hadron simulation is performed based on the estimated input p_T spectra discussed in the previous section. Properties of the hadron generation are listed below.

1. particles : π^\pm , K^\pm , K_S^0 , K_L^0 , p , and \bar{p}
2. pseudo-rapidity : $1.0 < |\eta| < 2.4$, realistic gaussian distribution
3. p_T : $0.8 < p_T < 9.0$, realistic distribution for each rapidity slice
4. azimuthal angle : $0 < \phi < 2\pi$, randomly generated
5. z -vertex : $-35 \text{ cm} < z_{vtx} < 35 \text{ cm}$, flat distribution

Hadron cocktail package

As previously mentioned in several sections, two hadron shower codes, G-FLUKA and GHEISHA, implemented in the GEANT based PHENIX simulation framework do not reproduce the particle flux seen in the data. Here are properties of unmodified two hadron shower codes introduced in [49].

- The overall particle flux from GHEISHA is about half of that from G-FLUKA.
- GHEISHA tends to allow lower p_T particles especially p_T below 1.5 GeV/c .

- GHEISHA tends to allow more kaons than pions at the MuID Gap-4, whereas pions and kaons are similar in G-FLUKA.

Since the response in two hadron shower codes depends on p_T and particle, it is really difficult to reproduce the measured particle flux in the entire p_T range with the original hadron shower codes. Therefore, the nuclear interaction cross sections in the both hadron shower code are altered separately until the modified shower codes successfully reproduce the data. A certain version of the hadron shower code is referred as a *hadron cocktail package*. For example, a G-FLUKA simulation with 5% increased nuclear interaction cross section is called FL105. In order to well reproduce hadronic flux over the entire p_T range, several good hadron packages are combined. Details on the good hadron package selection and how to combine them are discussed in Sec. 3.4.5 and 3.5.2.

3.4.3 Tuning hadron cocktail

In order to match individual hadron package to the data, the initial hadron spectra for each hadron package are modified by using weighting factors extracted at the MuID Gap-2, 3, and 4. This match and modification of the initial hadron spectra could compensate defects from input hadron estimation and hadron shower codes. In previous analysis [53, 77], the weighting factors are calculated from reconstructed p_T bins, and these weighting factors are applied to the generated p_T spectra.

For the stopped hadrons at the MuID Gap-2 and 3, yield ratios be-

tween the data and the hadron cocktail are the weighting factors,

$$w_{Gap2}(p_T^{rec}) = \frac{N_{Gap2}^{MC}(p_T^{rec})}{N_{Gap2}^{data}(p_T^{rec})}, \quad w_{Gap3}(p_T^{rec}) = \frac{N_{Gap3}^{MC}(p_T^{rec})}{N_{Gap3}^{data}(p_T^{rec})}. \quad (3.6)$$

Weighting factors at MuID Gap-4 are determined as the ratio of slopes from normalized z -vertex distribution. These slopes indicate differential yield of decay muons $\left(\frac{dN}{dz}\right)_{Gap4} \propto \frac{d^3N}{dp_T d\eta dl}$,

$$w_{Gap4}(p_T) = \frac{(dN/dz)_{Gap4}^{data}}{(dN/dz)_{Gap4}^{MC}}. \quad (3.7)$$

One concern about this original tuning scheme is that the weighting factors to adjust input hadron spectra are from ratios of reconstructed tracks so that they are discontinuous. In this research, tuning matrix in Fig. 3.23 are applied to convert the information from the reconstructed tracks into the generated tracks. As shown in the tuning matrix, a lot of tracks are reconstructed in shifted p_T bins from the generated p_T bins due to energy loss and decay kinematics. Furthermore, overall distributions are different between the MuID Gap-3, dominated by stopped hadrons, and the MuID Gap-4, dominated by decay muons.

New weighting factors for the generated p_T bins are determined by matrix calculation between the tuning matrix and the weighting factors from reconstructed p_T bins. The weighting factor for a certain input p_T bin i is,

$$w(p_T^{gen i}) = \sum_j^{N_{rec p_T} \text{ bins}} \frac{N_{p_T}^{rec j, gen i}}{N_{p_T}^{gen i}} w(p_T^{rec j}). \quad (3.8)$$

Weighting factors for tunes at all MuID gaps as a function of generated p_T bin are determined from the Eq. 3.8. Figure 3.22 shows comparison of weighting factors from old and new scheme at the MuID Gap-3 and 4. Weighting factors from the new method are basically consistent with the previous ones as well as continuous and less fluctuating.

For selecting good hadron packages, each package is tuned with optimal weighting factors. This optimal weighting factor is calculated as a weighted sum of the weighting factors at MuID Gap-2, 3, and 4. Basic idea for this weighted sum is that the weighting factor at MuID Gap-4 (MuID Gap-2 and 3) is optimized for reproducing the decay muon (punch-through hadron). Therefore, the optimal weighting factor is determined as the simple average of $w_{Gap4}(p_T^{gen\ i})$ and $w_{Gap2,3}(p_T^{gen\ i})$,

$$w_{Opt}(p_T^{gen\ i}) = \frac{w_{Gap4}(p_T^{gen\ i}) + w_{Gap2,3}(p_T^{gen\ i})}{2}, \quad (3.9)$$

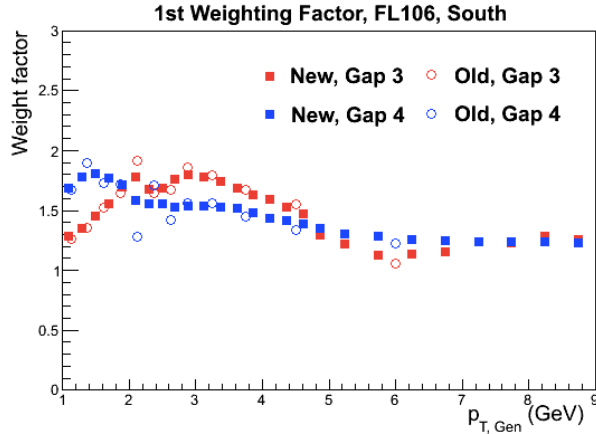


Figure 3.22: Comparison of weighting factors between two methods at MuID Gap-3 (red) and 4(blue).

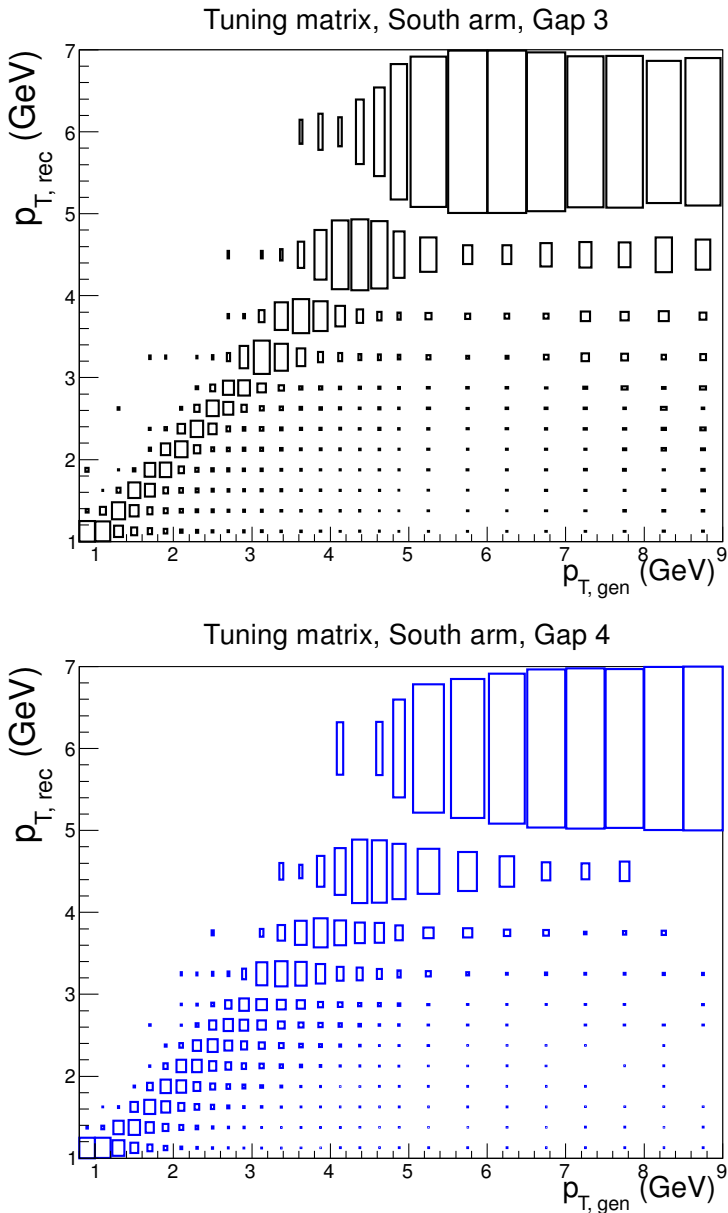


Figure 3.23: Tuning matrix for the stopped hadron at MuID Gap-3 (top) and the decay muon and punch-through hadron at MuID Gap-4 (bottom).

where $w_{Gap2,3}(p_T^{gen\ i})$ is an average of $w_{Gap2}(p_T^{gen\ i})$ and $w_{Gap3}(p_T^{gen\ i})$. The overall distributions and values of $w_{Gap2}(p_T^{gen\ i})$ and $w_{Gap3}(p_T^{gen\ i})$ are very close.

3.4.4 Trigger efficiency consideration

In this analysis, two MuIDLL1 (MuIDLL1H and MuIDLL1D) triggers are used as discussed in 2.5. Since there is not corresponding trigger configuration for hadron cocktail simulation, offline trigger emulator by mimicking the trigger logics with variables in the picoDST [49, 78] are used to apply the same trigger configurations applied to the data. However, intrinsic inefficiency of the MuIDLL1 triggers were found by comparing the MuIDLL1 triggered data to the MB triggered data. Moreover, as trigger efficiency depends on p_T and MuID Gap, tuning cocktail simulation at each MuID Gap might shows larger discrepancy. In order to avoid over- or under-correcting due to the offline trigger emulator, both the MB data and the MuIDLL1 triggered data were filtered with the offline emulator before the comparison.

Figure 3.24 and 3.25 show comparison of raw yield between the MB (filled points) and the MuIDLL1 (open points) triggered data for Run-8 $d+Au$ and Run-9 $p+p$, respectively. The bottom panel in each plot contains ratios. Efficiencies of the MuIDLL1D trigger (Gap-4) for both Run-8 and 9 as well as North and South seem to be ~ 1 over the entire p_T range. However, there are clear efficiency losses on the MuIDLL1H triggers especially at low p_T range. As the MuIDLL1 trigger calculates trigger logic based on hits from tracks, the MuIDLL1H trigger shows worse efficiency at MuID Gap-2 than at Gap-3. The trigger efficiency

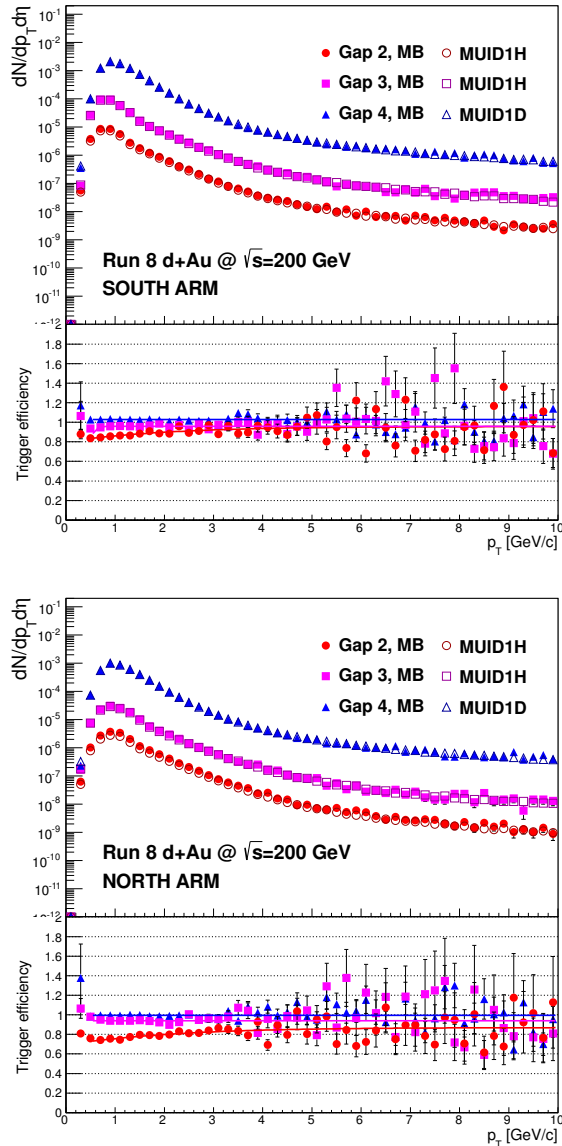


Figure 3.24: MuIDLL1 trigger efficiency at South (left) and North (right) arm for Run-8 $d+Au$.

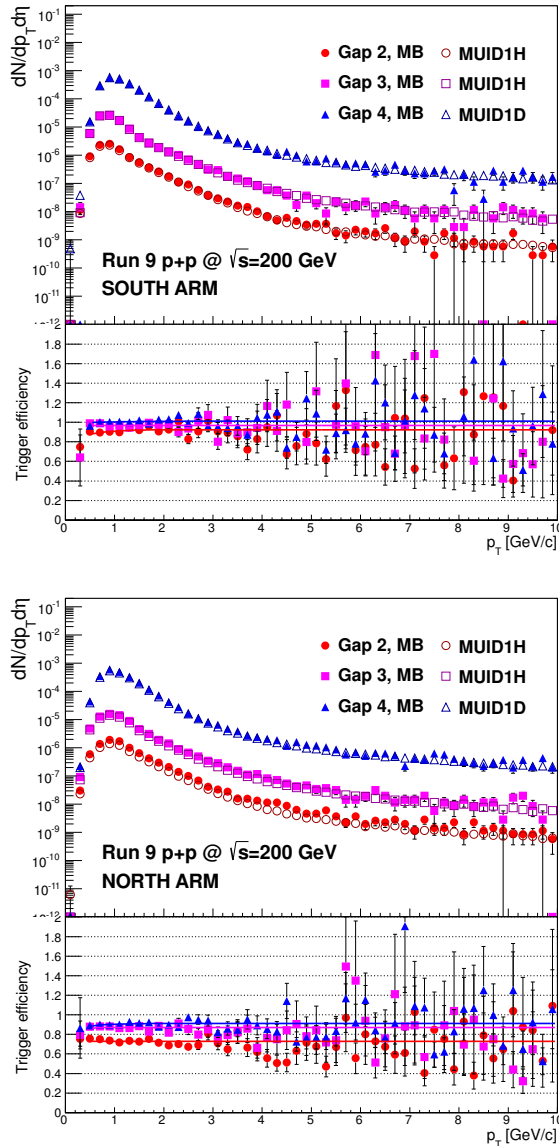


Figure 3.25: MuIDLL1 trigger efficiency at South (left) and North (right) arm for Run-9 $p+p$.

is determined by ratio of p_T spectra between the MuIDLL1 and the MB triggered data. The ratio is fit with the function as,

$$\epsilon_{trig} = \frac{a}{\exp[b - p_T]/c + 1}. \quad (3.10)$$

This function is referred from the heavy-flavor electron analysis to calculate ERT trigger efficiency [79]. The trigger efficiency for each MuIDLL1 trigger is corrected at the stage of tuning hadron cocktail simulations (matching to the data).

3.4.5 Hadron package selection

Several simulated hadron packages are tuned with the optimal weighting factor to check how well reproduce the data at the MuID Gap-2, 3, and 4 simultaneously. Good hadron packages to use for signal extraction are selected based on two factors below.

- **Stopped hadron yield at MuID Gap-2 and 3**

Raw yield of the stopped hadron at the MuID Gap-2 and 3 are compared between the data and the hadron packages. This match is important for the estimation of punch-through hadrons.

- **χ^2/ndf at MuID Gap-4**

Matching between the data and the hadron packages at the MuID Gap-4 is quantified by calculating χ^2/ndf of normalized z -vertex distributions as,

$$\chi^2_{Gap4}(p_T, i) = \sum_{j=1}^{N_{zbins}} \frac{\Delta z_j - \overline{\Delta z}}{\sigma_{z_j}^2 + \sigma_{\bar{z}}^2}, \quad (3.11)$$

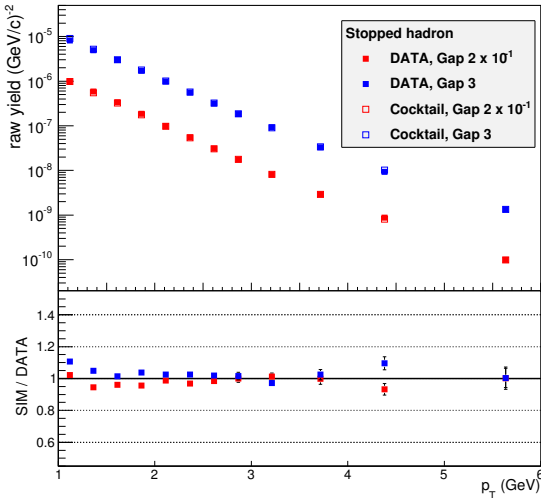


Figure 3.26: Comparison of the stopped hadron yield at MuID Gap-2 (red) and MuID Gap-3 (blue). The lower panel shows the cocktail of the data ratio.

where $\Delta z_i - \overline{\Delta z}$ equals $(z_j^{data} - \overline{z^{data}}) - (z_j^{MC} - \overline{z^{MC}})$. The normalized z -vertex distribution of inclusive tracks at the MuID Gap-4 is for the exact estimation of decay muons. Especially for low p_T bins where decay muons are dominant, matching with reduced χ^2/ndf is a important condition for good hadron packages.

Table 3.6: Good hadron cocktail packages used for the signal extraction.

| Run-8 $d+\text{Au}$ | | | | | |
|---------------------|-------|-------|------|------|------|
| FL103 | FL104 | FL105 | GH94 | GH95 | GH96 |
| Run-9 $p+p$ | | | | | |
| FL103 | FL104 | FL105 | GH94 | GH95 | GH96 |

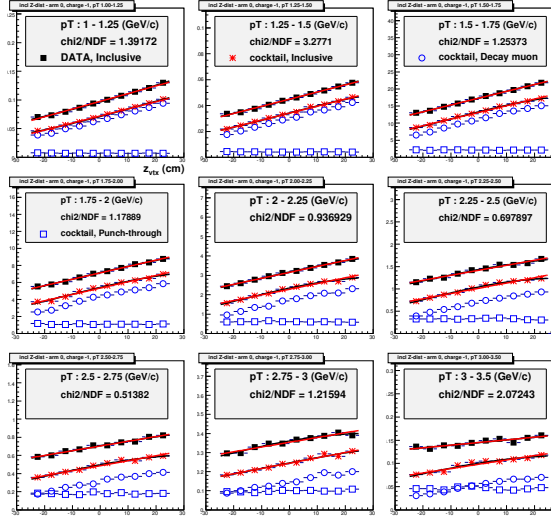


Figure 3.27: Matching slopes of normalized z -vertex distribution at MuID Gap-4 between the data (black squares) and the hadron cocktail (red star).

Figure 3.26 and 3.27 show an example hadron cocktail package after performing the optimal tune to the data. Figure 3.26 shows the stopped hadron raw yield at MuID Gap-2 and 3, and Fig. 3.27 shows the normalized z -vertex distribution at MuID Gap-4. Based on this kind of matching results from the optimal tune, good hadron packages are selected.

In this research, 6 cocktail packages are selected as the good ones for d +Au and p + p data separately. In Table 3.6, good hadron packages are listed, 3 hadron packages of each G-FLUKA and GHEISHA are used for both the d +Au and p + p data.

3.5 Signal extraction

The signal extraction is performed for each p_T bin by using 4 different tunes (MuID Gap-2, 3, 4, and optimal) of 6 good hadron packages. The procedure was originally adopted in the previous analysis [53, 80]. As previously discussed in Sec. 3.1.2, the invariant yield of heavy-flavor muon as a function of p_T is determined through following steps.

- Calculating heavy-flavor muon raw (uncorrected) yield for 4 different tunes (MuID Gap-2, 3, 4, and optimal) in each hadron cocktail package
- Averaging yields from the 4 different tunes and applying acceptance by efficiency correction for the final yield for each hadron cocktail package
- Combining yields of 6 hadron packages
- Subtracting muons from J/ψ decay by using decay simulation from the measured p_T spectra
- Applying bin shift correction
- In case of Run-9 $p+p$ which are symmetric collisions, combining the invariant yield of the South and North muon arms.

The details on above steps are described in following subsections.

3.5.1 Signal from one hadron cocktail package

As described in the Sec. 3.1.2, the heavy-flavor single muon yield for a certain p_T bin is calculated as,

$$Y(p_T) = \frac{1}{2\pi p_T} \frac{d^2 N^\mu}{dp_T dy}, \quad (3.12)$$

where p_T is the center of a given p_T bin, dp_T (dy) is the bin width of p_T (rapidity) bin, and N^μ is the number of heavy-flavor muons. The final heavy-flavor muon yield is determined by combining several hadron cocktail packages, and the invariant yield for a certain hadron cocktail package is calculated from 4 different tunes.

The heavy-flavor muon yield for a certain p_T bin i and a hadron cocktail package j is determined as,

$$\begin{aligned} Y_{Com,i,j} &= \frac{Y_{Gap23,i,j} + Y_{Gap4,i,j} + Y_{Gap234,i,j}}{3} \\ &= \frac{Y_{Gap2,i,j}}{4} + \frac{Y_{Gap3,i,j}}{4} + \frac{Y_{Gap4,i,j}}{4} + \frac{Y_{Gap234,i,j}}{4}, \end{aligned} \quad (3.13)$$

where $Y_{Gap23,i,j}$ is a simple average of $Y_{Gap2,i,j}$ and $Y_{Gap3,i,j}$, and $Y_{Gapk,i,j}$ is the heavy-flavor muon yield from the tune to reproduce the data at MuID Gap- k . The heavy-flavor muon yield $Y_{Gap23,i,j}$, which is tuned at the MuID Gap-2, 3, is expected to optimized for estimation of the punch-through hadrons, and the ($Y_{Gap4,i,j}$), which is tuned at the MuID Gap-4, is optimized for the decay muon estimation. The $Y_{Gap234,i,j}$ is a obtained yield from the optimal tune as described in Sec. 3.4.5.

The systematic uncertainty on the invariant yield from a certain hadron cocktail package due to the difference between 4 tunes, referred to

$\sigma_{Pack\ Mismatch,i,j}$, is determined as,

$$\begin{aligned}\sigma_{Pack\ Mismatch,i,j}^2 = & \frac{(Y_{Gap2,i,j} - Y_{Com,i,j})^2}{4} + \frac{(Y_{Gap3,i,j} - Y_{Com,i,j})^2}{4} \\ & + \frac{(Y_{Gap4,i,j} - Y_{Com,i,j})^2}{4} + \frac{(Y_{Gap234,i,j} - Y_{Com,i,j})^2}{4}\end{aligned}\quad (3.14)$$

3.5.2 Combining hadron cocktail packages

The combining heavy-flavor muon yield from 6 hadron cocktail packages is determined as a weighted sum. The combined yield for a certain p_T bin i is calculated as,

$$\langle Y_i \rangle = \sum_{j=1}^{N_{package}} w_{i,j} Y_{Com,i,j}, \quad (3.15)$$

where

$$w_{i,j} \equiv \frac{\frac{1}{\sigma_{i,j}^2}}{\sum_{j=1}^{N_{package}} \frac{1}{\sigma_{i,j}^2}}, \quad (3.16)$$

and $\sigma_{i,j}$ is a quadratic sum of the statistical and systematic uncertainties as $\sigma_{i,j}^2 = \sigma_{stat,i,j}^2 + \sigma_{sys,i,j}^2$. The systematic uncertainty on the heavy-flavor muon yield for a certain p_T bin i is determined as the variance of the weighted sample mean. The detailed calculation is like

below.

$$\begin{aligned}
Var(<Y_i>) &= \sum_{j=1}^{N_{package}} w_{i,j}^2 Var(Y_{Com,i,j}) \\
&\quad + 2 \sum_{j < m}^{N_{package}} w_{i,j}^2 w_{i,m}^2 Cov(Y_{Com,i,j}, Y_{Com,i,m}) \\
&= \sum_{j=1}^{N_{package}} w_{i,j}^2 \sigma_{i,j}^2 + 2 \sum_{j < m}^{N_{package}} w_{i,j}^2 w_{i,m}^2 \sigma_{pack\ common,i}^2 \\
&= \sum_{j=1}^{N_{package}} w_{i,j}^2 \sigma_{i,j}^2 + \sum_{j=1}^{N_{package}} \sum_{j \neq m}^{N_{package}} w_{i,j}^2 w_{i,m}^2 \sigma_{pack\ common,i}^2,
\end{aligned} \tag{3.17}$$

where $\sigma_{pack\ common,i}^2$ is the correlated uncertainty between the hadron cocktail packages. This includes the systematic uncertainties due to the input hadron estimation (σ_{Cock}^2) and the acceptance by efficiency calculation ($\sigma_{A\epsilon}^2$), and the statistical uncertainty (σ_{Stat}^2). The detailed description for each source of the systematic uncertainty is in 3.7.

Figure 3.28 shows comparison of invariant yield from different hadron packages at the South (top) and the North (bottom) arms in the Run-9 $p+p$ data. Lower panels in both plots shows the fractional difference between the hadron packages and the combined point. Over the entire p_T range, the fractional difference of each hadron package is less than 20%.

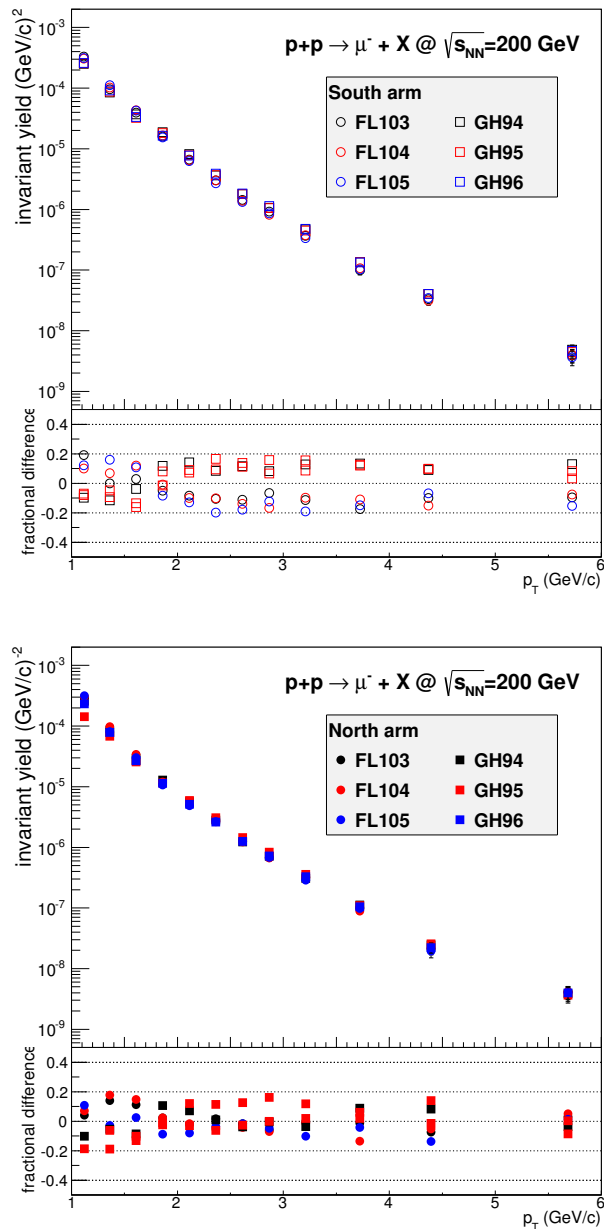


Figure 3.28: Comparison of the heavy-flavor muon yield from different hadron packages at South (top) and North (bottom) muon arms. Lower panel in each plot shows variations of hadron packages from the combined points.

3.5.3 Subtraction of muons from J/ψ decay

The subtracted background, calculated from the haron cocktail method, includes background tracks from light hadrons (π , K , and p). The obtained heavy-flavor muons are mostly from open-charm and open-bottom hadrons (D , B , etc.), but there are still contributions from quarkonia and low mass vector meson decays as discussed in Sec. 3.1.1. Among these minor background sources, the contribution from J/ψ can be calculated and subtracted based on the PHENIX J/ψ measurements at the muon arm in $p+p$ [81] and $d+Au$ [37] collisions.

The subtraction technique have been adopted widely in the heavy-flavor electron analysis [59, 82]. By using a decay generator named EXODUS, the p_T spectrum of daughter muons can be calculated from the mother J/ψ p_T spectrum. The subtraction is performed p_T bin by p_T bin, the p_T spectrum after the subtraction is closer to the p_T spectrum of pure open heavy-flavor hadrons. The calculation of the muon production from J/ψ decays was performed in [83], and the steps are following.

1. Parameterize the p_T spectrum of J/ψ by fitting to the measured data with a Hagedorn function,

$$B_{\mu^+\mu^-} \frac{1}{2\pi p_T} \frac{d^2 N}{dp_T dy} = \frac{a_3}{[e^{a_1 \cdot p_T - a_2 \cdot p_T^2} + p_T/p_0]^n}, \quad (3.18)$$

and a Kapalan function,

$$B_{\mu^+\mu^-} \frac{1}{2\pi p_T} \frac{d^2 N}{dp_T dy} = \frac{A}{[1 + (p_T/B)^2]^q}. \quad (3.19)$$

2. By using the EXODUS tool, generate J/ψ based on a uniform p_T spectrum within the muon arm rapidity range, and perform decay simulation to obtain the p_T spectrum of decayed muon.
3. Weight the p_T spectrum calculated in Step 2 by the parameterization obtained in Step 1 to consider the realistic mother's p_T spectrum.

Figure 3.29 shows the results of parameterization of mother J/ψ production in 0-100% d +Au collisions [83]. As both two function fit to the data reasonably well, average of the two fit functions is used for the Step 3 in the above process. The contribution of muons from J/ψ to inclusive heavy-flavor muons is very small at low p_T but increases up to $\sim 20\%$ at $p_T \approx 5 \text{ GeV}/c$, as shown in Fig. 3.30. Similar results are obtained in the $p+p$ and the other centrality of d +Au data [83]. Systematic uncertainties from this subtraction are determined as the variation of daughter muon p_T spectra between the upper and lower limit of statistical uncertainties in the mother J/ψ p_T spectrum, and the values are less than 1% over the entire p_T region.

3.5.4 Bin shift correction

Due to statistical limitation, the data is analyzed by using certain ranges of p_T bins. However, the p_T spectra of particle production usually follow the exponential shape, so the drop inside a p_T bin is not small. During the background subtraction, the average values of p_T ($\langle p_T \rangle$) is used for the yield calculation. For the final results, the invariant yield for a certain p_T bin is corrected up or down in order to plot the data point on the center of p_T bin.

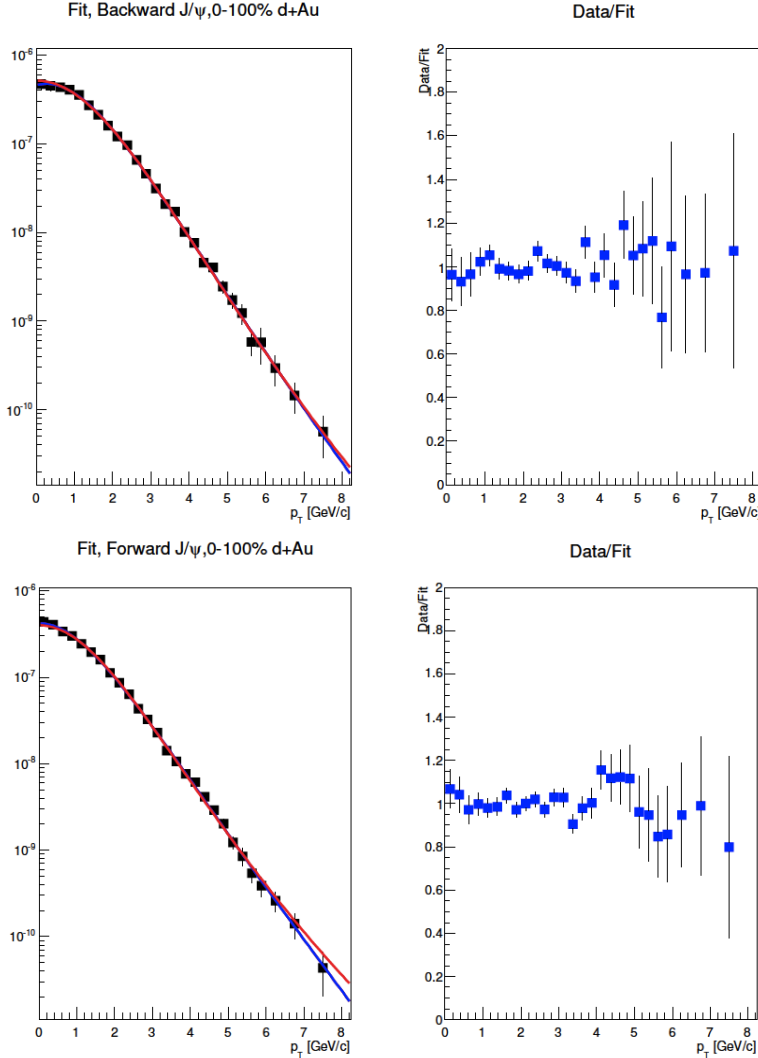


Figure 3.29: Examples of the parameterization of J/ψ production in 0-100% centrality $d+Au$ collisions at backward and forward (top) and forward (bottom) rapidity. The left panels show J/ψ p_T spectra [37] and fit functions, and the ratios between the data and average of two fit function are shown in the right panels [83].

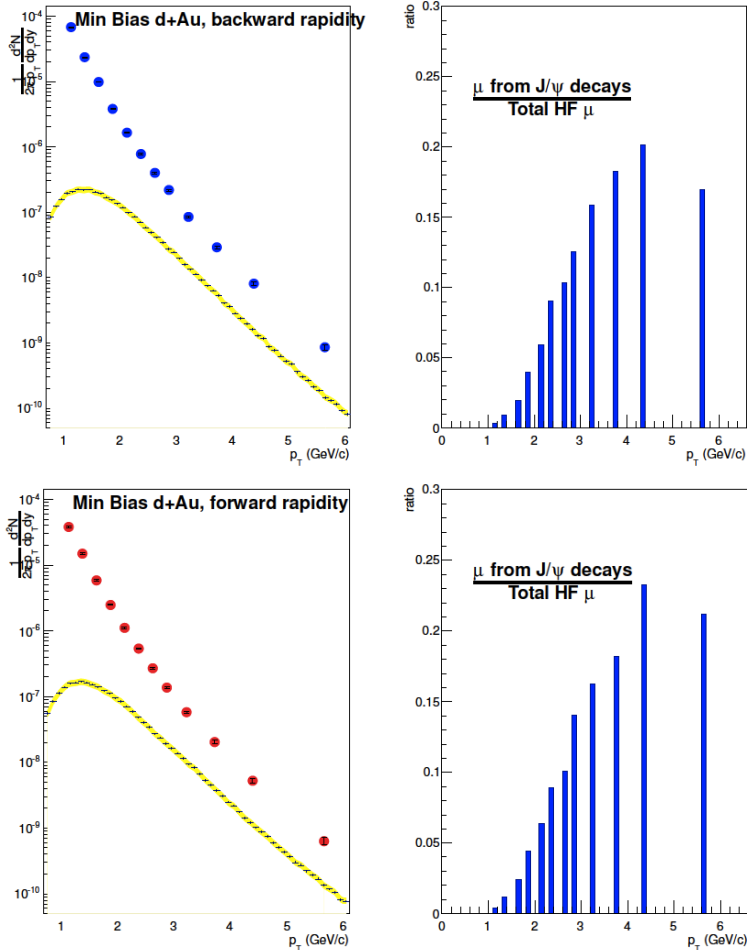


Figure 3.30: Comparison of inclusive heavy-flavor muons (data points) and muons from J/ψ (yellow line) in 0–100% centrality $d+Au$ collisions. The left panels show the fraction of muons from J/ψ in inclusive heavy-flavor muons [83].

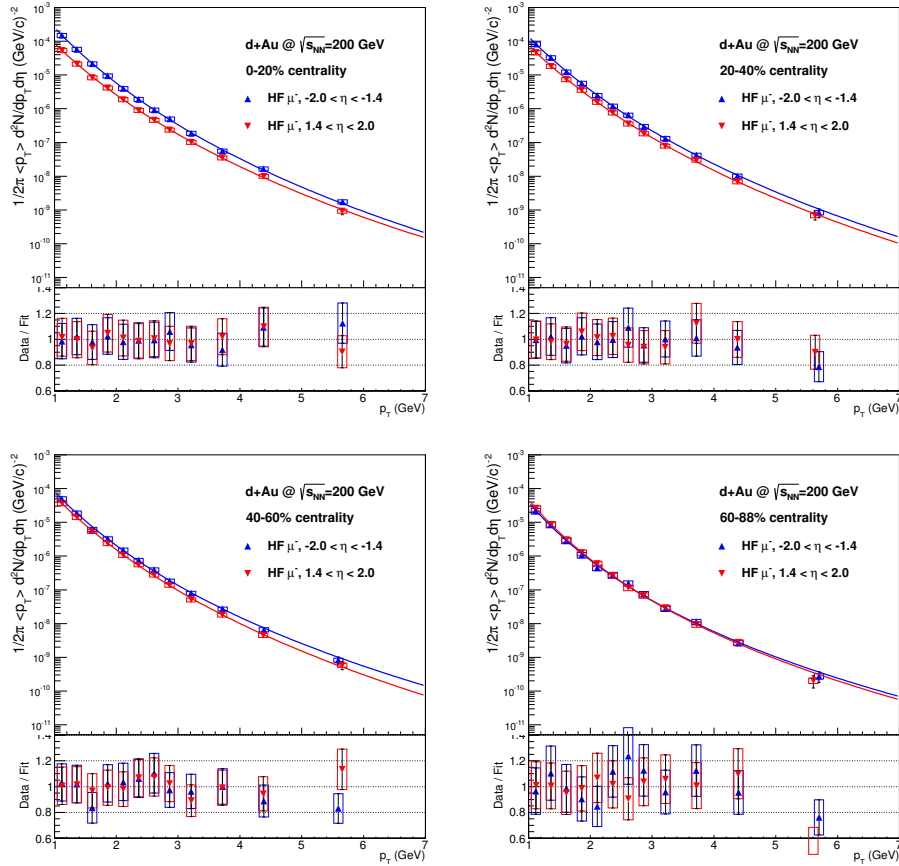


Figure 3.31: Fit to the invariant yield of heavy-flavor muons in different centrality classes of $d+Au$ collisions for the bin shift correction. The lower panels show the ratio between the data and fit function.

The bin shift correction is performed based on the previous method for the PHENIX results [49, 84], and the yield is corrected as,

$$Y_{corrected} = \frac{Y_{uncorrected}}{R}. \quad (3.20)$$

Where R is correction factor obtained from a fit function to the data. The same function for the parameterization of J/ψ production, Eq. 3.19, is used to fit to the invariant yield of heavy-flavor muons. The correction factor R is calculated as,

$$R = \frac{\int_{p_T^c + \Delta/2}^{p_T^c - \Delta/2} f(p_T) dp_T}{\Delta f(p_T^c)}, \quad (3.21)$$

where p_T^c is the central value of the p_T bin, Δ is the p_T bin width, and $f(p_T)$ is the fit function. Figure 3.31 shows fit results to the invariant yield in the four different centrality classes of d +Au collisions. In Table 3.7, calculated bin shift correction factors, R , for all p_T bins of invariant yield from the p + p and d +Au data sets are listed.

3.5.5 Combining two arms in p + p collisions

In case of the invariant yield in p + p collisions, which are symmetric collisions, two independent measurements at backward (South arm) and forward (North arm) rapidity are combined to produce more precise results. A basic scheme to combine two results is same as the technique to combine several hadron cocktail packages. Several analyses have adopted the similar method for the combined arm results [53, 77, 49, 85]. The combined invariant yield of heavy-flavor

Table 3.7: Bin shift correction factors depending on p_T bins for $p+p$ and different centrality classes $d+\text{Au}$ data at South and North arms.

| arm | p_T | $p+p$ | 0-100% | 0-20% | 20-40% | 40-60% | 60-88% |
|-----|-------|-------|--------|-------|--------|--------|--------|
| S | 1.125 | 1.055 | 1.048 | 1.050 | 1.045 | 1.049 | 1.062 |
| S | 1.375 | 1.044 | 1.040 | 1.042 | 1.039 | 1.041 | 1.049 |
| S | 1.625 | 1.037 | 1.034 | 1.036 | 1.033 | 1.034 | 1.039 |
| S | 1.875 | 1.031 | 1.030 | 1.031 | 1.029 | 1.029 | 1.032 |
| S | 2.125 | 1.026 | 1.026 | 1.027 | 1.026 | 1.025 | 1.027 |
| S | 2.375 | 1.023 | 1.023 | 1.024 | 1.023 | 1.022 | 1.023 |
| S | 2.625 | 1.020 | 1.020 | 1.021 | 1.020 | 1.019 | 1.020 |
| S | 2.875 | 1.017 | 1.018 | 1.019 | 1.018 | 1.017 | 1.017 |
| S | 3.250 | 1.060 | 1.064 | 1.067 | 1.065 | 1.059 | 1.058 |
| S | 3.750 | 1.048 | 1.052 | 1.055 | 1.054 | 1.048 | 1.046 |
| S | 4.500 | 1.153 | 1.170 | 1.181 | 1.176 | 1.154 | 1.143 |
| S | 6.000 | 1.423 | 1.494 | 1.530 | 1.521 | 1.432 | 1.382 |
| N | 1.125 | 1.076 | 1.044 | 1.042 | 1.042 | 1.047 | 1.064 |
| N | 1.375 | 1.056 | 1.038 | 1.036 | 1.036 | 1.040 | 1.050 |
| N | 1.625 | 1.044 | 1.033 | 1.031 | 1.032 | 1.034 | 1.041 |
| N | 1.875 | 1.035 | 1.028 | 1.027 | 1.028 | 1.029 | 1.034 |
| N | 2.125 | 1.028 | 1.025 | 1.024 | 1.025 | 1.026 | 1.028 |
| N | 2.375 | 1.023 | 1.022 | 1.021 | 1.022 | 1.023 | 1.024 |
| N | 2.625 | 1.020 | 1.019 | 1.019 | 1.020 | 1.020 | 1.021 |
| N | 2.875 | 1.017 | 1.017 | 1.017 | 1.018 | 1.018 | 1.018 |
| N | 3.250 | 1.057 | 1.062 | 1.060 | 1.064 | 1.064 | 1.062 |
| N | 3.750 | 1.044 | 1.051 | 1.050 | 1.053 | 1.052 | 1.049 |
| N | 4.500 | 1.132 | 1.169 | 1.164 | 1.178 | 1.171 | 1.154 |
| N | 6.000 | 1.340 | 1.495 | 1.479 | 1.534 | 1.496 | 1.417 |

muons for a certain p_T bin i is determined as,

$$\begin{aligned} <Y_i> &= \sum_{j=1}^{N_{arm}} w_{i,j} Y_{i,j} \\ &= w_{i, South} Y_{i, South} + w_{i, North} Y_{i, North}, \end{aligned} \quad (3.22)$$

where

$$w_{i,j} \equiv \frac{\frac{1}{\sigma_{i,j}^2}}{\sum_{j=1}^{N_{arm}} \frac{1}{\sigma_{i,j}^2}}. \quad (3.23)$$

The total uncertainty for a certain p_T bin i and a certain muon arm j is calculated as a quadratic sum of the systematic and the statistical uncertainties,

$$\begin{aligned} \sigma_{i,j}^2 &= \sigma_{stat,i,j}^2 + \sigma_{sys,i,j}^2 \\ &= \sigma_{stat,i,j}^2 + \sigma_{Pack\ Mismatch,i,j}^2 + \sigma_{A\epsilon}^2 + \sigma_{arm\ common}^2. \end{aligned} \quad (3.24)$$

The detailed description for each source of the systematic uncertainties is contained in Sec. 3.7. The systematic uncertainty for the combined invariant cross section is calculated as,

$$\begin{aligned} Var(<Y_i>) &= \sum_{j=1}^{N_{arm}} w_{i,j}^2 Var(Y_{i,j}) + 2 \sum_{j < m}^{N_{package}} w_{i,j}^2 w_{i,m}^2 Cov(Y_{i,j}, Y_{i,m}) \\ &= \sum_{j=1}^{N_{arm}} w_{i,j}^2 \sigma_{i,j}^2 + 2 \sum_{j < m}^{N_{arm}} w_{i,j}^2 w_{i,m}^2 \sigma_{arm\ common}^2 \\ &= \sum_{j=1}^{N_{arm}} w_{i,j}^2 \sigma_{i,j}^2 + \sum_{j=1}^{N_{arm}} \sum_{j \neq m}^{N_{arm}} w_{i,j}^2 w_{i,m}^2 \sigma_{arm\ common}^2, \end{aligned} \quad (3.25)$$

where $\sigma_{\text{arm common}}$ is the correlated uncertainty of both muon arms due to the initial hadron input (σ_{Cock}) and the MB trigger (σ_{BBC}),

$$\sigma_{\text{arm common}}^2 = \sigma_{\text{Cock}}^2 + \sigma_{\text{BBC}}^2. \quad (3.26)$$

3.6 Nuclear modification factor, R_{dA}

In order to quantify the medium effects in $d+\text{Au}$ collisions, the nuclear modification factor R_{dA} is calculated for a given centrality class of $d+\text{Au}$ collisions. The nuclear modification factor R_{dA} for a certain p_T bin is calculated as the following formula.

$$R_{dA}(p_T) = \frac{dY_{d\text{Au}}}{\langle T_{d\text{Au}} \rangle \, d\sigma_{pp}}, \quad (3.27)$$

where $dY_{d\text{Au}}$ ($d\sigma_{pp}$) is the differential heavy-flavor muon yield (cross section) in $d+\text{Au}$ ($p+p$) collisions in a given p_T and rapidity range, and $\langle T_{d\text{Au}} \rangle$ is the nuclear overlap function for a certain centrality range of $d+\text{Au}$ collisions. This equation can be re-written as,

$$R_{dA}(p_T) = \frac{dY_{d\text{Au}}}{\langle N_{\text{coll}} \rangle \, dY_{pp}}, \quad (3.28)$$

where dY_{pp} is the differential heavy-flavor muon yield in $p+p$ collisions, and $\langle N_{\text{coll}} \rangle$ is the average number of binary collisions for a certain $d+\text{Au}$ centrality class. The $\langle N_{\text{coll}} \rangle$ is determined from Glauber model calculation [68], and the values for analyzed centrality classes are listed in Table 2.4. In this research, both $d+\text{Au}$ and $p+p$ data sets are analyzed, and p_T spectra are obtained for exact same p_T bins.

Therefore, R_{dA} for a certain p_T bin is calculated as a yield ratio between $d+\text{Au}$ and $p+p$ collisions, so systematic uncertainties due to any extrapolation with fit functions could be removed.

3.7 Systematic uncertainty

3.7.1 Invariant yield

As described in Sec. 3.1.2, the invariant yield of heavy-flavor muon is determined as,

$$\frac{d^2N^\mu}{2\pi p_T dp_T dy} = \frac{1}{2\pi p_T \Delta p_T \Delta y} \frac{N_I - N_C - N_F - N_{J/\psi}}{(N_{\text{evt}}/\epsilon_{BBC})A\epsilon}. \quad (3.29)$$

In this equation, estimated quantities, N_C , N_F , $N_{J/\psi}$, ϵ_{BBC} , and $A\epsilon$, are sources of the systematic uncertainty. Brief summary of each component is in Table 3.8. Systematic uncertainties from the estimation of

Table 3.8: Source of the systematic uncertainty on invariant yield of heavy-flavor muons

| name | source | description |
|---------------------------------|------------------|--|
| $\sigma_{\text{Pack Mismatch}}$ | N_C | variation between 4 tunes (p_T & cocktail package uncorrelated) |
| σ_{Cock} | N_C | initial hadron input spectra (p_T & cocktail package correlated) |
| σ_{BBC} | ϵ_{BBC} | BBC trigger and centrality determination (p_T & cocktail package correlated) |
| $\sigma_{A\epsilon}$ | $A\epsilon$ | acceptance by efficiency calculation (p_T & cocktail package correlated) |

N_F and $N_{J/\psi}$ are negligible ($< 1\%$) compared to other components. Details on the sources of systematic uncertainties and their estimation are shown below.

$\sigma_{\text{Pack Mismatch}}$

$\sigma_{\text{Pack Mismatch}}$ is the systematic uncertainty due to variation between different tunes at the MuID Gap-2, 3, and 4 of a certain hadron cocktail package. Therefore, **$\sigma_{\text{Pack Mismatch}}$** is independent on the \mathbf{p}_T bin and the hadron cocktail package. This uncertainty is calculated as the mean difference between 4 tunes of a hadron cocktail package, and the exact formula is Eq. 3.17. The **$\sigma_{\text{Pack Mismatch}}$** is larger especially at low \mathbf{p}_T region, because hadron shower codes shows larger uncertainties on describing low \mathbf{p}_T hadron fluxes. In addition, the dominant background source at low \mathbf{p}_T region is the decay muon, so tuning with the stopped hadrons at the MuID Gap-2 and 3 results in larger variation between tunes.

σ_{Cock}

σ_{Cock} is related to uncertainties on the initial hadron spectra (K/π ratio) and the overall simulation chain for the hadronic background (N_C) estimation. In the previous data analysis [53], this systematic uncertainty was determined as $\frac{\text{background}}{\text{signal}} \times 10\%$. This was based on a conservative estimation method that 10% uncertainty of the initial hadron spectra (background) could propagate to the yield of heavy-flavor muon (signal) proportional to $\frac{\text{background}}{\text{signal}}$. In this research, another method to figure out realistic propagation of the background uncertainty to the signal through hadron simulations and tuning to the data. The yield variation of signal from each hadron cocktail package according to K/π ratio varying up to $\pm 30\%$ has been compiled.

Figure 3.32 shows the fractional yield variations for different hadronic packages depending on \mathbf{p}_T in the MB d +Au data. As shown in these figures, the actual yield variations due to the uncertainty of initial hadron spectra are less than 10%. This indicates that the current analysis technique, matching the hadron cocktail packages to the data at MuID Gaps, helps to suppress the propagation of initial uncertainties. Based on the study, $10 \sim 15\%$ uncertainties are assigned to σ_{Cock} depending on centrality classes.

ϵ_{BBC}

ϵ_{BBC} contains uncertainties on the BBC trigger efficiency and the centrality determination of d +Au collisions as discussed in Sec. 2.5.1 and 2.6. The PHENIX collaboration performed precise studies to clarify these uncertainties [66, 67]. The uncertainty values depending on centrality are listed in 2.4.

$A\epsilon$

$A\epsilon$ is associated with the acceptance by efficiency calculation. This uncertainty includes inefficiencies of detectors (MuTr and MuID) and acceptance mis-match between the data and the MC. A brief summary

Table 3.9: Source of the systematic uncertainty on acceptance by efficiency calculation

| name | description | value |
|----------------------|--------------------------|------------|
| σ_{MuTr} | MuTr efficiency | 4% |
| σ_{MuID} | MuID efficiency | 2% |
| σ_{run} | run to run variation | 2% |
| σ_{φ} | MC/data acceptance match | $\sim 8\%$ |
| $\sigma_{A\epsilon}$ | total sum | $\sim 9\%$ |

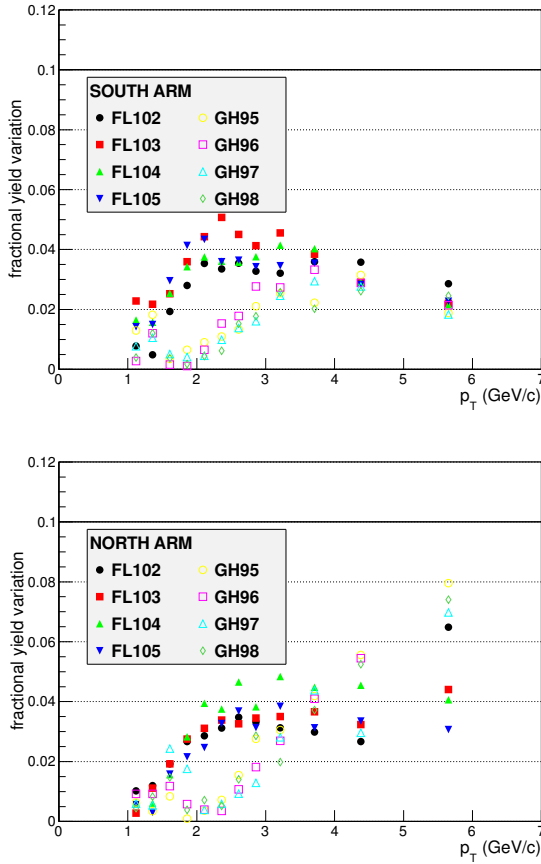


Figure 3.32: Yield variation of hadron cocktail packages by $\pm 30\%$ of K/π ratio change for South (North) arm in the d +Au data

for all components are listed in Table 3.9. σ_{MuTr} and σ_{MuID} are related to intrinsic detector performance, and the values are referred to the dimuon studies [37, 86]. During the data taking period which is typically longer than three months, condition of the detectors usually varies due to problems on high or low voltages, gas system, and data taking operation. In addition, the acceptance by efficiency calculation

is performed with limited number of reference runs, so discrepancy between the data and the simulation of reference runs is inevitable. In order to minimize the variation during the data taking period, proper geometrical cuts are applied. These fiducial cuts also help to improve acceptance match between the data and the MC simulation. Finally, $\sigma_{A\epsilon}$ is due to irreducible acceptance mis-match, and this is estimated based on φ distributions of the data and the MC as shown in Fig. 3.15. The final value of the $\sigma_{A\epsilon}$ is determined as a quadratic sum of values from four components as listed in Table 3.9.

3.7.2 Nuclear modification factor

As discussed in Sec. 3.6, the nuclear modification factor \mathbf{R}_{dA} is determined as,

$$\mathbf{R}_{dA}(p_T) = \frac{d\mathbf{Y}_{dAu}}{\langle N_{\text{coll}} \rangle d\mathbf{Y}_{pp}}, \quad (3.30)$$

where \mathbf{Y}_{dAu} (\mathbf{Y}_{pp}) is the invariant yield of heavy-flavor muons and $\langle N_{\text{coll}} \rangle$ is the average number of binary collisions of corresponding centrality class. The systematic uncertainty of \mathbf{R}_{dA} is determined as a quadratic sum of the systematic uncertainties of invariant yield of $d+Au$ and $p+p$ collisions. Although two data sets, $p+p$ and $d+Au$ data, have been analyzed along the exactly same procedure, any systematic uncertainty is not canceled out due to ambiguous correlations between the two data sets. The uncertainties in the $\langle N_{\text{coll}} \rangle$ and the BBC efficiency are treated as global uncertainties.

Chapter 4

Results

4.1 heavy-flavor muon p_T spectra

Based on the analysis steps described in the previous section, p_T spectra of heavy-flavor muons in $p+p$ and $d+\text{Au}$ collisions are obtained. Figure 4.1 shows the invariant cross section of negatively muons from open heavy-flavor decay. Bars and boxes around the data points refer to the statistical and systematic uncertainties, respectively. A solid line is a modified Kaplan function, $A[1 + (p_T/8.3)^2]^{-3.9}$ [87], fit to the $p+p$ data. Figure 4.2 shows the invariant yield of heavy-flavor muons in $d+\text{Au}$ collisions for five different centrality classes; 0–100%, 0–20% (most central), 20–40%, 40–60%, and 60–88% (most peripheral) at backward (top) and forward (bottom) rapidity ranges. The black data points are from $p+p$ shown in Fig. 4.1. Solid lines are also the modified Kaplan function, fit to the p_T spectrum in $p+p$ collisions, and then scaled by $\langle N_{\text{coll}} \rangle$ for each $d+\text{Au}$ centrality class.

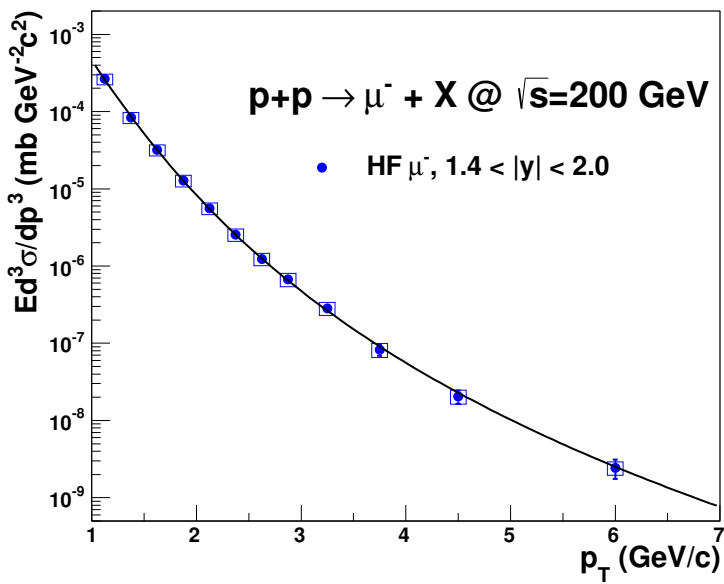


Figure 4.1: Invariant cross section of heavy-flavor muon in $p+p$ collisions. The solid line is a Kaplan function fit to the data.

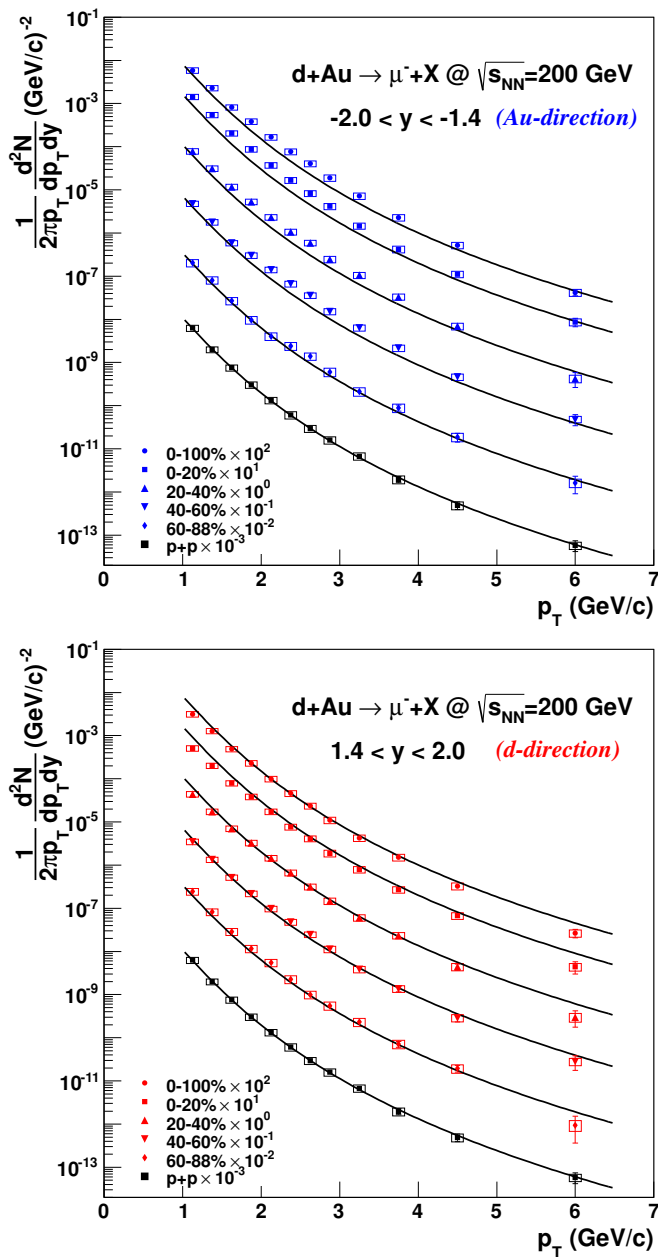


Figure 4.2: Invariant yield of heavy-flavor muon in $d+Au$ collisions for different centrality classes at backward (top) and forward (bottom) rapidity. Details are described in text.

4.2 Nuclear modification function, $R_{dA}(p_T)$

Based on the measured p_T spectra shown in the previous section, the nuclear modification factor R_{dA} as a function of p_T is calculated as described in Sec. 3.6. Figure 4.3, 4.4, 4.5, 4.6, and 4.7 show the nuclear modification factors at backward (blue circles) and forward (red squares) rapidity for 0–100%, 0–20% (most central), 20–40%, 40–60%, and 60–88% (most peripheral) centrality classes, respectively. Bars (Boxes) around the data points are the statistical (systematic) uncertainties. The systematic uncertainty for a certain p_T bin is determined as a quadratic sum of the systematic uncertainties of invariant yield in $p+p$ and $d+A$ collisions as described in Sec. 3.7.2. The black box around the unity on the right edge in each figure refer to the global scaling uncertainty considering uncertainties on the minimum bias trigger as well as the centrality and the $\langle N_{\text{coll}} \rangle$ determination.

As shown in Fig. 4.4, heavy-flavor muon production in the most central (0–20%) $d+A$ collisions relative to $p+p$ collisions shows an opposite trend of modification depending on rapidity. At backward rapidity (Au-going direction), heavy-flavor muon production is clearly enhanced relative to the $p+p$ data ($R_{dA} > 1$), whereas a suppression ($R_{dA} < 1$) is observed at forward rapidity (d-going direction). As centrality goes from central to peripheral, the magnitude of modification becomes smaller. Finally, in the most peripheral (60–88%) collisions, R_{dA} at both forward and backward rapidity are consistent with the unity over the entire p_T region. These results indicate the rapidity dependent strong cold nuclear matter (CNM) effects in heavy quark production. More discussion and comparison to model calculations will

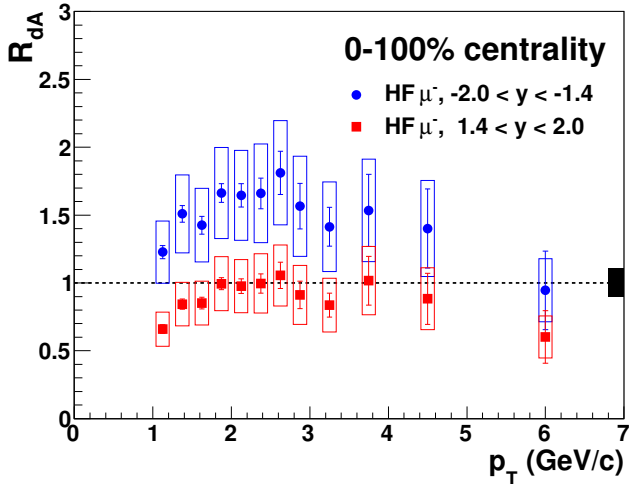


Figure 4.3: Nuclear modification factor R_{dA} as a function of p_T in 0-100% centrality d +Au collisions.

be in Sec. 5.3.

4.3 Nuclear modification function, $R_{dA}(\langle N_{coll} \rangle)$

In order to close look at the centrality dependence of heavy quark production, the nuclear modification factor R_{dA} is plotted as a function of $\langle N_{coll} \rangle$. Figure 4.8 shows such R_{dA} distribution for two p_T ranges, $1 < p_T < 3 \text{ GeV}/c$ (upper panel) and $3 < p_T < 5 \text{ GeV}/c$ (lower panel). As briefly discussed in the previous section, Sec. 4.2, the modifications of heavy-flavor muon production become stronger as the $\langle N_{coll} \rangle$ increases at both rapidity and p_T ranges. At both p_T ranges, the larger enhancement (suppression) is observed in more central collisions at backward (forward) rapidity. More discussion and comparison to model calculations will be in Sec. 5.3.

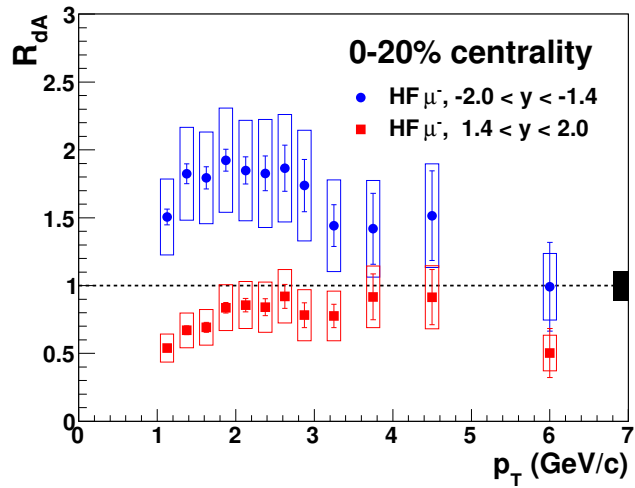


Figure 4.4: Nuclear modification factor R_{dA} as a function of p_T in 0-20% centrality d +Au collisions.

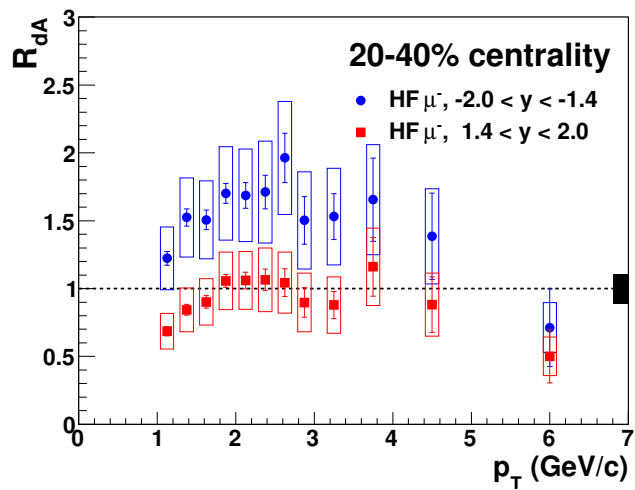


Figure 4.5: Nuclear modification factor R_{dA} as a function of p_T in 20-40% centrality d +Au collisions.

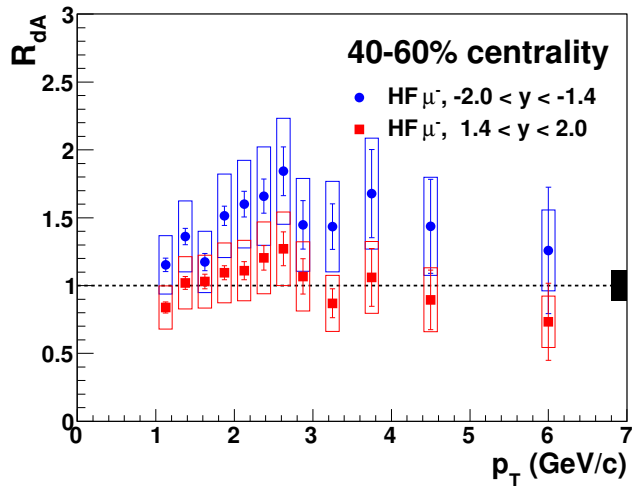


Figure 4.6: Nuclear modification factor R_{dA} as a function of p_T in 40-60% centrality d +Au collisions.

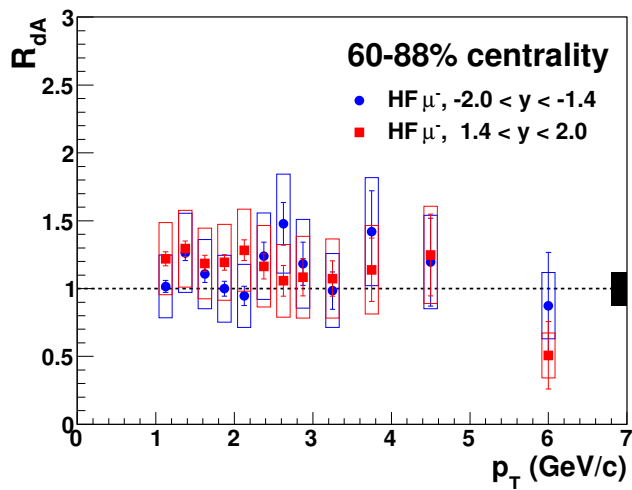


Figure 4.7: Nuclear modification factor R_{dA} as a function of p_T in 60-88% centrality d +Au collisions.

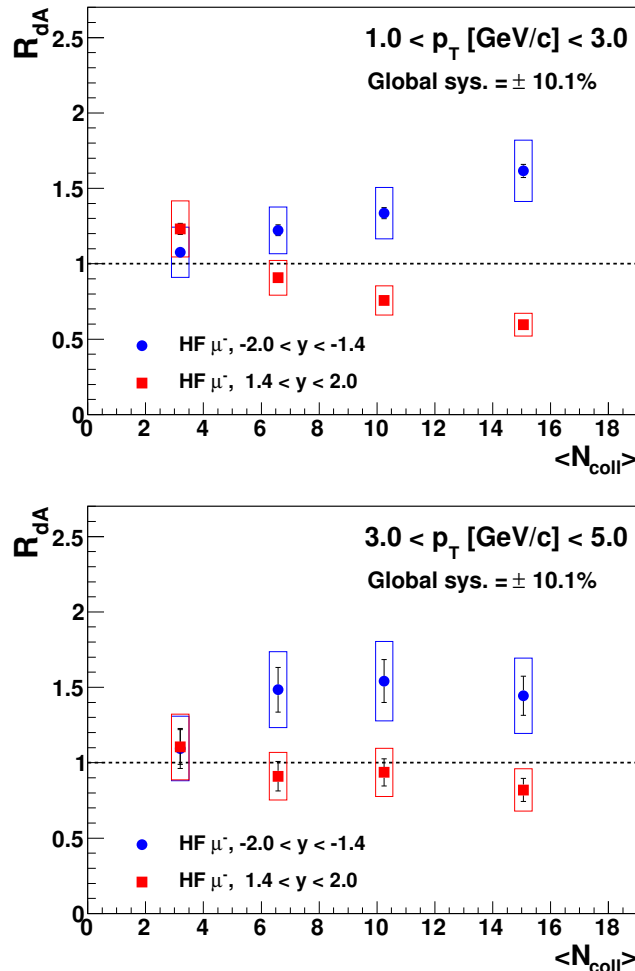


Figure 4.8: p_T integrated R_{dA} for two p_T ranges, $1 < p_T < 3 \text{ GeV}/c$ (upper) and $3 < p_T < 5 \text{ GeV}/c$ (lower), at backward and forward rapidity.

Chapter 5

Discussion

5.1 p_T spectra in $p+p$ collisions

Figure 5.1 shows comparisons of the heavy-flavor muon p_T spectra with a FONLL calculation [51, 52] and the previous PHENIX results [53]. The charm (blue) and bottom (red) components from the FONLL calculation are also plotted separately on the upper panel, and yellow bands represent the upper and lower uncertainties of the theoretical calculation. Lower panel shows ratio of the data to the FONLL calculation, and the bands indicates systematic uncertainties¹.

In the comparison to the previous PHENIX results, the new results (Run-9 data) are consistent with the previous measurement (Run-5 data) within uncertainties. Both statistical and systematic uncertainties are reduced in the new results, and these improvements result

¹FONLL calculation can be directly obtained in the web.
<http://www.lpthe.jussieu.fr/~cacciari/fonll/fonllform.html>

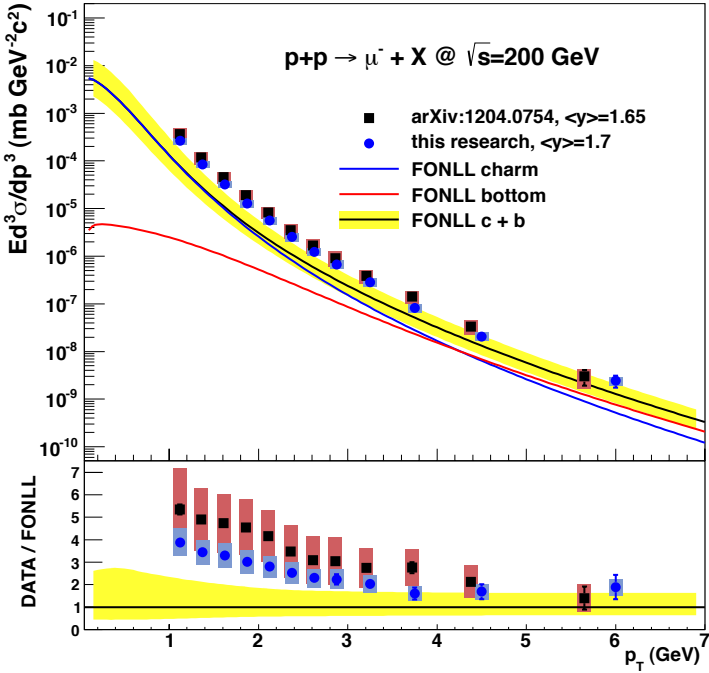


Figure 5.1: Invariant differential cross sections of heavy-flavor muons in $p+p$ collisions measured at forward rapidity. Black squares are the previous PHENIX results with the Run-5 data [53] and lines are from FONLL calculation [51, 52]. Lower panel shows ratios of data and FONLL calculation. Yellow bands represent upper and lower limits of the FONLL calculation.

from following factors.

- Enhanced statistics of data help to determine the hadronic background more precisely up to higher p_T
- Improvement of detailed analysis techniques to match the hadron cocktail simulation to the data

- Investigation into the propagation of uncertainties on the hadron cocktail simulation to the signal

In the comparison between the measured heavy-flavor muon spectra and the FONLL calculation, the data is a factor of $3 \sim 4$ larger than the central FONLL spectra at $\mathbf{p}_T < 3 \text{ GeV}/c$. The difference between the data and the central FONLL curve decrease to ~ 2 at $\mathbf{p}_T > 3 \text{ GeV}/c$, and the data is consistent with the FONLL calculation within uncertainties. Although the difference from the FONLL estimation is decreased in the new data, the data still lie clearly above the FONLL curve.

As discussed in [49] about the excess of data, it is interesting fact that the data becomes consistent with the FONLL curve within uncertainties when bottom contribution increases. This is probably related to uncertainties on both the data and the FONLL calculation.

- The theoretical estimation of bottom production is more precise than that of charm production due to larger mass of bottom. Especially at low \mathbf{p}_T region, $\mathbf{p}_T \lesssim \mathbf{m}_c$, the systematic uncertainty of FONLL calculation starts to increase.
- In the data analysis, the uncertainty is larger at low \mathbf{p}_T due to the smaller signal-to-background ratio and the inaccurate hadron shower simulation.

More discussions of comparison with the FONLL calculation can be found in [49].

5.2 Comparison of R_{dA} with the results at mid-rapidity

As introduced in Sec. 1.3.2, heavy-flavor electron production has been measured at mid-rapidity [59] with PHENIX central arm detectors. Figure 5.2 shows comparisons of $R_{dA}(p_T)$ in the most central and peripheral collisions, and Fig. 5.3 shows a comparison of $R_{dA}(\langle N_{coll} \rangle)$ for $1 < p_T < 3 \text{ GeV}/c$.

In the comparison of $R_{dA}(p_T)$, the mid-rapidity R_{dA} in the most peripheral collisions is consistent with the unity like the R_{dA} at backward and forward rapidity regions. In case of the most central collisions, the R_{dA} at mid-rapidity shows a similar enhancement with the R_{dA} at backward rapidity. According to the discussion in [59], the enhancement at mid-rapidity is thought to be attributed to p_T broadening from multiple scattering of initial partons. The enhancement observed in backward region at moderate p_T region is also probably due to the p_T broadening. In addition, a gluon anti-shadowing can explain such an enhancement. From PYTHIA [75] simulation, the momentum fraction of partons for $D \rightarrow \mu$ process at backward rapidity is $x_2 \approx 5.0 \times 10^{-2}$ which is in the anti-shadowing region based on R_g^{Pb} distribution of the EPS09s nPDF model shown in Fig. 1.15. Therefore the enhancement seen in backward rapidity is thought to be mainly contributed by the p_T broadening and the gluon anti-shadowing.

At forward rapidity, the p_T broadening is also seen from the shape of the most central $R_{dA}(p_T)$ shown in Fig. 5.2. However, heavy-flavor muon production is suppressed unlike backward and mid-rapidity regions. The momentum fraction of partons for $D \rightarrow \mu$ process at

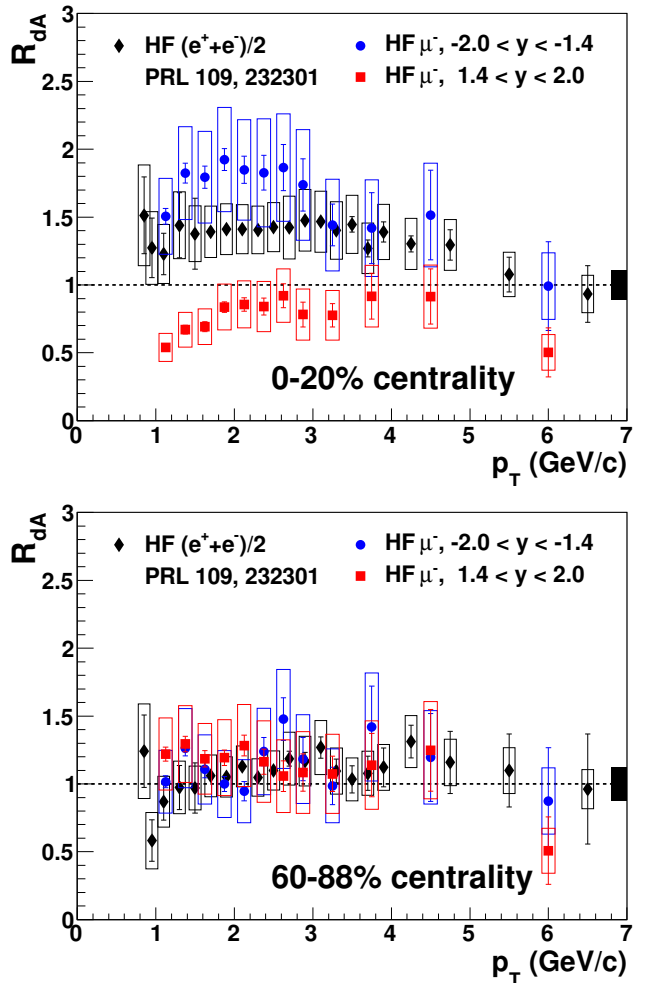


Figure 5.2: Comparison of R_{dA} as a function of p_T at different rapidity ranges in the most central (top) and most peripheral (bottom) $d+Au$ collisions.

forward rapidity from the PYTHIA simulation is $x_2 \approx 9.0 \times 10^{-3}$ which is in the shadowing region. The suppression may indicate that the main contributed CNM effect at forward region is the gluon shadowing. However it is hard to discriminate or quantify the contribution

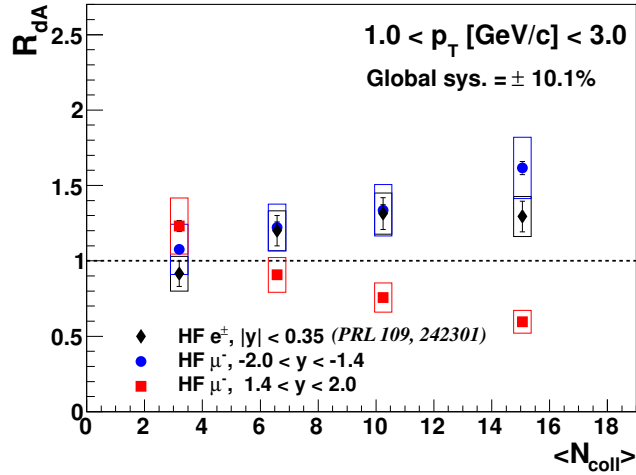


Figure 5.3: Comparison of R_{dA} as a function of $\langle N_{\text{coll}} \rangle$ at different rapidity ranges.

of each CNM effect and how they are competing solely with the data. In Sec. 5.3, further discussion with model predictions will be following.

Figure 5.3 shows $R_{dA}(\langle N_{\text{coll}} \rangle)$ with the results at mid-rapidity [59]. As shown in the comparison of $R_{dA}(p_T)$, the results at mid-rapidity agree with the backward R_{dA} , and the suppression is observed only at forward region. At all rapidity ranges, CNM effects clearly depend on the centrality which is directly related to the nuclear thickness or density.

5.3 R_{dA} compared to theoretical calculations

In this section, comparisons with theoretical model predictions will be discussed. Figure 5.4 shows comparisons of R_{dA} in unbias collisions with two model predictions. A black solid line on the upper panel is a prediction with pQCD calculation at forward rapidity considering CNM effects [58] such as shadowing, initial \mathbf{k}_T broadening, and energy loss in CNM. This pQCD prediction describes the data at forward rapidity pretty well. Interestingly, the same pQCD calculation including hot nuclear matter effects also succeeds to quantitatively predict the R_{AA} of heavy-flavor leptons in Cu+Cu (both forward and mid-rapidity) and Au+Au collisions (mid-rapidity) as mentioned in the introduction.

Another theoretical prediction shown in the lower panel is based on the EPS09s nPDF model [30]. This model provides the modification of partons' density inside the nucleus, and most recent model named EPS09s also considers spatial dependence. Based on this EPS09s nPDF set, one can calculate the magnitude of modification for an interested process by giving momentum fraction of partons (x), energy transfer (Q^2), and transverse distance from the center of nucleus (r_T). The calculation procedure is following.

- generate $D \rightarrow \mu$ process with the PYTHIA at forward and backward rapidity regions ($1.4 < \eta < 2.0$) and extract x_2 and Q^2
- select r_T from the r_T distribution corresponding to the PHENIX

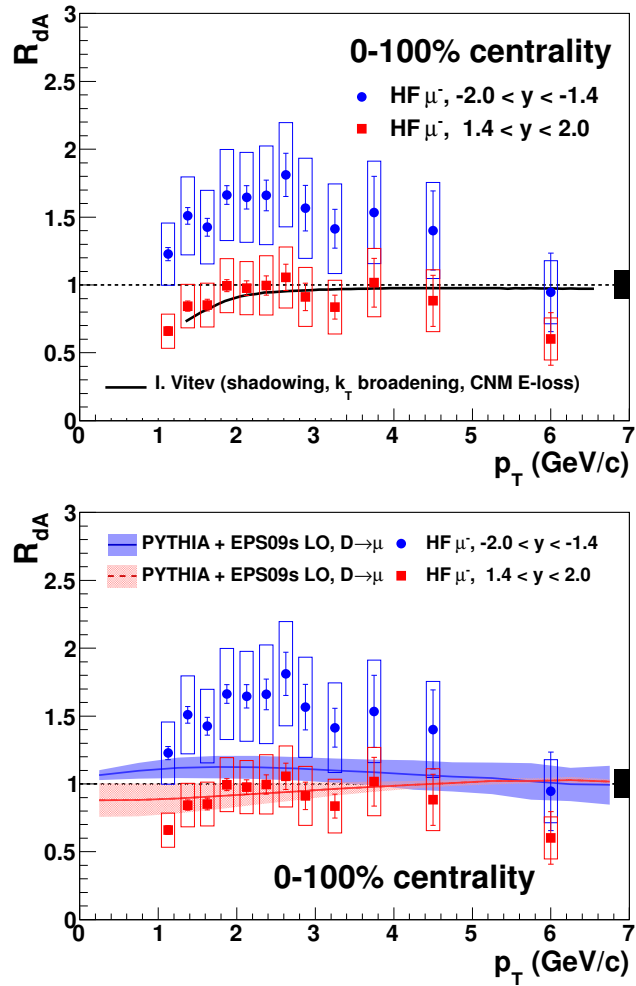


Figure 5.4: Comparison of R_{dA} to a prediction from pQCD [58] (top) and calculations based on EPS09s nPDF sets [30] (bottom) in 0–100% $d + \text{Au}$ collisions.

centrality determination for a certain centrality class

- calculate modification factors based on the EPS09s nPDF set with three input parameters, \mathbf{x}_2 , \mathbf{Q}^2 , and \mathbf{r}_T , obtained from the

above steps

PYTHIA generator used in this calculation is PYTHIA 8 [88], and just few parameters are changed in order to simulate the $D \rightarrow \mu$ process.

- $HardQCD:gg2ccbar = on$, $HardQCD:qqbar2ccbar = on$ to select hard processes
- $411:onMode = off$, $421:onMode = off$, and $431:onMode = off$ to turn off all decay modes of D^\pm , D^0 , and D_s^\pm
- $411:onIfAny = 13 -13$, $421:onIfAny = 13 -13$, and $431:onIfAny = 13 -13$ to turn on any decay modes including μ^\pm

This PYTHIA event generator only consider leading-order (LO) processes, so the EPS09s LO nPDF set is also used for consistency. Blue and red lines with bands on the lower panel and Fig. 5.5 represent the calculations based on the modification of parton distribution functions. The bands around lines are uncertainties determined based on [26].

In the 60–88% centrality class (lower panel in 5.5), the EPS09s nPDF based calculations are consistent with the data at both rapidity ranges. For the most central collisions (upper panel in 5.5), the model predictions show a good agreement with the forward data but underestimate the enhancement seen in the backward data. The disagreement at backward rapidity indicate another CNM effect, e.g. \mathbf{p}_T broadening, as discussed in the comparison to the mid-rapidity results. At forward rapidity, the EPS09s nPDF based calculation, considering only nPDF modification, well describe the $R_{dA}(\mathbf{p}_T)$ for different centrality classes. In addition, the pQCD calculation (black solid line on the upper panel

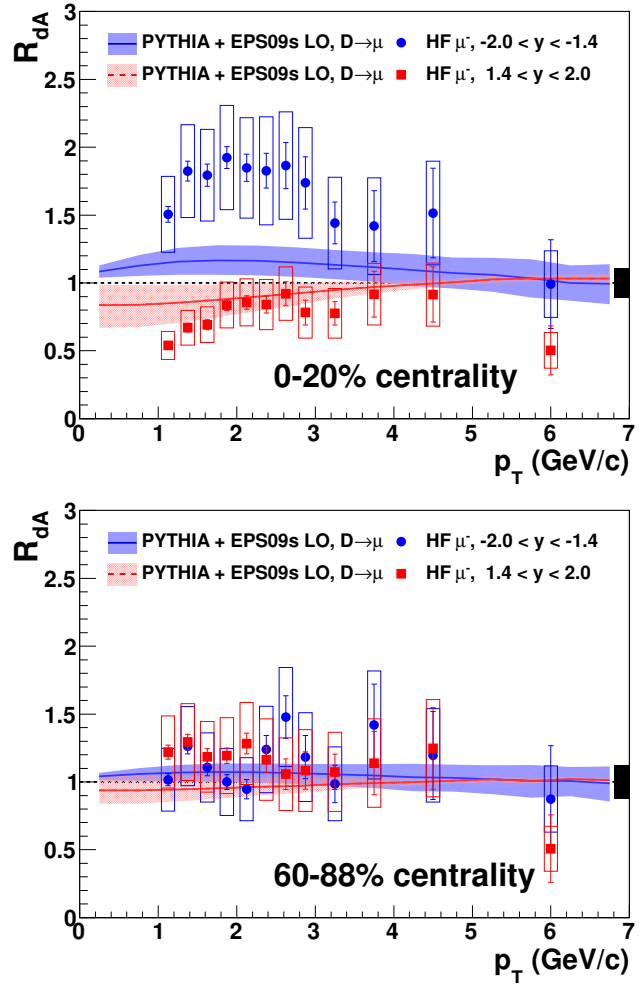


Figure 5.5: Comparison of R_{dA} to calculations based on EPS09s nPDF sets [30] in 0-20% (top) and 60-88% (bottom) $d+Au$ collisions.

of Fig. 5.4), additionally including p_T broadening and energy loss, also reproduce the data well. Therefore additional CNM effects can not be ruled out, and these CNM effects may compete each other so that both model calculations show good agreements with the data.

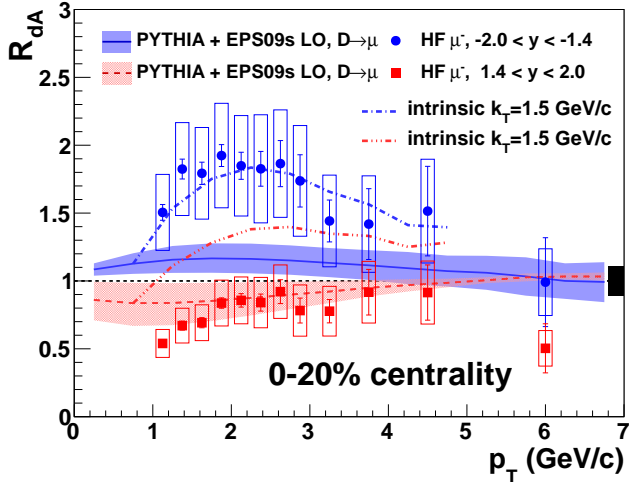


Figure 5.6: Comparison of R_{dA} for the 0–20% centrality class to the EPS09s nPDF sets [30] based calculation with additional intrinsic \mathbf{k}_T component.

Figure 5.6 contains additional two dot-dashed curves considering an initial \mathbf{k}_T component. Interestingly, the curves including two CNM effects (nPDF modification and Cronin effect) shows a very good agreement with the data at backward rapidity, whereas it overshoots the forward data. This is an exactly opposite trend against the trend shown in comparison to the original EPS09s nPDF calculation. For these comparisons, one can not find a proper combination of nPDFs and initial \mathbf{k}_T to reproduce the data at both rapidity ranges simultaneously. Not an additional CNM effect but a final-state interaction [38] may account for this larger \mathbf{p}_T broadening at backward rapidity where the multiplicity is almost twice larger than that in the forward region.

Figure 5.7 shows comparisons of $R_{dA}(\langle N_{coll} \rangle)$ with the EPS09s nPDF based on calculations. As discussed in the comparisons of $R_{dA}(\mathbf{p}_T)$,

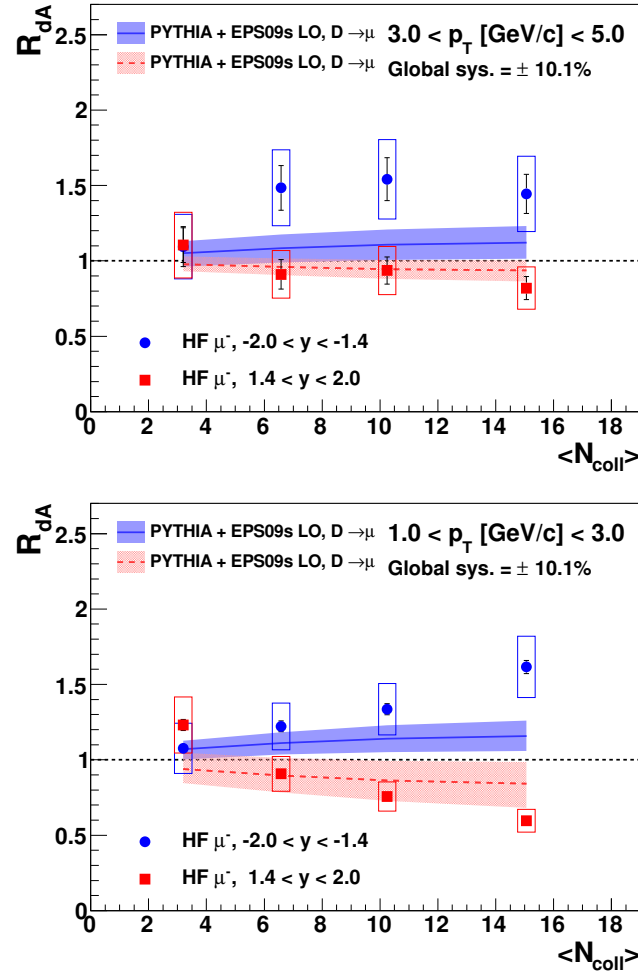


Figure 5.7: Comparison of R_{dA} as a function of $\langle N_{\text{coll}} \rangle$ to calculations based on EPS09s nPDF sets [30] for $1.0 < p_T [\text{GeV}/c] < 3.0$ (top) and $3.0 < p_T [\text{GeV}/c] < 5.0$ (bottom).

this model calculation successfully describes the centrality dependence at forward region. However, it underestimates the difference between forward and backward data. This fact may also suggest the role of

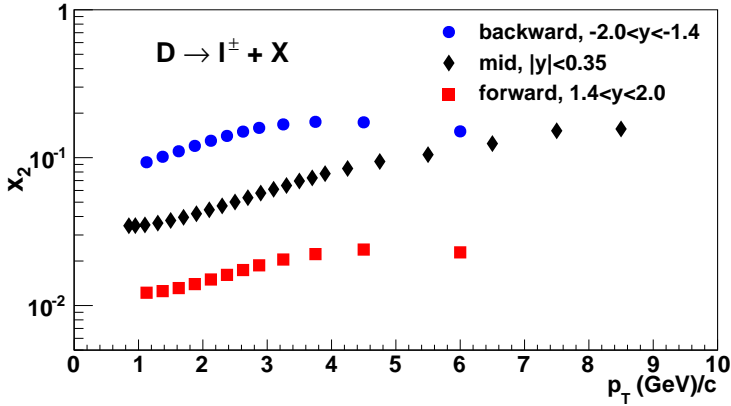


Figure 5.8: The momentum fraction x_2 of gluons in the Au nucleus for $D \rightarrow l^\pm + X$ processes.

other CNM effects besides the modification of nPDF.

As described above, the momentum fraction x of gluons in the Au nucleus can be extracted from the PYTHIA simulation. Figure 5.8 shows the momentum fraction x_2 distributions as a function of p_T for the $D \rightarrow l^\pm + X$ processes. We can access different momentum fraction of gluons depending on rapidity and p_T . Based on the relation, Fig. 5.5 can be re-plotted as a function of x_2 , the momentum fraction of gluons.

Figure 5.9 shows R_{dA} as function of x_2 for the most central (top) and peripheral (bottom) classes at different rapidity ranges. The lines with bands represent the PYTHIA plus EPS09s nPDF calculations. In order to make valid comparisons, only the data points at $p_T < 4 \text{ GeV}/c$, where D mesons are dominant, are used in the comparisons. As can be seen in the Fig. 5.9, the modification depending on x_2 observed in the data is stronger than the prediction from the EPS09s nPDF

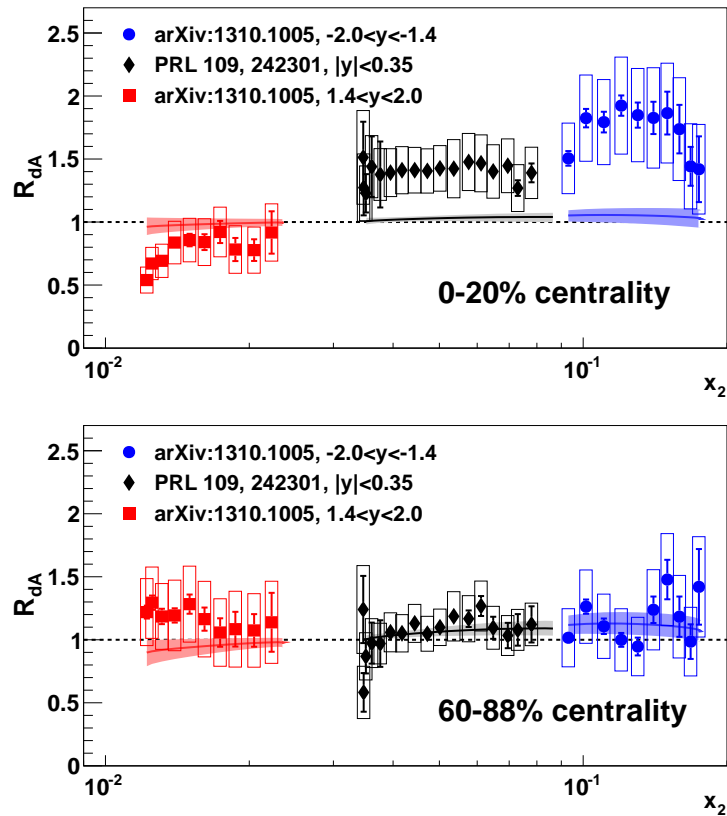


Figure 5.9: Comparison of R_{dA} as a function of x_2 to calculations based on EPS09s nPDF sets [30] in 0–20% (top) and 60–88% (bottom) d +Au collisions.

model.

5.4 Comparison of R_{dA} between heavy-flavor muon and J/ψ

The measurement of heavy quark production will shed light on the study of quarkonia production which are survived bound states of heavy quarks. As discussed in Sec. 1.2.3, one primary difference in the CNM effects on quarkonia production is the nuclear breakup. Figure 5.10 shows comparisons of R_{dA} between heavy-flavor muons measured in this research and J/ψ [37] at forward and backward rapidity regions. Previous study showed that charm contributions dominate over those from bottom at $p_T < 3 \text{ GeV}/c$ in the inclusive heavy-flavor production [89], so we could directly compare between D and J/ψ productions at this p_T range.

In the most peripheral collisions (bottom panel), R_{dA} of J/ψ and heavy-flavor muon are consistent with each other at both rapidity ranges. However in the most central collisions (top panel), only the forward R_{dA} shows an agreement within uncertainties. At backward rapidity, the R_{dA} of J/ψ is significantly smaller than the R_{dA} of heavy-flavor muon. These results indicate that J/ψ is largely affected by the nuclear breakup at backward rapidity where the Au nucleus is going. This different trend depending on rapidity was similarly observed in the $J/\psi R_{dA}$ as a function of rapidity [39]. Model calculations based on the EPS09 nPDF sets plus a fixed nuclear breakup cross section failed to reproduce the centrality and rapidity dependence of the $J/\psi R_{dA}$ simultaneously.

A similar trend is also observed in R_{dA} as a function $\langle N_{\text{coll}} \rangle$ as shown in Fig. 5.11 [42]. As shown in the figure, J/ψ production is suppressed

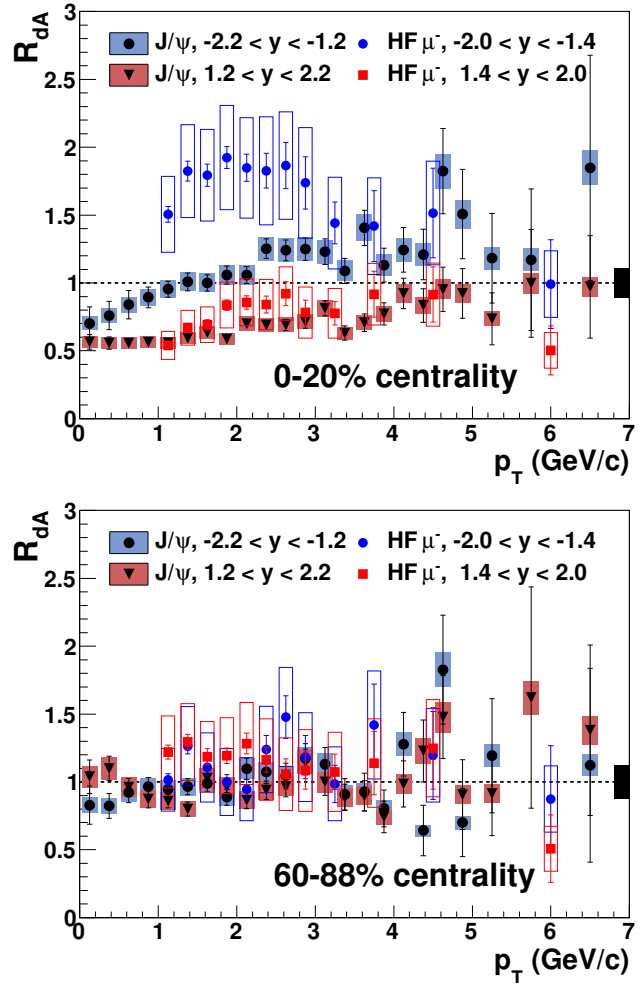


Figure 5.10: Comparison of R_{dA} between heavy-flavor muon and J/ψ [37] in 0–20% (top) and 60–88% (bottom) d +Au collisions.

at all rapidity ranges, as well as the magnitude of suppression increases as the $\langle N_{\text{coll}} \rangle$ becomes larger. Comparing to the heavy-flavor lepton results shown in Fig. 5.3, only the forward results follow the trend of $R_{dA}(\langle N_{\text{coll}} \rangle)$ in J/ψ .

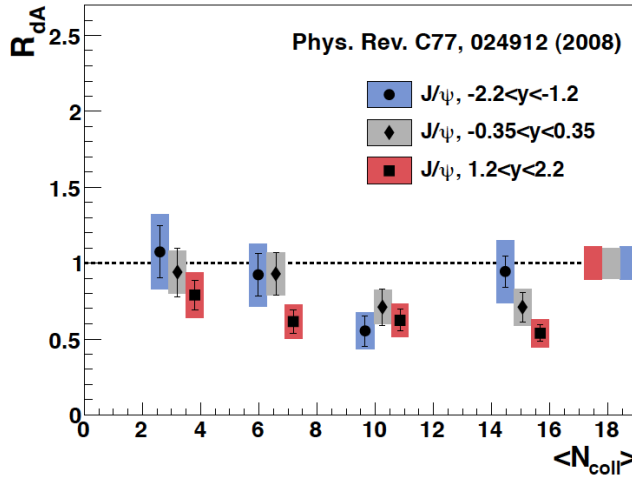


Figure 5.11: Nuclear modification factor R_{dA} of J/ψ as a function of $\langle N_{\text{coll}} \rangle$ at different rapidity ranges [42]. The backward (forward) data points are shifted to left (right) from the central point of $\langle N_{\text{coll}} \rangle$.

Global multiplicity measurements in d +Au collisions show that $dN_{\text{ch}}/d\eta$ in backward rapidity ($\eta \approx -2$) is almost twice larger than that in forward region ($\eta \approx 2$) [90]. The huge nuclear breakup at backward may be related to the dense co-moving particles. These results of open heavy-flavor productions at various rapidity ranges will be a key constraint to model calculations of J/ψ production.

Chapter 6

Conclusion and outlook

6.1 Conclusion

This dissertation represents the measurement of invariant yield of heavy-flavor muons in $p+p$ and different centrality classes of $d+\text{Au}$ collisions at $\sqrt{s_{NN}} = 200 \text{ GeV}$ as shown in Sec. 4.1. Based on these measurements, the nuclear modification factor R_{dA} as a function of p_T and $\langle N_{\text{coll}} \rangle$ is determined in order to quantify nuclear effects in $d+\text{Au}$ collisions as shown in Sec. 4.2 and 4.3. The results from this research were submitted to Phys. Rev. Lett. in Oct. 2013 [91].

Heavy-flavor muon production had been observed previously with the first $d+\text{Au}$ data taken in 2003. However, due to the lack of statistics, the measurement was limited only at $p_T < 3 \text{ GeV}/c$ for just minimum bias $d+\text{Au}$ collisions. During the second $d+\text{Au}$ run in 2008, PHENIX collected almost 40 times larger data than the first $d+\text{Au}$ run. Based on this high quality data, heavy-flavor muons have been

measured up to $p_T = 6 \text{ GeV}/c$ for different centrality classes.

The results in this research show:

- The \mathbf{R}_{dA} of heavy-flavor muons at both forward and backward rapidity ranges in 60–88% centrality of $d+\text{Au}$ collisions are consistent with the unity and each other. These results indicate that there is no overall modification due to CNM effects on heavy quark production in the peripheral $d+\text{Au}$ collisions.
- The \mathbf{R}_{dA} of heavy-flavor muons in 0–20% centrality of $d+\text{Au}$ collisions shows a clear enhancement at backward rapidity, whereas an overall suppression is observed at forward rapidity. The enhancement seen in the backward data is consistent with the \mathbf{R}_{dA} of heavy-flavor electrons at mid-rapidity [59].
- Theoretical predictions, pQCD including CNM effects and EPS09s nPDF based calculation, show agreements with the data at forward rapidity. However, the EPS09s nPDF based calculation, considering only nPDF modification, underestimates the difference between forward and backward rapidity ranges.
- Comparison to the J/ψ results provide an insight into the effect of the nuclear breakup at backward rapidity where many co-moving particles come out.

Based on the well developed data analysis procedure in the previous researches [53, 69], detailed techniques listed below have been improved in this research.

- Tuning of the hadron cocktail simulation has been improved by using response matrices to convert tuning parameters obtained from reconstructed \mathbf{p}_T into those for generated \mathbf{p}_T .
- A precise study to estimate the systematic uncertainty from the hadron cocktail simulation contributes to reduce the systematic uncertainties.
- Muons from \mathbf{J}/ψ mesons are subtracted from the signal, so the results are closer to muons from open heavy-flavor decay.

6.2 Outlook

Based on the development achieved so far, further data analyses are being performed with following data sets.

- Au+Au data in $\sqrt{s_{NN}} = 62$ and 39 GeV collected during the RHIC Run-10
- Cu+Au and $\mathbf{p}+\mathbf{p}$ data in $\sqrt{s_{NN}} = 200$ GeV collected during the RHIC Run-12

One promising aspect in the heavy-flavor muon analysis is that additional absorbers (~ 30 cm) were installed during the summer in 2010. Based on the simulation study with this additional absorber, punch-through hadrons are substantially reduced up to $\mathbf{p}_T \approx 5$ GeV/c, and the fraction of punch-through hadrons to the total hadronic background is less than 5% in low \mathbf{p}_T region. This will give us more precise background estimation and reduction of systematic uncertainty.

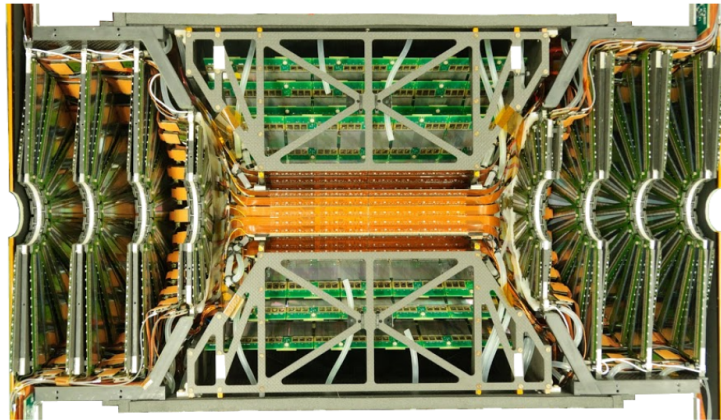


Figure 6.1: A cross-sectional view of the VTX barrels in the center and the two FVTX endcaps at both sides [92].

Another good news is that PHENIX collected very large amount of data during the RHIC Run-12 based on improved beam luminosities. The maximum p_T of heavy-flavor muon measurement is expected to be extended up to $\sim 10 \text{ GeV}/c$ where the bottom contribution is clearly more dominant than that of charm.

PHENIX have upgraded a silicon vertex tracking system in order to measure primary and second vertex positions precisely. Figure 6.1 shows a cross-sectional view of the silicon vertex tracking system consisting of the VTX [93] in the center and the FVTX [92] at forward and backward 4sides. Both detectors were installed and their commissioning was successfully done during the recent RHIC runs. Two systems are expected to provide $\sim 100 \mu\text{m}$ of spatial resolution. Based on the high precision of vertex measurement, leptons from **D** ($c\tau \approx 300 \mu\text{m}$) and **B** ($c\tau \approx 500 \mu\text{m}$) mesons can be separated. This is the primary physics goal of the silicon vertex tracking system.

According to the PHENIX beam use proposal [94], RHIC runs in upcoming two years will be dedicated to the heavy-flavor physics. Au+Au and (p +Au) run is scheduled in the RHIC Run-14 (Run-15), and many interesting new results will come out with the data. Based on the D/B separation, we can figure out the mass dependent modification of heavy quarks in the hot or cold nuclear matters.

Appendix A

Additional plots

A.1 R_{NS}

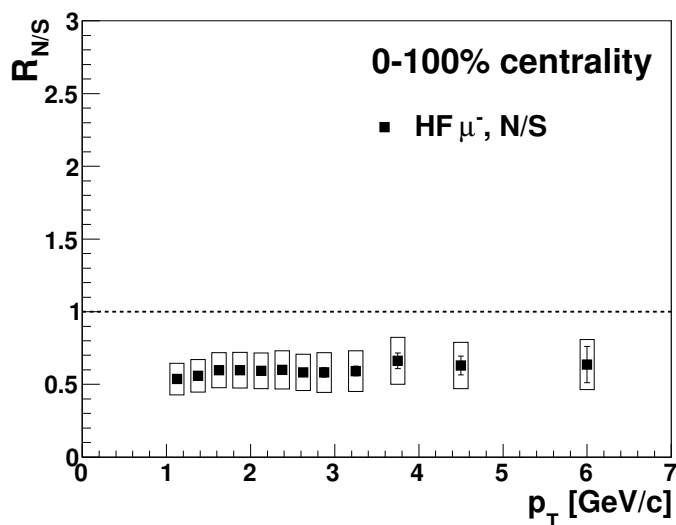


Figure A.1: Invariant yield ratio between forward (North) and backward (South) in 0–100% centrality d +Au collisions.

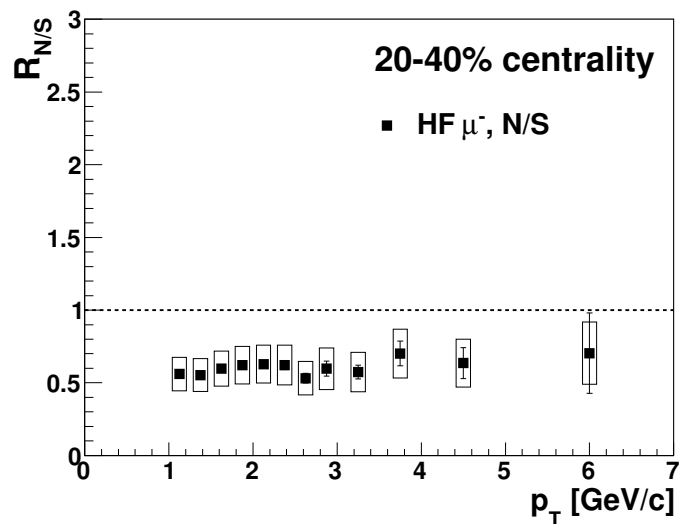
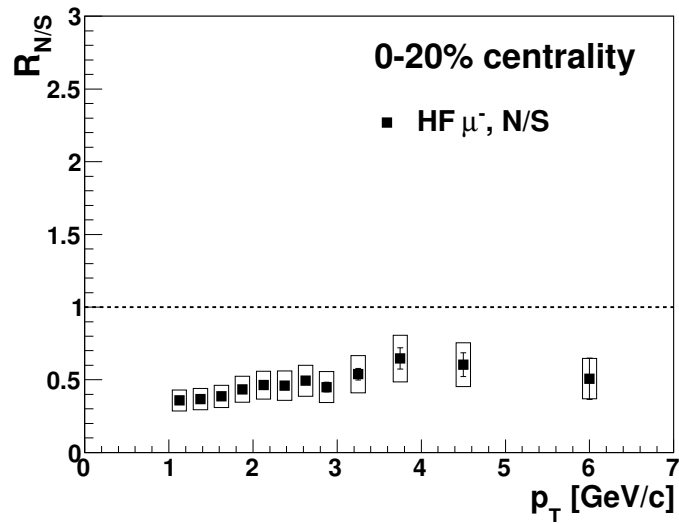


Figure A.3: Invariant yield ratio between forward (North) and backward (South) in 20–40% centrality d +Au collisions.

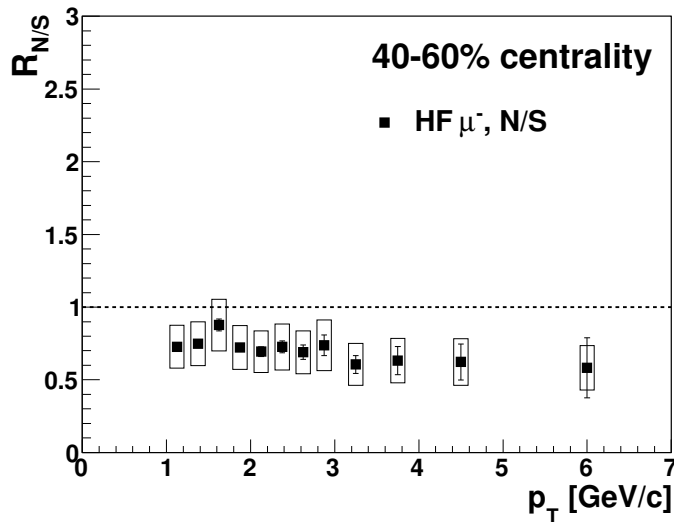


Figure A.4: Invariant yield ratio between forward (North) and backward (South) in 40–60% centrality d +Au collisions.

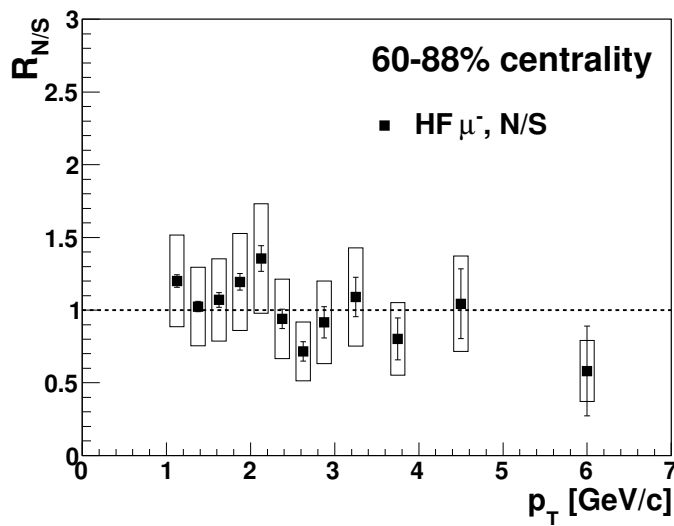


Figure A.5: Invariant yield ratio between forward (North) and backward (South) in 60–88% centrality d +Au collisions.

A.2 R_{CP}

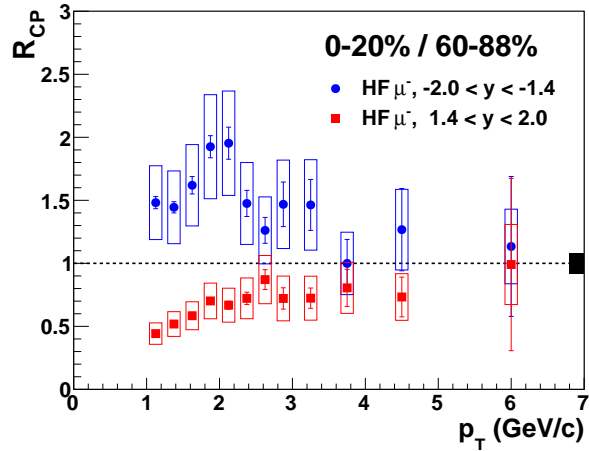


Figure A.6: The nuclear modification factor R_{CP} for 0–20% centrality d +Au collisions.

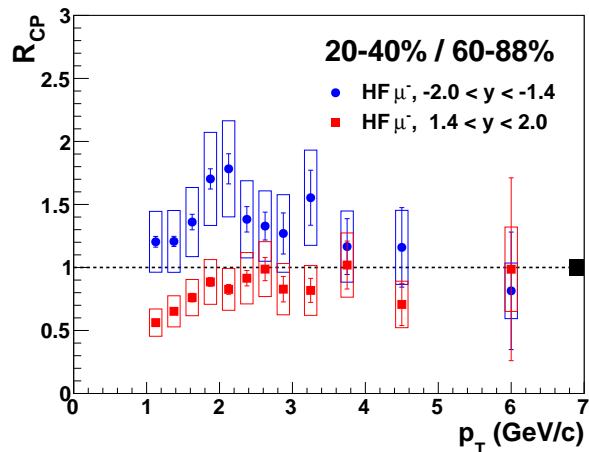


Figure A.7: The nuclear modification factor R_{CP} for 20–40% centrality d +Au collisions.

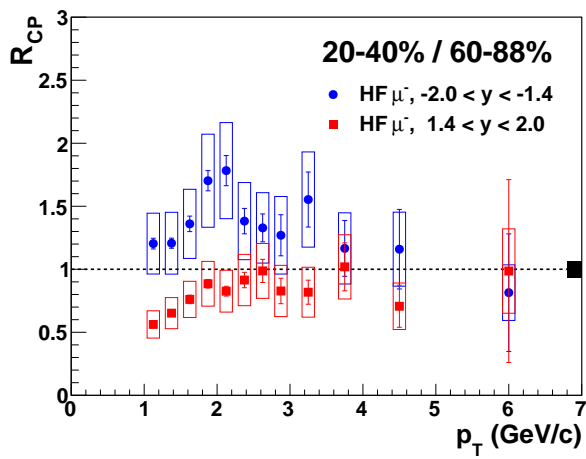


Figure A.8: The nuclear modification factor R_{CP} for 40–60% centrality d +Au collisions.

A.3 R_{dA} of heavy-flavor lepton and J/ψ

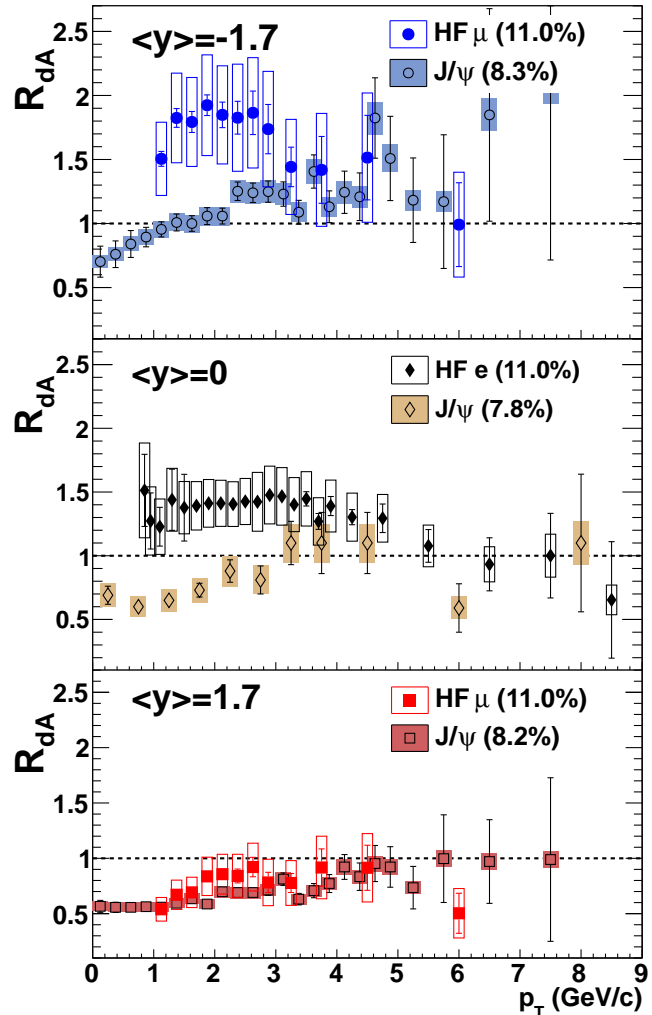


Figure A.9: Comparison of R_{dA} between heavy-flavor lepton and J/ψ at different rapidity ranges.

Appendix B

Data table

Table B.1: Heavy-flavor muon double differential cross section in $p+p$ collisions at $1.4 < |y| < 2.0$.

| p_T | Ed^3p/dp^3 | stat. uncertainty | sys. uncertainty |
|-------|--------------|-------------------|------------------|
| 1.125 | 2.64e-04 | 9.06e-06 | 4.20e-05 |
| 1.375 | 8.38e-05 | 3.08e-06 | 1.35e-05 |
| 1.625 | 3.18e-05 | 1.32e-07 | 5.15e-05 |
| 1.875 | 1.27e-05 | 4.92e-07 | 2.18e-06 |
| 2.215 | 5.61e-06 | 2.77e-07 | 9.59e-07 |
| 2.375 | 2.55e-06 | 1.64e-07 | 4.72e-07 |
| 2.625 | 1.24e-06 | 1.04e-07 | 2.23e-07 |
| 2.875 | 6.69e-07 | 6.81e-08 | 1.32e-07 |
| 3.250 | 2.83e-07 | 2.71e-08 | 5.46e-08 |
| 3.750 | 8.22e-08 | 1.36e-08 | 1.68e-08 |
| 4.500 | 2.05e-08 | 4.06e-09 | 4.26e-09 |
| 6.000 | 2.43e-09 | 6.89e-10 | 4.69e-10 |

Table B.2: Heavy flavor-muon invariant yield in 0–100% d +Au collisions at backward (South, $-2.0 < y < -1.4$) and forward (Nouth, $1.4 < y < 2.0$) rapidity.

| rapidity | p_T | $1/2\pi p_T d^2N/dp_T dy$ | stat. error | sys. error. |
|----------|-------|---------------------------|-------------|-------------|
| S | 1.125 | 5.85564e-05 | 1.15771e-06 | 8.25817e-06 |
| S | 1.375 | 2.28476e-05 | 3.84915e-07 | 3.25932e-06 |
| S | 1.625 | 8.20331e-06 | 1.66305e-07 | 1.16945e-06 |
| S | 1.875 | 3.82836e-06 | 5.84956e-08 | 5.60852e-07 |
| S | 2.125 | 1.66737e-06 | 3.16874e-08 | 2.44351e-07 |
| S | 2.375 | 7.64873e-07 | 1.83467e-08 | 1.18019e-07 |
| S | 2.625 | 4.05252e-07 | 1.13032e-08 | 6.09591e-08 |
| S | 2.875 | 1.89377e-07 | 7.36818e-09 | 3.09167e-08 |
| S | 3.250 | 7.22965e-08 | 2.86692e-09 | 1.19075e-08 |
| S | 3.750 | 2.27985e-08 | 1.42653e-09 | 3.88756e-09 |
| S | 4.500 | 5.18719e-09 | 4.15143e-10 | 9.07761e-10 |
| S | 6.000 | 4.15544e-10 | 6.37085e-11 | 7.58652e-11 |
| N | 1.125 | 3.14489e-05 | 1.1017e-06 | 4.53737e-06 |
| N | 1.375 | 1.27794e-05 | 3.54128e-07 | 1.8029e-06 |
| N | 1.625 | 4.90297e-06 | 1.43719e-07 | 6.90111e-07 |
| N | 1.875 | 2.28947e-06 | 4.95782e-08 | 3.32375e-07 |
| N | 2.125 | 9.8874e-07 | 2.62532e-08 | 1.44119e-07 |
| N | 2.375 | 4.58891e-07 | 1.53933e-08 | 7.11785e-08 |
| N | 2.625 | 2.36166e-07 | 9.33461e-09 | 3.5822e-08 |
| N | 2.875 | 1.1024e-07 | 6.02676e-09 | 1.84627e-08 |
| N | 3.250 | 4.28042e-08 | 2.33086e-09 | 7.26925e-09 |
| N | 3.750 | 1.51117e-08 | 1.19553e-09 | 2.60917e-09 |
| N | 4.500 | 3.27017e-09 | 3.45911e-10 | 5.99151e-10 |
| N | 6.000 | 2.64546e-10 | 5.7876e-11 | 5.22727e-11 |

Table B.3: Heavy flavor-muon invariant yield in 0–20% d +Au collisions at backward (South, $-2.0 < y < -1.4$) and forward (Nouth, $1.4 < y < 2.0$) rapidity.

| rapidity | p_T | $1/2\pi p_T d^2N/dp_T dy$ | stat. error | sys. error. |
|----------|-------|---------------------------|-------------|-------------|
| S | 1.125 | 0.0001425 | 2.50827e-06 | 1.99238e-05 |
| S | 1.375 | 5.48111e-05 | 8.934e-07 | 7.64606e-06 |
| S | 1.625 | 2.04746e-05 | 3.99783e-07 | 2.85906e-06 |
| S | 1.875 | 8.78952e-06 | 1.49125e-07 | 1.27104e-06 |
| S | 2.125 | 3.71656e-06 | 8.45344e-08 | 5.38384e-07 |
| S | 2.375 | 1.66985e-06 | 5.12055e-08 | 2.56021e-07 |
| S | 2.625 | 8.27778e-07 | 3.23575e-08 | 1.24852e-07 |
| S | 2.875 | 4.16982e-07 | 2.14231e-08 | 6.75522e-08 |
| S | 3.250 | 1.46286e-07 | 8.35686e-09 | 2.43859e-08 |
| S | 3.750 | 4.18405e-08 | 4.29287e-09 | 7.39828e-09 |
| S | 4.500 | 1.11295e-08 | 1.268e-09 | 1.94945e-09 |
| S | 6.000 | 8.64418e-10 | 1.94654e-10 | 1.60586e-10 |
| N | 1.125 | 5.10828e-05 | 1.99114e-06 | 7.46956e-06 |
| N | 1.375 | 2.01546e-05 | 6.73908e-07 | 2.89776e-06 |
| N | 1.625 | 7.9045e-06 | 2.79881e-07 | 1.12852e-06 |
| N | 1.875 | 3.82454e-06 | 9.93572e-08 | 5.61763e-07 |
| N | 2.125 | 1.72278e-06 | 5.51845e-08 | 2.52457e-07 |
| N | 2.375 | 7.68564e-07 | 3.29704e-08 | 1.20829e-07 |
| N | 2.625 | 4.08919e-07 | 2.0662e-08 | 6.25645e-08 |
| N | 2.875 | 1.87682e-07 | 1.35011e-08 | 3.21817e-08 |
| N | 3.250 | 7.88383e-08 | 5.31613e-09 | 1.32883e-08 |
| N | 3.750 | 2.7043e-08 | 2.67849e-09 | 4.67492e-09 |
| N | 4.500 | 6.72032e-09 | 8.67691e-10 | 1.1914e-09 |
| N | 6.000 | 4.39216e-10 | 1.39246e-10 | 8.85173e-11 |

Table B.4: Heavy flavor-muon invariant yield in 20–40% d +Au collisions at backward (South, $-2.0 < y < -1.4$) and forward (Nouth, $1.4 < y < 2.0$) rapidity.

| rapidity | p_T | $1/2\pi p_T d^2N/dp_T dy$ | stat. error | sys. error. |
|----------|-------|---------------------------|-------------|-------------|
| S | 1.125 | 7.87833e-05 | 1.77588e-06 | 1.1328e-05 |
| S | 1.375 | 3.11564e-05 | 6.36786e-07 | 4.50221e-06 |
| S | 1.625 | 1.1703e-05 | 2.89775e-07 | 1.67385e-06 |
| S | 1.875 | 5.28896e-06 | 1.10252e-07 | 7.84392e-07 |
| S | 2.125 | 2.30829e-06 | 6.43388e-08 | 3.40395e-07 |
| S | 2.375 | 1.06457e-06 | 3.88081e-08 | 1.64688e-07 |
| S | 2.625 | 5.93122e-07 | 2.52695e-08 | 8.92132e-08 |
| S | 2.875 | 2.45373e-07 | 1.6632e-08 | 4.09918e-08 |
| S | 3.250 | 1.05653e-07 | 6.64511e-09 | 1.73069e-08 |
| S | 3.750 | 3.32096e-08 | 3.3888e-09 | 5.60431e-09 |
| S | 4.500 | 6.92887e-09 | 9.96432e-10 | 1.22259e-09 |
| S | 6.000 | 4.22601e-10 | 1.57461e-10 | 8.41146e-11 |
| N | 1.125 | 4.41814e-05 | 1.58397e-06 | 6.48953e-06 |
| N | 1.375 | 1.72475e-05 | 5.28496e-07 | 2.4794e-06 |
| N | 1.625 | 7.00586e-06 | 2.22086e-07 | 9.91077e-07 |
| N | 1.875 | 3.28328e-06 | 8.13347e-08 | 4.78065e-07 |
| N | 2.125 | 1.45008e-06 | 4.57309e-08 | 2.10981e-07 |
| N | 2.375 | 6.62288e-07 | 2.76857e-08 | 1.03053e-07 |
| N | 2.625 | 3.15347e-07 | 1.72927e-08 | 4.86715e-08 |
| N | 2.875 | 1.46579e-07 | 1.16094e-08 | 2.50406e-08 |
| N | 3.250 | 6.06536e-08 | 4.59532e-09 | 1.03001e-08 |
| N | 3.750 | 2.32846e-08 | 2.47852e-09 | 3.9738e-09 |
| N | 4.500 | 4.40867e-09 | 7.12463e-10 | 8.34314e-10 |
| N | 6.000 | 2.97442e-10 | 1.20948e-10 | 6.84856e-11 |

Table B.5: Heavy flavor-muon invariant yield in 40–60% d +Au collisions at backward (South, $-2.0 < y < -1.4$) and forward (Nouth, $1.4 < y < 2.0$) rapidity.

| rapidity | p_T | $1/2\pi p_T d^2N/dp_T dy$ | stat. error | sys. error. |
|----------|-------|---------------------------|-------------|-------------|
| S | 1.125 | 4.76839e-05 | 1.19829e-06 | 6.7301e-06 |
| S | 1.375 | 1.78767e-05 | 4.40746e-07 | 2.58897e-06 |
| S | 1.625 | 5.8563e-06 | 2.08583e-07 | 8.53649e-07 |
| S | 1.875 | 3.0216e-06 | 8.12674e-08 | 4.48807e-07 |
| S | 2.125 | 1.40565e-06 | 4.74147e-08 | 2.06443e-07 |
| S | 2.375 | 6.62569e-07 | 2.91041e-08 | 1.01766e-07 |
| S | 2.625 | 3.57336e-07 | 1.92998e-08 | 5.37999e-08 |
| S | 2.875 | 1.5176e-07 | 1.25614e-08 | 2.50575e-08 |
| S | 3.250 | 6.35802e-08 | 5.08395e-09 | 1.0429e-08 |
| S | 3.750 | 2.16067e-08 | 2.6384e-09 | 3.59425e-09 |
| S | 4.500 | 4.61152e-09 | 7.78361e-10 | 7.98378e-10 |
| S | 6.000 | 4.79597e-10 | 1.38627e-10 | 8.1543e-11 |
| N | 1.125 | 3.46761e-05 | 1.16105e-06 | 5.01982e-06 |
| N | 1.375 | 1.33877e-05 | 3.8972e-07 | 1.87965e-06 |
| N | 1.625 | 5.13446e-06 | 1.65526e-07 | 7.19571e-07 |
| N | 1.875 | 2.18268e-06 | 6.27096e-08 | 3.18109e-07 |
| N | 2.125 | 9.75049e-07 | 3.57627e-08 | 1.42207e-07 |
| N | 2.375 | 4.81011e-07 | 2.14749e-08 | 7.46127e-08 |
| N | 2.625 | 2.46561e-07 | 1.38625e-08 | 3.74184e-08 |
| N | 2.875 | 1.11929e-07 | 9.22904e-09 | 1.87074e-08 |
| N | 3.250 | 3.8516e-08 | 3.61992e-09 | 6.63812e-09 |
| N | 3.750 | 1.36515e-08 | 1.97016e-09 | 2.39609e-09 |
| N | 4.500 | 2.87267e-09 | 5.57628e-10 | 5.47767e-10 |
| N | 6.000 | 2.79348e-10 | 1.03577e-10 | 5.55134e-11 |

Table B.6: Heavy flavor-muon invariant yield in 60–88% d +Au collisions at backward (South, $-2.0 < y < -1.4$) and forward (Nouth, $1.4 < y < 2.0$) rapidity.

| rapidity | p_T | $1/2\pi p_T d^2N/dp_T dy$ | stat. error | sys. error. |
|----------|-------|---------------------------|-------------|-------------|
| S | 1.125 | 2.04245e-05 | 5.57111e-07 | 3.89991e-06 |
| S | 1.375 | 8.05659e-06 | 2.10763e-07 | 1.55748e-06 |
| S | 1.625 | 2.68453e-06 | 1.01559e-07 | 5.17221e-07 |
| S | 1.875 | 9.69333e-07 | 4.09775e-08 | 1.98598e-07 |
| S | 2.125 | 4.04049e-07 | 2.46467e-08 | 8.17191e-08 |
| S | 2.375 | 2.40364e-07 | 1.51879e-08 | 4.9275e-08 |
| S | 2.625 | 1.39322e-07 | 9.96853e-09 | 2.73372e-08 |
| S | 2.875 | 6.03014e-08 | 6.57308e-09 | 1.3176e-08 |
| S | 3.250 | 2.12247e-08 | 2.66847e-09 | 4.70983e-09 |
| S | 3.750 | 8.89030e-09 | 1.42511e-09 | 1.92949e-09 |
| S | 4.500 | 1.8649e-09 | 4.30911e-10 | 4.16945e-10 |
| S | 6.000 | 1.61894e-10 | 7.03612e-11 | 3.64032e-11 |
| N | 1.125 | 2.45185e-05 | 5.9497e-07 | 4.41471e-06 |
| N | 1.375 | 8.25563e-06 | 1.99489e-07 | 1.47916e-06 |
| N | 1.625 | 2.87327e-06 | 8.95294e-08 | 5.18584e-07 |
| N | 1.875 | 1.15749e-06 | 3.39835e-08 | 2.19479e-07 |
| N | 2.125 | 5.47646e-07 | 1.91719e-08 | 1.04096e-07 |
| N | 2.375 | 2.25959e-07 | 1.17768e-08 | 4.64882e-08 |
| N | 2.625 | 9.96989e-08 | 7.47995e-09 | 2.03789e-08 |
| N | 2.875 | 5.52528e-08 | 5.12758e-09 | 1.21195e-08 |
| N | 3.250 | 2.31372e-08 | 2.04976e-09 | 4.99698e-09 |
| N | 3.750 | 7.12927e-09 | 1.09177e-09 | 1.59946e-09 |
| N | 4.500 | 1.94703e-09 | 3.35261e-10 | 4.32415e-10 |
| N | 6.000 | 9.41391e-11 | 5.77074e-11 | 2.64966e-11 |

Table B.7: Heavy flavor-muon R_{dA} in 0–100% d +Au collisions at backward (South, $-2.0 < y < -1.4$) and forward (Nouth, $1.4 < y < 2.0$) rapidity. Global uncertainty 10.4% is not included.

| rapidity | p_T | R_{dA} | stat. error | sys. error. |
|----------|-------|----------|-------------|-------------|
| S | 1.125 | 1.22722 | 0.0485808 | 0.229366 |
| S | 1.375 | 1.50905 | 0.0608238 | 0.286656 |
| S | 1.625 | 1.42552 | 0.0656092 | 0.271463 |
| S | 1.875 | 1.66276 | 0.0686749 | 0.334925 |
| S | 2.125 | 1.64555 | 0.0865221 | 0.331397 |
| S | 2.375 | 1.65984 | 0.112818 | 0.363098 |
| S | 2.625 | 1.81125 | 0.158695 | 0.384111 |
| S | 2.875 | 1.56555 | 0.167536 | 0.36888 |
| S | 3.250 | 1.41405 | 0.14341 | 0.329274 |
| S | 3.750 | 1.53419 | 0.265131 | 0.377626 |
| S | 4.500 | 1.40072 | 0.291679 | 0.353309 |
| S | 6.000 | 0.945383 | 0.290077 | 0.232168 |
| N | 1.125 | 0.659105 | 0.0322648 | 0.124809 |
| N | 1.375 | 0.844061 | 0.0386078 | 0.159339 |
| N | 1.625 | 0.85201 | 0.0429636 | 0.161101 |
| N | 1.875 | 0.994379 | 0.0434925 | 0.199339 |
| N | 2.125 | 0.975799 | 0.0540043 | 0.195957 |
| N | 2.375 | 0.995834 | 0.0706888 | 0.218414 |
| N | 2.625 | 1.05552 | 0.0961878 | 0.22479 |
| N | 2.875 | 0.911338 | 0.101481 | 0.217416 |
| N | 3.250 | 0.837212 | 0.0883599 | 0.198007 |
| N | 3.750 | 1.01692 | 0.179879 | 0.251818 |
| N | 4.500 | 0.883059 | 0.188925 | 0.227831 |
| N | 6.000 | 0.601856 | 0.194292 | 0.154645 |

Table B.8: Heavy flavor-muon \mathbf{R}_{dA} in 0–20% d +Au collisions at backward (South, $-2.0 < y < -1.4$) and forward (Nouth, $1.4 < y < 2.0$) rapidity. Global uncertainty 11.0% is not included.

| rapidity | \mathbf{p}_T | \mathbf{R}_{dA} | stat. error | sys. error. |
|----------|----------------|-------------------|-------------|-------------|
| S | 1.125 | 1.50505 | 0.0580309 | 0.279917 |
| S | 1.375 | 1.82439 | 0.073155 | 0.342255 |
| S | 1.625 | 1.79303 | 0.0820153 | 0.337548 |
| S | 1.875 | 1.92385 | 0.0806596 | 0.384877 |
| S | 2.125 | 1.84845 | 0.0997342 | 0.369996 |
| S | 2.375 | 1.82618 | 0.128116 | 0.398226 |
| S | 2.625 | 1.86446 | 0.169869 | 0.395934 |
| S | 2.875 | 1.73719 | 0.192534 | 0.407817 |
| S | 3.250 | 1.44191 | 0.154265 | 0.337803 |
| S | 3.750 | 1.41892 | 0.260937 | 0.355508 |
| S | 4.500 | 1.51455 | 0.329885 | 0.382188 |
| S | 6.000 | 0.991064 | 0.32744 | 0.245757 |
| N | 1.125 | 0.539525 | 0.0279606 | 0.102968 |
| N | 1.375 | 0.670848 | 0.0330657 | 0.127999 |
| N | 1.625 | 0.692226 | 0.0373826 | 0.13193 |
| N | 1.875 | 0.837114 | 0.0383232 | 0.168851 |
| N | 2.125 | 0.856834 | 0.0495966 | 0.172553 |
| N | 2.375 | 0.840515 | 0.0627771 | 0.185603 |
| N | 2.625 | 0.921036 | 0.0878861 | 0.197015 |
| N | 2.875 | 0.781902 | 0.0917625 | 0.188741 |
| N | 3.250 | 0.777094 | 0.0859809 | 0.18308 |
| N | 3.750 | 0.917098 | 0.168074 | 0.227235 |
| N | 4.500 | 0.914528 | 0.203528 | 0.232128 |
| N | 6.000 | 0.503566 | 0.180839 | 0.130923 |

Table B.9: Heavy flavor-muon R_{dA} in 20–40% d +Au collisions at backward (South, $-2.0 < y < -1.4$) and forward (Nouth, $1.4 < y < 2.0$) rapidity. Global uncertainty 10.7% is not included.

| rapidity | p_T | R_{dA} | stat. error | sys. error. |
|----------|-------|----------|-------------|-------------|
| S | 1.125 | 1.22289 | 0.0501773 | 0.23111 |
| S | 1.375 | 1.5241 | 0.0638579 | 0.291636 |
| S | 1.625 | 1.50621 | 0.0724621 | 0.287358 |
| S | 1.875 | 1.70134 | 0.0739602 | 0.344938 |
| S | 2.125 | 1.68722 | 0.0945801 | 0.340918 |
| S | 2.375 | 1.71102 | 0.123847 | 0.374776 |
| S | 2.625 | 1.96335 | 0.181772 | 0.416355 |
| S | 2.875 | 1.50235 | 0.175428 | 0.357971 |
| S | 3.250 | 1.5305 | 0.168024 | 0.355421 |
| S | 3.750 | 1.65516 | 0.307104 | 0.405386 |
| S | 4.500 | 1.38575 | 0.318049 | 0.350927 |
| S | 6.000 | 0.712072 | 0.286119 | 0.183758 |
| N | 1.125 | 0.685791 | 0.0339761 | 0.131229 |
| N | 1.375 | 0.843709 | 0.0400933 | 0.160967 |
| N | 1.625 | 0.901673 | 0.0467109 | 0.170969 |
| N | 1.875 | 1.05616 | 0.047767 | 0.212052 |
| N | 2.125 | 1.05992 | 0.0611642 | 0.212647 |
| N | 2.375 | 1.06445 | 0.0792206 | 0.233835 |
| N | 2.625 | 1.04386 | 0.101516 | 0.224293 |
| N | 2.875 | 0.897461 | 0.108239 | 0.21623 |
| N | 3.250 | 0.878633 | 0.1003 | 0.207799 |
| N | 3.750 | 1.1605 | 0.216516 | 0.285762 |
| N | 4.500 | 0.881718 | 0.20479 | 0.231289 |
| N | 6.000 | 0.501182 | 0.195929 | 0.14175 |

Table B.10: Heavy flavor-muon R_{dA} in 40–60% d +Au collisions at backward (South, $-2.0 < y < -1.4$) and forward (Nouth, $1.4 < y < 2.0$) rapidity. Global uncertainty 11.1% is not included.

| rapidity | p_T | R_{dA} | stat. error | sys. error. |
|----------|-------|----------|-------------|-------------|
| S | 1.125 | 1.15293 | 0.0489963 | 0.215577 |
| S | 1.375 | 1.36217 | 0.0599837 | 0.260982 |
| S | 1.625 | 1.17406 | 0.0635807 | 0.22641 |
| S | 1.875 | 1.51404 | 0.0701466 | 0.307214 |
| S | 2.125 | 1.60043 | 0.0942284 | 0.322682 |
| S | 2.375 | 1.65879 | 0.125448 | 0.362043 |
| S | 2.625 | 1.84251 | 0.179551 | 0.39092 |
| S | 2.875 | 1.44738 | 0.178477 | 0.342903 |
| S | 3.250 | 1.43467 | 0.168208 | 0.333391 |
| S | 3.750 | 1.67742 | 0.325305 | 0.408068 |
| S | 4.500 | 1.43663 | 0.345494 | 0.360504 |
| S | 6.000 | 1.25878 | 0.465929 | 0.29758 |
| N | 1.125 | 0.838419 | 0.0401368 | 0.159075 |
| N | 1.375 | 1.02012 | 0.0475133 | 0.192059 |
| N | 1.625 | 1.02935 | 0.0536311 | 0.194167 |
| N | 1.875 | 1.09368 | 0.051584 | 0.219694 |
| N | 2.125 | 1.11016 | 0.0668415 | 0.223009 |
| N | 2.375 | 1.20424 | 0.0911031 | 0.264129 |
| N | 2.625 | 1.27133 | 0.124698 | 0.270821 |
| N | 2.875 | 1.0675 | 0.130827 | 0.254415 |
| N | 3.250 | 0.869104 | 0.106235 | 0.207129 |
| N | 3.750 | 1.05983 | 0.212875 | 0.264565 |
| N | 4.500 | 0.894925 | 0.219583 | 0.235684 |
| N | 6.000 | 0.733193 | 0.283512 | 0.189031 |

Table B.11: Heavy flavor-muon \mathbf{R}_{dA} in 60–88% d +Au collisions at backward (South, $-2.0 < y < -1.4$) and forward (Nouth, $1.4 < y < 2.0$) rapidity. Global uncertainty 12.4% is not included.

| rapidity | \mathbf{p}_T | \mathbf{R}_{dA} | stat. error | sys. error. |
|----------|----------------|-------------------|-------------|-------------|
| S | 1.125 | 1.01593 | 0.0444864 | 0.230554 |
| S | 1.375 | 1.26292 | 0.0566647 | 0.291036 |
| S | 1.625 | 1.10718 | 0.0615109 | 0.255039 |
| S | 1.875 | 0.999204 | 0.0550255 | 0.246961 |
| S | 2.125 | 0.946403 | 0.0707376 | 0.231795 |
| S | 2.375 | 1.23797 | 0.105123 | 0.318212 |
| S | 2.625 | 1.47786 | 0.156612 | 0.364549 |
| S | 2.875 | 1.18313 | 0.15994 | 0.327472 |
| S | 3.250 | 0.985263 | 0.137371 | 0.272219 |
| S | 3.750 | 1.41988 | 0.300034 | 0.398105 |
| S | 4.500 | 1.19519 | 0.323683 | 0.344295 |
| S | 6.000 | 0.874146 | 0.393189 | 0.243415 |
| N | 1.125 | 1.21957 | 0.0512223 | 0.265693 |
| N | 1.375 | 1.29412 | 0.0566427 | 0.283042 |
| N | 1.625 | 1.18502 | 0.0610169 | 0.261016 |
| N | 1.875 | 1.19315 | 0.056677 | 0.279985 |
| N | 2.125 | 1.28275 | 0.076199 | 0.301409 |
| N | 2.375 | 1.16378 | 0.0918931 | 0.299825 |
| N | 2.625 | 1.05756 | 0.112921 | 0.267811 |
| N | 2.875 | 1.08408 | 0.137701 | 0.300777 |
| N | 3.250 | 1.07404 | 0.129499 | 0.291656 |
| N | 3.750 | 1.13863 | 0.233737 | 0.32574 |
| N | 4.500 | 1.24783 | 0.301555 | 0.358021 |
| N | 6.000 | 0.508304 | 0.248902 | 0.165648 |

Table B.12: Heavy-flavor muon p_T integrated R_{dA} for $1.0 < p_T < 3.0$ GeV/c at backward (South, $-2.0 < y < -1.4$) and forward (Nouth, $1.4 < y < 2.0$) rapidity.

| rapidity | $\langle N_{\text{coll}} \rangle$ | R_{dA} | stat. uncertainty | sys. uncertainty |
|----------|-----------------------------------|----------|-------------------|------------------|
| S | 15.061 | 1.61589 | 0.0431298 | 0.203374 |
| S | 10.248 | 1.33546 | 0.0375694 | 0.169593 |
| S | 6.579 | 1.22164 | 0.0358754 | 0.155549 |
| S | 3.198 | 1.07617 | 0.0325824 | 0.165974 |
| N | 15.061 | 0.59627 | 0.0205498 | 0.0758311 |
| N | 10.248 | 0.756535 | 0.0250276 | 0.0964502 |
| N | 6.579 | 0.907248 | 0.029359 | 0.115688 |
| N | 3.198 | 1.23132 | 0.0361499 | 0.185668 |

Table B.13: Heavy-flavor muon p_T integrated R_{dA} for $3.0 < p_T < 5.0$ GeV/c at backward (South, $-2.0 < y < -1.4$) and forward (Nouth, $1.4 < y < 2.0$) rapidity.

| rapidity | $\langle N_{\text{coll}} \rangle$ | R_{dA} | stat. uncertainty | sys. uncertainty |
|----------|-----------------------------------|----------|-------------------|------------------|
| S | 15.061 | 1.44459 | 0.130096 | 0.249339 |
| S | 10.248 | 1.54113 | 0.142309 | 0.263446 |
| S | 6.579 | 1.48402 | 0.147834 | 0.251471 |
| S | 3.198 | 1.09445 | 0.132282 | 0.213344 |
| N | 15.061 | 0.81931 | 0.0762939 | 0.139793 |
| N | 10.248 | 0.936014 | 0.0906309 | 0.160128 |
| N | 6.579 | 0.910326 | 0.0972223 | 0.157632 |
| N | 3.198 | 1.10466 | 0.115742 | 0.218173 |

Appendix C

Good run list

C.1 Run-9 $p+p$, MuIDLL-1D and -1H triggered data

Good runs for South and North muon arms are same.

281913, 281916, 281918, 281919, 281968, 281969, 281972, 281974, 282111, 282116, 282135, 282136, 282138, 282174, 282175, 282176, 282178, 282179, 282189, 282190, 282191, 282192, 282195, 282201, 282204, 282205, 282209, 282347, 282365, 282366, 282379, 282383, 282384, 282385, 282387, 282388, 282389, 282421, 282422, 282425, 282426, 282427, 282428, 282430, 282431, 282433, 282519, 282520, 282521, 282528, 282529, 282559, 282560, 282578, 282580, 282653, 282654, 282655, 282657, 282658, 282660, 282661, 282669, 282773, 282774, 282775, 282777, 282778, 283126, 283127, 283128, 283131, 283133, 283135, 283189, 283190, 283191, 283192, 283194, 283195, 283196, 283202, 283204, 283212, 283213, 283214, 283215, 283216, 283217, 283218, 283219, 283220, 283318, 283320, 283328, 283331, 283332, 283333, 283334,

283335, 283338, 283340, 283351, 283352, 283353, 283354, 283363, 283367, 283376, 283377, 283378, 283380, 283381, 283383, 283385, 283390, 283436, 283452, 283453, 283456, 283457, 283512, 283513, 283517, 283518, 283519, 283527, 283528, 283529, 283530, 283532, 283533, 283534, 283586, 283588, 283590, 283591, 283594, 283595, 283596, 283598, 283599, 283601, 283602, 283687, 283688, 283698, 283699, 283700, 283701, 283702, 283703, 283704, 283705, 283706, 283707, 283775, 283790, 283803, 283850, 283851, 283915, 283918, 283919, 283954, 283997, 284004, 284006, 284008, 284010, 284011, 284013, 284024, 284162, 284163, 284164, 284171, 284175, 284182, 284359, 284360, 284381, 284383, 284427, 284429, 284430, 284432, 284434, 284435, 284436, 284438, 284440, 284690, 284693, 284694, 284696, 284703, 284704, 284709, 284782, 284783, 284785, 284786, 284787, 284788, 284789, 284793, 284839, 284902, 284903, 284904, 284907, 284908, 284909, 284910, 284911, 284912, 284921, 284924, 284925, 284927, 284973, 284975, 284976, 284978, 284983, 285042, 285044, 285045, 285046, 285150, 285151, 285153, 285154, 285155, 285156, 285167, 285168, 285173, 285175, 285262, 285264, 285265, 285270, 285279, 285280, 285281, 285282, 285283, 285288, 285290, 285334, 285339, 285345, 285348, 285448, 285449, 285450, 285451, 285453, 285454, 285455, 285590, 285591, 285592, 285593, 285594, 285595, 285596, 285597, 285716, 285717, 285718, 285719, 285720, 285722, 285724, 285752, 285753, 285754, 285811, 285813, 285814, 285816, 285818, 285828, 285829, 285831, 285832, 285833, 285882, 285883, 285884, 285885, 285886, 285887, 285888, 285889, 285891, 285926, 285927, 285928, 285929, 285931, 285933, 285934, 285968, 285970, 285972, 285985, 285988, 285989, 285990, 285991, 286024, 286025, 286027, 286028, 286030, 286032, 286033, 286036, 286134, 286137, 286139, 286140, 286144, 286145, 286194, 286196, 286198, 286200, 286204, 286207, 286208, 286225, 286226, 286228, 286229, 286230, 286231, 286634,

286635, 286636, 286637, 286638, 286640, 286642, 286643, 286743, 286749, 286756, 286757, 286758, 286761, 286764, 286875, 286876, 286877, 286878, 286880, 286884, 287002, 287003, 287004, 287005, 287006, 287008, 287037, 287038, 287496, 287497, 287498, 287500, 287501, 287531, 287532, 287533, 287536, 287537, 287538, 287539, 287540, 287661, 287662, 287663, 287668, 287669, 287670, 287673, 287674, 287675, 287677, 287785, 287788, 287791, 287792, 287794, 287799, 287801, 287802, 287805, 287806, 287807, 287811, 287817, 287922, 287923, 287924, 287925, 287926, 287934, 287935, 287936, 287940, 287941, 287942, 287943, 287947, 287949, 287950, 287955, 287959, 287960, 287962, 287963, 288007, 288008, 288009, 288010, 288014, 288015, 288016, 288065, 288066, 288069, 288094, 288095, 288096, 288100, 288213, 288215, 288216, 288219, 288220, 288221, 288340, 288341, 288351, 288359, 288362, 288368, 288370, 288373, 288375, 288559, 288574, 288576, 288577, 288664, 288666, 288838, 288841, 288843, 288845, 288847, 288886, 288891, 288900, 288903, 288906, 289002, 289003, 289007, 289008, 289009, 289019, 289020, 289021, 289024, 289025, 289026, 289029, 289036, 289037, 289038, 289040, 289041, 289042, 289065, 289067, 289068, 289071, 289072, 289073, 289172, 289173, 289178, 289190, 289305, 289307, 289373, 289374, 289375, 289377, 289426, 289427, 289428, 289431, 289667, 289669, 289670, 289672, 289674, 289675, 289676, 289680, 289682, 289683, 289685, 289686, 289687, 289702, 289704, 289706, 289779, 289780, 289781, 289782, 289786, 289787, 289788, 289845, 289848, 289850, 289862, 289863, 289881, 289974, 289976, 289977, 289979, 290007, 290010, 290061, 290062, 290063, 290066, 290067, 290069, 290070, 290071, 290072, 290073, 290074, 290076, 290077, 290079, 290080, 290081, 290082, 290126, 290127, 290131, 290134, 290136, 290216, 290217, 290219, 290220, 290222, 290223, 290224, 290225, 290227, 290229, 290230, 290231, 290233, 290319, 290320, 290321, 290322, 290323, 290324,

290325, 290332, 290333, 290335, 290336, 290337, 290345, 290346, 290348, 290349, 290366, 290367, 290369, 290405, 290406, 290407, 290409, 290410, 290411, 290412, 290487, 290489, 290492, 290493, 290504, 290505, 290506, 290652, 290655, 290656, 290752, 290958, 290969, 290984, 290985, 290988, 290989, 290992, 291006, 291017, 291018, 291022, 291026, 291028, 291029, 291060, 291061, 291063, 291069, 291141, 291143, 291144

C.2 Run-8 $d+Au$, MuIDLL-1D triggered data for south arm

246466, 246468, 246469, 246472, 246474, 246479, 246480, 246483, 246484, 246485, 246486, 246488, 246490, 246492, 246496, 246497, 246498, 246499, 246500, 246501, 246503, 246510, 246512, 246516, 246541, 246542, 246543, 246544, 246545, 246546, 246547, 246548, 246550, 246551, 246581, 246582, 246583, 246585, 246594, 246595, 246597, 246599, 246600, 246603, 246605, 246606, 247037, 247041, 247044, 247045, 247055, 247169, 247172, 247173, 247176, 247179, 247180, 247182, 247184, 247185, 247186, 247189, 247190, 247191, 247221, 247229, 247231, 247232, 247234, 247235, 247237, 247238, 247239, 247240, 247241, 247242, 247243, 247244, 247245, 247246, 247248, 247249, 247250, 247251, 247253, 247254, 247255, 247256, 247377, 247378, 247379, 247381, 247382, 247385, 247388, 247389, 247391, 247392, 247397, 247399, 247400, 247401, 247403, 247404, 247411, 247426, 247428, 247429, 247433, 247434, 247435, 247436, 247437, 247438, 247439, 247440, 247483, 247484, 247611, 247614, 247615, 247616, 247623, 247624, 247625, 247626, 247631, 247782, 247784, 247786, 247787, 247788, 247789, 247817, 247818, 247820, 247821, 247936, 247938, 247939, 247941, 247942, 247947, 247948,

247950, 247951, 247959, 248034, 248037, 248039, 248040, 248045, 248052, 248055, 248148, 248149, 248150, 248152, 248166, 248167, 248170, 248171, 248177, 248178, 248184, 248289, 248291, 248293, 248295, 248298, 248308, 248310, 248311, 248355, 248359, 248363, 248364, 248365, 248367, 248368, 248380, 248382, 248383, 248473, 248475, 248476, 248478, 248479, 248490, 248522, 248525, 248527, 248528, 248529, 248533, 248534, 248667, 248671, 248782, 248785, 248788, 248789, 248790, 248865, 248871, 248886, 248887, 249052, 249065, 249069, 249070, 249072, 249085, 249086, 249093, 249094, 249111, 249117, 249123, 249124, 249138, 249146, 249147, 249148, 249255, 249257, 249258, 249259, 249391, 249394, 249398, 249399, 249401, 249405, 249407, 249433, 249437, 249440, 249441, 249445, 249453, 249454, 249455, 249456, 249458, 249460, 249463, 249464, 249466, 249471, 249472, 249474, 249487, 249488, 249491, 249495, 249497, 249499, 249716, 249720, 249727, 249728, 249731, 249732, 249738, 249742, 249746, 249747, 249748, 249750, 249751, 249768, 249769, 249771, 249772, 249838, 249839, 249843, 249844, 249847, 249853, 249854, 249858, 249866, 250003, 250006, 250010, 250012, 250014, 250019, 250020, 250022, 250023, 250024, 250025, 250026, 250041, 250042, 250044, 250045, 250046, 250047, 250048, 250049, 250095, 250096, 250097, 250098, 250101, 250152, 250153, 250154, 250156, 250157, 250158, 250159, 250165, 250166, 250167, 250168, 250169, 250171, 250173, 250174, 250211, 250212, 250214, 250215, 250216, 250218, 250220, 250223, 250224, 250276, 250277, 250278, 250279, 250280, 250281, 250282, 250306, 250307, 250308, 250309, 250310, 250313, 250319, 250321, 250322, 250325, 250327, 250328, 250336, 250482, 250483, 250484, 250593, 250594, 250595, 250597, 250702, 250703, 250782, 250786, 250788, 250790, 250792, 250794, 250795, 250837, 250838, 250840, 250842, 250971, 250972, 250973, 250975, 250977, 250978, 251049, 251050, 251054, 251055, 251059, 251060, 251061, 251063,

251064, 251065, 251102, 251105, 251106, 251107, 251109, 251111, 251124, 251133, 251136, 251329, 251331, 251332, 251334, 251338, 251412, 251417, 251485, 251487, 251489, 251491, 251492, 251497, 251498, 251499, 251500, 251501, 251502, 251503, 251510, 251511, 251512, 251685, 251687, 251689, 251690, 251692, 251695, 251697, 251819, 251822, 251823, 251824, 251825, 251826, 251827, 251829, 251837, 251838, 251839, 251840, 251841, 251842, 251843, 251846, 251849, 251850, 251851, 251852, 251853, 251854, 251855, 251857, 251858, 251859, 251862, 251863, 251946, 251947, 251948, 251949, 251952, 251956, 251960, 251962, 251964, 251965, 251975, 251976, 251977, 251978, 251979, 251988, 251989, 251992, 251993, 252102, 252103, 252104, 252106, 252115, 252116, 252117, 252118, 252120, 252121, 252123, 252125, 252127, 252128, 252130, 252131, 252134, 252135, 252140, 252141, 252143, 252144, 252146, 252147, 252187, 252190, 252193, 252195, 252196, 252197, 252201, 252202, 252203, 252209, 252210, 252216, 252219, 252220, 252222, 252225, 252228, 252232, 252233, 252235, 252238, 252239, 252240, 252242, 252256, 252257, 252259, 252260, 252262, 252501, 252503, 252505, 252506, 252507, 252774, 252775, 252776, 252783, 252787, 252793, 252935, 252936, 252937, 252949, 252950, 252951, 252956, 252957, 252961, 252966, 252967, 252968, 252969, 252971, 252976, 252977, 252978, 252981, 253020, 253022, 253023, 253024, 253025, 253029, 253036, 253037, 253038, 253039, 253040, 253095, 253097, 253101, 253102, 253141, 253143, 253144, 253147, 253151, 253153, 253154, 253157, 253161, 253295, 253296, 253297, 253298, 253299, 253301, 253302, 253317, 253428, 253433, 253434, 253436, 253437, 253442, 253443, 253444, 253445, 253447, 253450, 253451, 253458, 253459, 253460, 253524, 253525, 253526, 253535, 253536, 253539, 253540, 253541, 253571, 253572, 253629, 253631, 253632, 253633, 253634, 253693, 253694, 253695, 253697, 253698, 253699, 253700, 253701

C.3 Run-8 $d+$ Au, MuIDLL-1D triggered data for north arm

246466, 246469, 246472, 246474, 246479, 246480, 246484, 246485, 246486, 246488, 246490, 246492, 246497, 246498, 246499, 246500, 246501, 246503, 246510, 246512, 246516, 246541, 246542, 246543, 246544, 246545, 246546, 246547, 246550, 246551, 246581, 246582, 246583, 246585, 246587, 246594, 246597, 246599, 246600, 246603, 246605, 247037, 247041, 247044, 247045, 247054, 247055, 247169, 247172, 247173, 247176, 247179, 247180, 247182, 247184, 247185, 247186, 247189, 247190, 247191, 247221, 247229, 247230, 247231, 247232, 247234, 247235, 247237, 247238, 247239, 247240, 247241, 247242, 247243, 247244, 247245, 247246, 247248, 247249, 247250, 247251, 247253, 247254, 247255, 247256, 247377, 247378, 247379, 247381, 247382, 247385, 247388, 247389, 247391, 247392, 247397, 247399, 247400, 247401, 247403, 247404, 247411, 247426, 247428, 247429, 247433, 247434, 247435, 247436, 247437, 247438, 247439, 247440, 247483, 247484, 247611, 247614, 247615, 247616, 247624, 247625, 247626, 247631, 247817, 247818, 247820, 247821, 247936, 247938, 247939, 247941, 247942, 247947, 247948, 247950, 247951, 247959, 248034, 248037, 248039, 248040, 248045, 248052, 248055, 248148, 248149, 248150, 248152, 248166, 248167, 248170, 248171, 248177, 248178, 248184, 248289, 248291, 248293, 248295, 248298, 248308, 248310, 248311, 248355, 248359, 248363, 248364, 248365, 248367, 248368, 248382, 248383, 248490, 248527, 248534, 248667, 248671, 248782, 248785, 248788, 248789, 248865, 248871, 248887, 249052, 249065, 249069, 249070, 249072, 249085, 249086, 249093, 249094, 249111, 249117, 249123, 249124, 249138, 249146, 249147, 249148, 249255, 249257, 249258, 249259, 249391, 249394, 249398, 249399, 249401, 249405, 249407, 249433, 249437, 249440, 249441,

249445, 249453, 249454, 249455, 249456, 249458, 249460, 249463, 249464, 249466, 249471, 249472, 249474, 249487, 249488, 249491, 249495, 249497, 249499, 249716, 249720, 249727, 249728, 249731, 249732, 249738, 249742, 249746, 249747, 249748, 249750, 249751, 249771, 249772, 249837, 249838, 249839, 249843, 249844, 249847, 249853, 249854, 249858, 249866, 250003, 250006, 250010, 250012, 250014, 250019, 250020, 250022, 250023, 250024, 250025, 250026, 250041, 250042, 250044, 250045, 250046, 250047, 250048, 250049, 250095, 250096, 250097, 250098, 250101, 250152, 250153, 250154, 250156, 250157, 250158, 250159, 250169, 250171, 250173, 250174, 250211, 250212, 250214, 250215, 250216, 250218, 250220, 250223, 250224, 250276, 250277, 250278, 250279, 250593, 250594, 250595, 250597, 250698, 250702, 250703, 250786, 250790, 250792, 250794, 250795, 250837, 250838, 250840, 250842, 250847, 250848, 250849, 250862, 250864, 250865, 250866, 250873, 250875, 250878, 250879, 250883, 250885, 250887, 250973, 250975, 250977, 250978, 251049, 251054, 251055, 251060, 251061, 251063, 251064, 251065, 251101, 251102, 251105, 251106, 251107, 251109, 251111, 251124, 251125, 251133, 251136, 251331, 251332, 251334, 251338, 251412, 251417, 251485, 251487, 251489, 251491, 251492, 251497, 251498, 251499, 251500, 251501, 251502, 251503, 251510, 251511, 251512, 251687, 251689, 251690, 251692, 251695, 251697, 251819, 251822, 251823, 251824, 251825, 251826, 251827, 251829, 251836, 251837, 251838, 251839, 251840, 251841, 251842, 251843, 251846, 251849, 251850, 251851, 251852, 251853, 251854, 251855, 251857, 251858, 251859, 251862, 251863, 251946, 251947, 251948, 251949, 251952, 251956, 251960, 251962, 251964, 251965, 251969, 251975, 251976, 251977, 251978, 251979, 251988, 251989, 251992, 251993, 252102, 252103, 252104, 252106, 252115, 252116, 252117, 252118, 252120, 252121, 252123, 252125, 252127, 252128, 252130, 252131, 252134, 252135, 252140, 252141, 252143,

252144, 252146, 252147, 252187, 252190, 252193, 252195, 252196, 252197, 252201, 252202, 252203, 252209, 252210, 252216, 252219, 252220, 252222, 252225, 252228, 252232, 252233, 252235, 252238, 252239, 252240, 252242, 252255, 252256, 252257, 252259, 252260, 252262, 252501, 252503, 252505, 252506, 252507, 252520, 252521, 252524, 252526, 252616, 252618, 252622, 252623, 252625, 252632, 252633, 252634, 252650, 252655, 252656, 252658, 252660, 252661, 252774, 252775, 252776, 252783, 252787, 252793, 252927, 252929, 252930, 252931, 252935, 252936, 252937, 252949, 252950, 252951, 252956, 252957, 252961, 252966, 252967, 252968, 252969, 252971, 252975, 252976, 252977, 252978, 252981, 253020, 253022, 253023, 253024, 253025, 253029, 253036, 253037, 253038, 253039, 253040, 253092, 253095, 253097, 253101, 253102, 253141, 253143, 253144, 253147, 253151, 253153, 253154, 253157, 253161, 253295, 253296, 253297, 253298, 253299, 253301, 253302, 253317, 253428, 253433, 253434, 253436, 253437, 253442, 253443, 253444, 253445, 253447, 253450, 253451, 253458, 253459, 253460, 253523, 253524, 253526, 253535, 253536, 253539, 253540, 253541, 253568, 253569, 253570, 253571, 253572, 253629, 253631, 253632, 253633, 253634, 253693, 253694, 253695, 253697, 253698, 253699, 253700, 253701

C.4 Run-8 d +Au, MuIDLL-1H triggered data for south arm

247483, 247484, 247611, 247614, 247615, 247616, 247623, 247624, 247625, 247626, 247631, 247782, 247784, 247786, 247787, 247788, 247789, 247817, 247818, 247820, 247821, 247936, 247938, 247939, 247941, 247942, 247947, 247948, 247950, 247951, 247959, 248034, 248037, 248039, 248040, 248045,

248052, 248055, 248148, 248150, 248152, 248166, 248167, 248170, 248171, 248177, 248184, 248289, 248291, 248293, 248295, 248298, 248308, 248310, 248311, 248355, 248359, 248363, 248365, 248367, 248368, 248380, 248382, 248383, 248473, 248475, 248476, 248478, 248479, 248490, 248522, 248525, 248527, 248528, 248529, 248533, 248534, 248667, 248671, 248782, 248785, 248788, 248789, 248790, 248865, 248871, 248887, 249052, 249065, 249069, 249070, 249072, 249085, 249086, 249093, 249094, 249111, 249117, 249123, 249124, 249138, 249146, 249147, 249148, 249255, 249257, 249258, 249259, 249391, 249394, 249398, 249401, 249405, 249407, 249433, 249437, 249441, 249445, 249453, 249454, 249455, 249456, 249458, 249460, 249463, 249464, 249466, 249471, 249472, 249474, 249487, 249488, 249491, 249495, 249497, 249499, 249720, 249727, 249731, 249732, 249738, 249747, 249748, 249750, 249751, 249768, 249769, 249771, 249772, 249837, 249838, 249843, 249844, 249847, 249853, 249854, 249858, 249866, 250003, 250006, 250010, 250012, 250014, 250020, 250022, 250023, 250024, 250025, 250026, 250041, 250042, 250044, 250045, 250046, 250047, 250048, 250049, 250095, 250096, 250097, 250098, 250101, 250152, 250153, 250154, 250156, 250157, 250158, 250159, 250166, 250167, 250168, 250169, 250171, 250173, 250174, 250211, 250212, 250214, 250215, 250216, 250218, 250220, 250223, 250224, 250276, 250277, 250278, 250279, 250280, 250281, 250282, 250306, 250307, 250308, 250309, 250313, 250319, 250321, 250322, 250325, 250327, 250328, 250336, 250482, 250483, 250484, 250593, 250594, 250595, 250597, 250698, 250702, 250703, 250782, 250786, 250788, 250790, 250792, 250794, 250795, 250838, 250840, 250842, 250971, 250972, 250973, 250975, 250977, 250978, 251049, 251050, 251054, 251055, 251059, 251060, 251061, 251063, 251064, 251065, 251101, 251102, 251105, 251106, 251107, 251109, 251111, 251124, 251125, 251133, 251136, 251329, 251331, 251332, 251334, 251338, 251412, 251417, 251485,

251487, 251489, 251491, 251492, 251497, 251498, 251499, 251500, 251501, 251502, 251503, 251510, 251511, 251512, 251687, 251689, 251690, 251692, 251695, 251697, 251819, 251823, 251824, 251825, 251826, 251827, 251829, 251838, 251839, 251840, 251841, 251842, 251843, 251846, 251850, 251851, 251852, 251853, 251854, 251855, 251857, 251858, 251859, 251862, 251863, 251947, 251948, 251949, 251952, 251956, 251960, 251962, 251964, 251965, 251975, 251976, 251977, 251978, 251979, 251988, 251989, 251992, 251993, 252102, 252103, 252104, 252106, 252115, 252116, 252117, 252118, 252120, 252121, 252123, 252125, 252127, 252128, 252130, 252131, 252134, 252135, 252140, 252141, 252143, 252144, 252146, 252147, 252190, 252193, 252195, 252196, 252197, 252202, 252203, 252209, 252210, 252216, 252219, 252220, 252222, 252225, 252228, 252232, 252233, 252235, 252238, 252239, 252240, 252242, 252255, 252256, 252257, 252259, 252260, 252262, 252501, 252503, 252505, 252506, 252507, 252774, 252775, 252776, 252783, 252787, 252793, 252935, 252936, 252937, 252949, 252951, 252956, 252957, 252961, 252966, 252967, 252968, 252969, 252971, 252976, 252977, 252978, 252981, 253022, 253023, 253024, 253025, 253029, 253037, 253038, 253039, 253040, 253093, 253095, 253097, 253101, 253102, 253141, 253143, 253144, 253147, 253153, 253154, 253157, 253161, 253296, 253297, 253298, 253299, 253301, 253302, 253317, 253428, 253433, 253434, 253436, 253437, 253442, 253443, 253444, 253445, 253447, 253450, 253451, 253458, 253459, 253460, 253524, 253525, 253536, 253539, 253540, 253541, 253570, 253571, 253572, 253631, 253632, 253633, 253634, 253693, 253694, 253695, 253698, 253699, 253700, 253701

C.5 Run-8 $d+\text{Au}$, MuIDLL-1H triggered data for north arm

247938, 247939, 247942, 247947, 247948, 247950, 247951, 247959, 248036, 248037, 248039, 248040, 248055, 248149, 248150, 248166, 248167, 248170, 248171, 248177, 248182, 248289, 248291, 248293, 248295, 248298, 248305, 248308, 248355, 248359, 248363, 248364, 248365, 248367, 248380, 248382, 248383, 248473, 248475, 248476, 248478, 248479, 248490, 248522, 248525, 248527, 248528, 248533, 248534, 248667, 248782, 248785, 248788, 248789, 248790, 248871, 248887, 249052, 249069, 249070, 249072, 249085, 249086, 249093, 249094, 249111, 249117, 249123, 249124, 249146, 249148, 249255, 249257, 249258, 249259, 249391, 249394, 249398, 249399, 249405, 249407, 249433, 249441, 249445, 249452, 249453, 249455, 249456, 249458, 249460, 249463, 249464, 249466, 249471, 249472, 249474, 249487, 249488, 249491, 249495, 249497, 249720, 249727, 249728, 249731, 249732, 249738, 249750, 249751, 249771, 249772, 249837, 249838, 249844, 249847, 249853, 249854, 249858, 249866, 250003, 250006, 250010, 250012, 250014, 250022, 250023, 250024, 250025, 250026, 250042, 250044, 250045, 250046, 250047, 250048, 250049, 250095, 250096, 250097, 250098, 250101, 250152, 250153, 250154, 250156, 250157, 250158, 250159, 250167, 250168, 250169, 250171, 250173, 250174, 250211, 250212, 250214, 250215, 250216, 250218, 250220, 250223, 250224, 250276, 250277, 250278, 250279, 250593, 250594, 250595, 250597, 250698, 250702, 250703, 250786, 250788, 250790, 250792, 250794, 250795, 250837, 250838, 250840, 250842, 250847, 250848, 250849, 250862, 250864, 250865, 250866, 250873, 250875, 250877, 250878, 250879, 250883, 250885, 250887, 250971, 250972, 250973, 250975, 250977, 250978, 251049, 251054, 251055, 251059, 251060, 251061, 251063, 251064, 251065, 251101, 251102,

251105, 251106, 251107, 251109, 251111, 251124, 251125, 251133, 251136, 251329, 251331, 251332, 251334, 251338, 251412, 251417, 251485, 251487, 251489, 251491, 251492, 251497, 251498, 251499, 251500, 251502, 251503, 251510, 251511, 251512, 251685, 251687, 251689, 251690, 251692, 251695, 251697, 251819, 251822, 251823, 251824, 251825, 251826, 251827, 251829, 251836, 251837, 251838, 251839, 251840, 251841, 251842, 251843, 251846, 251849, 251850, 251851, 251852, 251853, 251854, 251855, 251857, 251858, 251859, 251862, 251863, 251946, 251947, 251948, 251949, 251952, 251956, 251962, 251964, 251965, 251969, 251975, 251976, 251977, 251978, 251979, 251988, 251989, 251992, 251993, 252102, 252103, 252104, 252106, 252115, 252116, 252117, 252118, 252120, 252121, 252123, 252125, 252127, 252128, 252130, 252131, 252134, 252135, 252140, 252141, 252143, 252144, 252146, 252147, 252187, 252190, 252193, 252195, 252196, 252197, 252201, 252202, 252203, 252209, 252210, 252216, 252219, 252220, 252222, 252225, 252228, 252232, 252233, 252235, 252238, 252239, 252240, 252242, 252255, 252256, 252257, 252259, 252260, 252262, 252501, 252503, 252504, 252505, 252506, 252507, 252520, 252521, 252524, 252526, 252616, 252618, 252622, 252623, 252625, 252632, 252633, 252634, 252650, 252655, 252656, 252658, 252660, 252661, 252774, 252775, 252776, 252783, 252787, 252793, 252927, 252929, 252930, 252931, 252935, 252936, 252937, 252949, 252950, 252951, 252956, 252957, 252961, 252966, 252967, 252968, 252969, 252971, 252975, 252976, 252977, 252978, 252981, 253020, 253022, 253023, 253024, 253025, 253029, 253036, 253037, 253038, 253039, 253040, 253092, 253095, 253097, 253101, 253102, 253141, 253143, 253144, 253147, 253151, 253153, 253154, 253157, 253161, 253295, 253296, 253297, 253298, 253299, 253301, 253302, 253317, 253428, 253433, 253434, 253436, 253437, 253440, 253442, 253443, 253444, 253445, 253447, 253450, 253451, 253458, 253459, 253460, 253523, 253524,

253525, 253526, 253535, 253536, 253539, 253540, 253541, 253568, 253569, 253570, 253571, 253572, 253629, 253631, 253632, 253633, 253634, 253693, 253694, 253695, 253697, 253698, 253699, 253700, 253701

Bibliography

- [1] J. Beringer et al., Review of Particle Physics (RPP), Phys.Rev. **D86**, 010001 (2012).
- [2] E. V. Shuryak, Quantum Chromodynamics and the Theory of Superdense Matter, Phys.Rept. **61**, 71–158 (1980).
- [3] H. D. Politzer, Reliable Perturbative Results for Strong Interactions?, Phys.Rev.Lett. **30**, 1346–1349 (1973).
- [4] H. D. Politzer, Asymptotic Freedom: An Approach to Strong Interactions, Phys.Rept. **14**, 129–180 (1974).
- [5] D. Gross and F. Wilczek, Asymptotically Free Gauge Theories. 1, Phys.Rev. **D8**, 3633–3652 (1973).
- [6] D. Gross and F. Wilczek, ASYMPTOTICALLY FREE GAUGE THEORIES. 2., Phys.Rev. **D9**, 980–993 (1974).
- [7] S. Bethke, Experimental tests of asymptotic freedom, Prog.Part.Nucl.Phys. **58**, 351–386 (2007).

- [8] F. Karsch, E. Laermann, and A. Peikert, The Pressure in two flavor, (2+1)-flavor and three flavor QCD, *Phys.Lett.* **B478**, 447–455 (2000).
- [9] F. Karsch and E. Laermann, Thermodynamics and in medium hadron properties from lattice QCD, (2003).
- [10] P. Sorensen, Elliptic Flow: A Study of Space-Momentum Correlations In Relativistic Nuclear Collisions, (2009).
- [11] K. Rajagopal, Mapping the QCD phase diagram, *Nucl.Phys.* **A661**, 150–161 (1999).
- [12] P. Jacobs, D. Kharzeev, B. Muller, J. Nagle, K. Rajagopal, et al., Phases of QCD: Summary of the Rutgers long range plan town meeting, January 12-14, 2007, (2007).
- [13] K. Adcox et al., Formation of dense partonic matter in relativistic nucleus-nucleus collisions at RHIC: Experimental evaluation by the PHENIX collaboration, *Nucl.Phys.* **A757**, 184–283 (2005).
- [14] I. Arsene et al., Quark gluon plasma and color glass condensate at RHIC? The Perspective from the BRAHMS experiment, *Nucl.Phys.* **A757**, 1–27 (2005).
- [15] B. Back, M. Baker, M. Ballintijn, D. Barton, B. Becker, et al., The PHOBOS perspective on discoveries at RHIC, *Nucl.Phys.* **A757**, 28–101 (2005).
- [16] J. Adams et al., Experimental and theoretical challenges in the search for the quark gluon plasma: The STAR Collabora-

- tion's critical assessment of the evidence from RHIC collisions, *Nucl.Phys. A***757**, 102–183 (2005).
- [17] J. Bjorken, Highly Relativistic Nucleus-Nucleus Collisions: The Central Rapidity Region, *Phys.Rev. D***27**, 140–151 (1983).
- [18] M. Gyulassy and M. Plumer, Jet Quenching in Dense Matter, *Phys.Lett. B***243**, 432–438 (1990).
- [19] S. Adler et al., A Detailed Study of High- $p(T)$ Neutral Pion Suppression and Azimuthal Anisotropy in Au+Au Collisions at $s(NN)^{**}(1/2) = 200$ -GeV, *Phys.Rev. C***76**, 034904 (2007).
- [20] J. Adams et al., Evidence from d + Au measurements for final state suppression of high $p(T)$ hadrons in Au+Au collisions at RHIC, *Phys.Rev.Lett. 91*, 072304 (2003).
- [21] A. Adare et al., Scaling properties of azimuthal anisotropy in Au+Au and Cu+Cu collisions at $s(NN) = 200$ -GeV, *Phys.Rev.Lett. 98*, 162301 (2007).
- [22] J. Adams et al., Particle type dependence of azimuthal anisotropy and nuclear modification of particle production in Au + Au collisions at $s(NN)^{**}(1/2) = 200$ -GeV, *Phys.Rev.Lett. 92*, 052302 (2004).
- [23] J. Adams et al., Multi-strange baryon elliptic flow in Au + Au collisions at $s(NN)^{**}(1/2) = 200$ -GeV, *Phys.Rev.Lett. 95*, 122301 (2005).

- [24] I. Arsene et al., On the evolution of the nuclear modification factors with rapidity and centrality in $d + Au$ collisions at $s(NN)^{**}(1/2) = 200$ -GeV, *Phys.Rev.Lett.* **93**, 242303 (2004).
- [25] R. Plackyte, arXiv:1111.5452.
- [26] K. J. Eskola, H. Paukkunen, and C. A. Salgado, EPS09: A New Generation of NLO and LO Nuclear Parton Distribution Functions, *JHEP* **0904**, 065 (2009).
- [27] J. Aubert et al., The ratio of the nucleon structure functions F_{2n} for iron and deuterium, *Phys.Lett.* **B123**, 275 (1983).
- [28] D. de Florian and R. Sassot, Nuclear parton distributions at next-to-leading order, *Phys.Rev.* **D69**, 074028 (2004).
- [29] K. Eskola, V. Kolhinen, and C. Salgado, The Scale dependent nuclear effects in parton distributions for practical applications, *Eur.Phys.J.* **C9**, 61–68 (1999).
- [30] I. Helenius, K. J. Eskola, H. Honkanen, and C. A. Salgado, Modeling the Impact Parameter Dependence of the nPDFs With EKS98 and EPS09 Global Fits, *JHEP* **1207**, 073 (2012).
- [31] J. Arrington, New Measurements of the EMC Effect in Few-Body Nuclei, *J.Phys.Conf.Ser.* **69**, 012024 (2007).
- [32] A. Bodek and J. Ritchie, Fermi Motion Effects in Deep Inelastic Lepton Scattering from Nuclear Targets, *Phys.Rev.* **D23**, 1070 (1981).

- [33] A. Bodek and J. Ritchie, Further Studies of Fermi Motion Effects in Lepton Scattering from Nuclear Targets, Phys.Rev. **D24**, 1400 (1981).
- [34] A. Adare et al., Suppression of back-to-back hadron pairs at forward rapidity in d +Au Collisions at $\sqrt{s_{NN}} = 200$ GeV, Phys.Rev.Lett. **107**, 172301 (2011).
- [35] J. Cronin, H. J. Frisch, M. Shochet, J. Boymond, R. Mermod, et al., Production of Hadrons with Large Transverse Momentum at 200-GeV, 300-GeV, and 400-GeV, Phys.Rev. **D11**, 3105 (1975).
- [36] A. Adare et al., Spectra and ratios of identified particles in Au+Au and d +Au collisions at $\sqrt{s_{NN}} = 200$ GeV, (2013).
- [37] A. Adare et al., Transverse-Momentum Dependence of the J/ψ Nuclear Modification in d +Au Collisions at $\sqrt{s_{NN}} = 200$ GeV, Phys. Rev. C **87**, 034904 (2013).
- [38] R. C. Hwa and C. B. Yang, Final state interaction as the origin of the Cronin effect, Phys. Rev. Lett. **93**, 082302 (2004).
- [39] A. Adare et al., Cold Nuclear Matter Effects on J/ψ Yields as a Function of Rapidity and Nuclear Geometry in Deuteron-Gold Collisions at $\sqrt{s_{NN}} = 200$ GeV, Phys. Rev. Lett. **107**, 142301 (2011).
- [40] R. Arnaldi et al., J/psi production in proton-nucleus collisions at 158 and 400 GeV, Phys.Lett. **B706**, 263–267 (2012).

- [41] C. Lourenco, R. Vogt, and H. K. Woehri, Energy dependence of J/psi absorption in proton-nucleus collisions, *JHEP* **0902**, 014 (2009).
- [42] A. Adare et al., Cold Nuclear Matter Effects on J/Psi as Constrained by Deuteron-Gold Measurements at $s(\text{NN})^{**}(1/2) = 200\text{-GeV}$, *Phys. Rev. C* **77**, 024912 (2008).
- [43] R. Vogt, Uncertainties in the charm production cross section, Heavy Quark Workshop at LBNL, 2007.
- [44] G. Bunce, N. Saito, J. Soffer, and W. Vogelsang, Prospects for spin physics at RHIC, *Ann.Rev.Nucl.Part.Sci.* **50**, 525–575 (2000).
- [45] J. C. Collins, D. E. Soper, and G. F. Sterman, Factorization of Hard Processes in QCD, *Adv.Ser.Direct.High Energy Phys.* **5**, 1–91 (1988).
- [46] J. C. Collins, Hard scattering factorization with heavy quarks: A General treatment, *Phys.Rev.* **D58**, 094002 (1998).
- [47] R. Vogt, The Total charm cross-section, *Eur.Phys.J.ST* **155**, 213–222 (2008).
- [48] M. Cacciari, P. Nason, and R. Vogt, QCD predictions for charm and bottom production at RHIC, *Phys.Rev.Lett.* **95**, 122001 (2005).
- [49] D. Hornback, 2008, Ph.D. thesis.

- [50] A. Adare et al., Measurement of high- $p(T)$ single electrons from heavy-flavor decays in $p+p$ collisions at $s^{**}(1/2) = 200$ -GeV, *Phys. Rev. Lett.* **97**, 252002 (2006).
- [51] M. Cacciari, M. Greco, and P. Nason, The $p(T)$ spectrum in heavy flavor hadroproduction, *JHEP* **9805**, 007 (1998).
- [52] M. Cacciari, S. Frixione, and P. Nason, The $p(T)$ spectrum in heavy flavor photoproduction, *JHEP* **0103**, 006 (2001).
- [53] A. Adare et al., Nuclear-Modification Factor for Open-Heavy-Flavor Production at Forward Rapidity in Cu+Cu Collisions at $\sqrt{s_{NN}} = 200$ GeV, *Phys. Rev. C* **86**, 024909 (2012).
- [54] Y. L. Dokshitzer and D. Kharzeev, Heavy quark colorimetry of QCD matter, *Phys.Lett.* **B519**, 199–206 (2001).
- [55] A. Adare et al., Energy Loss and Flow of Heavy Quarks in Au+Au Collisions at $s(NN)^{**}(1/2) = 200$ -GeV, *Phys. Rev. Lett.* **98**, 172301 (2007).
- [56] A. Adare et al., System-size dependence of open-heavy-flavor production in nucleus-nucleus collisions at $\sqrt{s_{NN}}=200$ GeV, (2013).
- [57] R. Sharma, I. Vitev, and B.-W. Zhang, Light-cone wave function approach to open heavy flavor dynamics in QCD matter, *Phys.Rev. C* **80**, 054902 (2009).
- [58] I. Vitev, Non-Abelian energy loss in cold nuclear matter, *Phys. Rev. C* **75**, 064906 (2007).
- [59] A. Adare et al., arXiv:1208.1293.

- [60] K. Adcox et al., PHENIX central arm tracking detectors, *Nucl.Instrum.Meth.* **A499**, 489–507 (2003).
- [61] M. Aizawa et al., PHENIX central arm particle ID detectors, *Nucl.Instrum.Meth.* **A499**, 508–520 (2003).
- [62] H. Akikawa et al., PHENIX muon arms, *Nucl. Instrum. Methods A* **499**, 537–548 (2003).
- [63] M. Allen et al., PHENIX inner detectors, *Nucl.Instrum.Meth.* **A499**, 549–559 (2003).
- [64] R. J. Newby, 2003, J/ψ production in Au+Au Collisions at 200 GeV, Ph.D thesis, University of Tennessee.
- [65] S. S. Adler et al., PHENIX on-line systems, *Nucl.Instrum.Meth.* **A499**, 560–592 (2003).
- [66] H. Sato et al., 2003, PHENIX analysis note 184.
- [67] J. Nagle, 2010, PHENIX analysis note 900.
- [68] M. L. Miller, K. Reygers, S. J. Sanders, and P. Steinberg, Glauber modeling in high energy nuclear collisions, *Ann. Rev. Nucl. Part. Sci.* **57**, 205–243 (2007).
- [69] S. Adler et al., Measurement of Single Muons at Forward Rapidity in p+p Collisions at $s^{**}(1/2) = 200$ -GeV and Implications for Charm Production, *Phys.Rev.* **D76**, 092002 (2007).
- [70] R. Brun, F. Carminati, and S. Giani, 1994, GEANT CERN-W-5013 (1994).

- [71] X. He, J. Ying, A. Sen, and L. Patel, 2012, PHENIX analysis note 1004.
- [72] M. Chiu, B. Hong, K. Lee, M. Leitch, H. Pereira, C. Silva, and Y. Kim, 2012, PHENIX analysis note 890.
- [73] J. Nagle, 2009, PHENIX analysis note 844.
- [74] Y. Cobigo, J. Gosset, and H. Pereira, 2003, PHENIX technical note 405.
- [75] T. Sjostrand, S. Mrenna, and P. Z. Skands, PYTHIA 6.4 Physics and Manual, JHEP **0605**, 026 (2006).
- [76] M. Gyulassy and X.-N. Wang, HIJING 1.0: A Monte Carlo program for parton and particle production in high-energy hadronic and nuclear collisions, Comput.Phys.Commun. **83**, 307 (1994).
- [77] I. Garishvili, 2009, Ph.D. thesis.
- [78] I. Garishvili, D. Hornback, Y. Kwon, M. Liu, K. Read, X. Wang, V. Cianciolo, and J. Hamblen, 2007, PHENIX analysis note 606.
- [79] M. Durham, 2012, PHENIX analysis note 1016.
- [80] I. Garhsivili, D. Hornback, K. Read, and V. Cianciolo, 2011, PHENIX analysis note 962.
- [81] A. Adare et al., Ground and excited charmonium state production in $\mathbf{p} + \mathbf{p}$ collisions at $\sqrt{s} = 200$ GeV, Phys.Rev. **D85**, 092004 (2012).

- [82] A. Adare et al., Heavy Quark Production in $\mathbf{p}+\mathbf{p}$ and Energy Loss and Flow of Heavy Quarks in Au+Au Collisions at $\sqrt{s_{NN}} = 200$ GeV, Phys. Rev. C **84**, 044905 (2011).
- [83] M. Durham, 2013, PHENIX analysis note 1098.
- [84] A. Frawley, C. Silve, and D. McGlinchey, 2013, PHENIX analysis note 1001.
- [85] J. Nagle and M. Wysocki, 2012, PHENIX analysis note 997.
- [86] A. Adare et al., $\mathbf{v(1S + 2S + 3S)}$ production in $\mathbf{d}+\text{Au}$ and $\mathbf{p} + \mathbf{p}$ collisions at $\sqrt{s_{NN}} = 200$ GeV and cold-nuclear matter effects, Phys.Rev. **C87**, 044909 (2013).
- [87] J. K. Yoh, S. W. Herb, D. C. Hom, L. M. Lederman, J. C. Sens, et al., Study of Scaling in Hadronic Production of Dimuons, Phys. Rev. Lett. **41**, 684 (1978).
- [88] T. Sjostrand, S. Mrenna, and P. Z. Skands, A Brief Introduction to PYTHIA 8.1, Comput.Phys.Commun. **178**, 852–867 (2008).
- [89] A. Adare et al., Measurement of Bottom versus Charm as a Function of Transverse Momentum with Electron-Hadron Correlations in $\mathbf{p}+\mathbf{p}$ Collisions at $\sqrt{s} = 200$ GeV, Phys. Rev. Lett. **103**, 082002 (2009).
- [90] B. Alver et al., Phobos results on charged particle multiplicity and pseudorapidity distributions in Au+Au, Cu+Cu, d+Au, and p+p collisions at ultra-relativistic energies, Phys.Rev. **C83**, 024913 (2011).

- [91] A. Adare et al., Cold-nuclear-matter effects on heavy-quark production at forward and backward rapidity in d+Au collisions at $\sqrt{s_{NN}}=200$ GeV, (2013).
- [92] C. Aidala, L. Anaya, L. Anderssen, A. Bambaugh, A. Barron, et al., The PHENIX Forward Silicon Vertex Detector, (2013).
- [93] A. Taketani et al., Silicon vertex tracker for RHIC PHENIX experiment, Nucl.Instrum.Meth. **A623**, 374–376 (2010).
- [94] PHENIX Beam User Proposal for RHIC Run-14 and Run-15, 2013, <https://indico.bnl.gov/conferenceDisplay.py?confId=632>.

국문요약

질량 중심에너지 200GeV의 중양자-금이온 충돌에서
발생한 무거운 쿼크의 붕괴에서 온 단일 뮤온의
핵변환인자 R_{dA} 측정

임상훈
연세대학교 대학원
물리 및 응용물리 학과

RHIC에서 수행되는 중이온 충돌 실험에서 충돌 초기에 생성되는 무거운 쿼크들은 이 실험에서 생성되는 높은 밀도의 물질을 연구하는데 매우 효과적이다. 양성자-양성자 충돌에서 발생하는 무거운 쿼크의 측정 결과는 섭동 양자색소역학의 계산과의 비교를 통해 이론 모델을 시험할 수 있고, 다양한 충돌 실험에서 얻는 결과를 해석하기 위한 비교군의 역할도 한다. 특히 중양자-금이온 충돌 실험을 통해 초기상태의 차가운 핵물질 효과가 어떻게 무거운 쿼크의 생성에 영향을 주는지 연구할 수 있다.

피닉스 실험의 뮤온 검출기는 전방 신속도 ($1.2 < \eta < 2.4$) 및 후방 신속도 ($-2.2 < \eta < -1.2$) 영역에서 뮤온을 검출하기 위한 장치이다. 2005년에 수집한 양성자-양성자 및 구리 이온들간의 충돌 실험 자료를 분석한 이전의 연구에서 배경사건을 제거하기 위한 효율적인 자료 분석 방법이 개발되었다. 이 방법은 강입자 모사실험을 통해 배경사건들을 예측하는 방법으로 “강입자 칵테일” 방법이라고

불리운다. 유사한 자료 분석 방법이 2008년에 수집한 중양자-금이온 및 2009년에 수집한 양성자-양성자 충돌 실험 자료를 분석한 본 연구에도 사용되었다. 본 연구를 통해 중양자-금이온 및 양성자-양성자 충돌에서 발생한 무거운 쿼크에서 오는 단일 뮤온의 생성량을 전방 신속도 영역, $1.4 < |y| < 2.0$, 에서 측정하였다. 두 충돌 실험 자료에서 측정한 생성량을 바탕으로 무거운 쿼크에 영향을 미치는 차가는 핵물질 효과를 정량적으로 알아보기 위해 핵변환인자 R_{dA} 를 다양한 충돌 겹침도에 (0–100%, 0–20%, 20–40%, 40–60%, 60–88%) 대해서 계산하였다.

핵심되는 말 : RHIC, 피닉스 (PHENIX), 차가운 핵물질 효과, 무거운 쿼크, 핵변환인자 (R_{dA})

논문을 마무리하며...

어느덧 대학에 들어온지도 10년이라는 시간이 지나 이제는 박사과정의 마무리를 하는 때에 이르게 되었습니다. 논문을 마무리한다는 후련함 보다는 아직 ‘박사’라는 이름에 아직 부족한 것이 많지 않은지 걱정이 앞섭니다. 다시 새롭게 시작하는 마음으로 모자랐던 부분들을 계속 채워나가야 할 것 같습니다.

물리를 처음 배울 때부터 박사 논문을 마무리하는 지금에 이르기까지 도움을 주신 주위의 많은 분들에게 감사를 드립니다. 고등학교에서 물리를 시작하는데 도움을 주신 이종복 선생님, 학위 과정동안 많은 지도와 지원을 해주신 강주환, 권영일 교수님, 심사위원으로 논문을 마무리 하는데 도움을 주신 주관식, 이수형 교수님께 감사드립니다. 또한 대학 생활의 대부분 이었던 한얼^R의 선후배 분들, 과학관 319호에서 함께 하였던 핵물리 연구실 선후배 분들, BNL에서 지내는 동안 도움을 주신 분들에게도 감사하는 마음입니다. 특히 연구를 진행하고 미국에서 생활하는데 많은 조언과 도움을 주신 인제형에게 감사를 전하고 싶습니다.

앞으로 행복한 날들을 함께할 당신에게도 옆에서 힘이 되어 주어서 고맙고 사랑한다고 전합니다. 마지막으로 당신 자신 보다는 항상 제가 우선이셨던 부모님께 마음속에 담아 두고 표현하지 못했던 감사와 사랑을 전하고 싶습니다. 항상 감사하는 마음으로 이에 보답하는 삶을 살아갈 수 있도록 노력하겠습니다.

2013년 12월 눈오는 어느 날
임상훈